MODELING OF CONCRETE UNDER HIGH STRAIN RATE CONDITIONS USING NONLINEAR FINITE ELEMENT METHOD

A Thesis Submitted to
The Graduate School of Engineering and Sciences of
Izmir Institute of Technology
in Partial Fulfillment of the Requirements for the Degree of

DOCTOR OF PHILOSOPHY

in Civil Engineering

by
M. ALPER ÇANKAYA

JULY 2017

İZMİR

We approve the thesis of **Mehmet Alper ÇANKAYA**

Examining Committee Members:

Assist. Prof. Dr. Selçuk SAATCI
Department of Civil Engineering, İzmir Institute of Technology

Prof. Dr. Mustafa GÜDEN
Department of Mechanical Engineering, İzmir Institute of Technology

Assoc. Prof. Dr. İzzet ÖZDEMİR
Department of Civil Engineering, İzmir Institute of Technology

Prof. Dr. Babür DELİKTAŞ
Department of Civil Engineering, Uludağ University

Assist. Prof. Dr. Levent AYDIN
Department of Mechanical Engineering, İzmir Katip Çelebi University

19 July 2017

Assist. Prof. Dr. Selçuk SAATCI
Supervisor, Department of Civil Engineering
İzmir Institute of Technology

Prof. Dr. Alper TAŞDEMİRCİ
Co-Supervisor, Department of Mechanical Engineering
İzmir Institute of Technology

Prof. Dr. Şebnem ELÇİ
Head of the Department of Civil Engineering

Prof. Dr. Aysun SOFUOĞLU
Dean of the Graduate School of Engineering and Sciences

ACKNOWLEDGEMENTS

This research project was performed at Dynamic Testing and Modeling Laboratory in the Izmir Institute of Technology and was financially supported by Scientific and Research Council of Turkey (TÜBİTAK). I would like to express my sincere gratitude to these organizations for the support provided.

I would like to express my appreciation to my advisor Assist. Prof. Dr. Selcuk Saatcı and co-advisor Prof. Dr. Alper Taşdemirci for all of their contributions, encouragement and support throughout this project and thesis study.

I wish to thank my colleagues at the Department of Civil and Mechanical Engineering and all of those who helped me in anyhow during the accomplishment of the study.

Lastly, I owe gratefulness to my parents and family for their endless support throughout my life.

ABSTRACT

MODELING OF REINFORCED CONCRETE UNDER HIGH STRAIN RATE CONDITIONS USING NONLINEAR FINITE ELEMENT METHOD

In this study, a comprehensive experimental and numerical study was undertaken to model concrete under high strain rate conditions. Concrete cylinder specimens, all obtained from the same batch, were tested both under static and high strain rate conditions. 15 cylinder specimens were tested under $3.55x10^{-5}$, $3.23x10^{-4}$, $2.97x10^{-3}$ 1/s strain rates, whereas three identical specimens were tested using a Split Hopkinson Pressure Bar (SHPB) test setup under 235, 245, 260 1/s strain rates. Used SHPB setup was modified to include quartz crystal stress sensors, so that the stresses developed in the specimens were directly obtained, eliminating common issues regarding stress readings in a conventional setup. Stress-strain behavior and other material parameters that would be necessary for numerical modeling were obtained under various strain rates. Test samples were modeled using an explicit finite element program LS-DYNA, using Holmquist-Johnson-Cook model with experimentally obtained model parameters. To verify the obtained parameters further, drop tower test on concrete plates were also performed and modeled. Numerical modeling of both SHPB samples and concrete plates were successful in capturing the observed behavior. The study also provided the literature with a reliable test data with complete parameters that can be used for further studies in the area.

ÖZET

BETONARMENİN YÜKSEK HIZLI ŞEKİL DEĞİŞTİRME KOŞULLARI ALTINDA DOĞRUSAL OLMAYAN SONLU ELEMANLAR YÖNTEMİYLE MODELLENMESİ

Bu çalışmada, betonun yüksek hızlı şekil değiştirme koşulları altında modellenmesi için kapsamlı bir deneysel ve sayısal çalışma yapılmıştır. Aynı karışımdan elde edilen silindirik beton numuneleri hem statik hem de yüksek hızlı şekil değiştirme koşullarında test edilmiştir. Statik testler toplam 15 silindirik numune üzerinde ve $3.55x10^{-5}$, $3.23x10^{-4}$ ve $2.97x10^{-3}$ 1/s şekil değiştirme hızlarına sahip olacak şekilde yapılmıştır. Ayrıca üç özdeş numune kullanılarak Split Hopkinson Basınç Barı (SHBB) testleri 235, 260, 245 1/s şekil değiştirme hızlarında tamamlanmıştır. Kullanılan SHBB düzeneği, piezo-elektrik kuartz kristal alıcıları kullanılarak modifiye edilmiş ve bu sayede numunelerde oluşan gerilmeler klasik düzeneklerdeki gerilme verisi tespiti aşamasında karşılaşılan yaygın sorunlar aşılarak doğrudan numune çubuk arayüzlerinden okunabilmiştir. Numerik modelleme için gerekli gerilme-şekil değiştirme davranışı ve diğer malzeme parametreleri farklı şekil değiştirme hızları altında tespit edilmiştir. Numuneler, sonlu elemanlar analiz programı LS-DYNA ile parametreleri deneysel olarak belirlenmiş malzeme modeli Holmquist-Johnson-Cook (HJC) kullanılarak modellenmiştir. Elde edilen malzeme modeli parametrelerinin doğruluğunun teyit edilmesi amacıyla prizmatik beton plakalar ile düşen ağırlık testleri ve nümerik analizleri yapılmıştır. SHBB ve düşen ağırlık nümerik analizleri gözlemlenen deneysel davranışı başarıyla temsil edebilmiştir. Çalışma aynı zamanda güvenilir deneysel verilerini tüm parametreleriyle barındırmasıyla literatüre latkı sağlamış olup bu alanda gelecekte yapılacak çalışmalarda kullanılabilecektir.

TABLE OF CONTENTS

LIST OF FIGURES

LIST OF TABLES

Table **Page**

CHAPTER 1

INTRODUCTION

1.1 General

Structures might be exposed to high loading rates due to impact and blast loading throughout their lifespan. Explosions at military or industrial buildings, vehicle collisions to bridge piers and rock-fall to barriers in transportation structures, impact loads owing to sea waves can be listed as examples of extreme loadings on structures. Such loading effects can produce high strain rates on the structural material since they occur in very high magnitudes in a very short period of time. Materials exhibit considerably different behavior at high strain rates compared to their quasi-static behavior. To obtain sensitive and accurate analysis results of structures subjected to extreme loadings, it is important to formulate the material behavior under high strain rates. For this purpose, many researchers have investigated the behavior of structural materials under high strain rate conditions, including reinforced concrete (RC).

Split Hopkinson Pressure Bar (SHPB) setup is a commonly used test method to investigate the behavior of concrete at high strain rates. A large number of SHPB tests have been reported in the literature on concrete. However, due to complex nature of testing conditions, reported test results often contain problems with the stress homogeneity in the specimens and interpretation of readings using one dimensional wave theory. Moreover, in brittle materials including concrete, it is difficult to determine the stress developing on the material due to the probability of premature failure. On the other hand, in each individual study performed, all the parameters that would be required in a numerical modeling were usually not gathered, creating problems when these studies are used to develop or calibrate numerical models for concrete under high strain rate conditions.

In this study, the behavior of concrete at both high and low strain rates were investigated and significant parameters for numerical modeling of concrete under high strain rates were determined through an experimental and numerical program. High strain rate tests of concrete were conducted using a modified SHPB setup, testing three

cylindrical specimens of 45 mm length and 39.5 mm diameter under 235, 245, 260 1/s strain rates. The stresses at the specimen faces were obtained not only by indirect measurement of strain gauges on aluminum bars as they are in a conventional SHPB apparatus, but also through direct measurements provided by a modified SHPB setup with piezoelectric quartz crystals mounted on the bar-specimen interfaces. By this way, strength enhancement of concrete under high strain rates could be determined in high precision. In addition, 15 static tests were performed at 0.0045, 0.045 and 0.45 mm/s cross head speeds with specimens that had identical geometry with those tested under high strain rates using SHPB setup. Specimens tested under static and high strain rates were all obtained from the same concrete batch, ensuring a reliable comparison between quasi-static and high strain behavior of exactly identical specimens. Performed high strain rate tests were also modeled in LS-DYNA which is an explicit nonlinear finite element software. In the numerical study, Holmquist-Johnson-Cook (HJC) material model was used. The model parameters in the material model were determined from the test results.

Finally, to verify the obtained parameters of the material model, drop tower tests were conducted and numerically modeled in LS-DYNA. For this purpose, six prismatic specimens with 200x200x20 mm dimensions were cast from the same batch with cylindrical specimens. Three of the specimens were tested by releasing a striker having 15.68 kg mass with an impact velocity of 1 m/s while the rest of the specimens were tested by 3 m/s. These tests were modeled in LS-DYNA by using HJC material model.

1.2 Literature Review

Determination of mechanical properties of concrete under high strain rates has been a subject of numerous studies. Malvern et al. (1985) conducted one of the first significant experimental SHPB studies about the concrete behavior under high strain rates. In this study, effect of aggregate size and their types in the specimen were investigated experimentally. Throughout the dynamic tests, strain rates varied between 10 and 100 1/s and cylindrical specimens had length-to-diameter (L/D) ratio of 1. In total, four different aggregate types were used for high strength (97 MPa) concrete mixes. Three of them had a maximum aggregate size of 12.5 mm while the last type had 9.5 mm. A clear strength increase was reported for all concrete types while researchers

posed a new question about the possibility of observed strength increase being associated with lateral inertia confinement.

Ross (1989) conducted tests by three different types of high strain rate tests as: direct tension, direct compression and split cylinder (indirect tension) tests by SHPB setup. Concrete specimens had 51 mm length and diameter having an L/D ratio of 1. Maximum aggregate size was selected to be 9.5 mm in the specimens. From the results, it was found out to be strain rate sensitivity of direct tension tests were two to four times greater than that of compression tests at identical strain rates. In the study it is mentioned that compressive tests stress homogeneity along the specimen length was provided.

Bischoff and Perry (1991) published a review paper which investigates the experimental studies that have been performed until the beginning of 1990s. The available literature about uniaxial compressive behavior of concrete material under high strain rate was investigated in the study. Collected data on concrete strength variation by strain rate is presented in Figure 1.1.

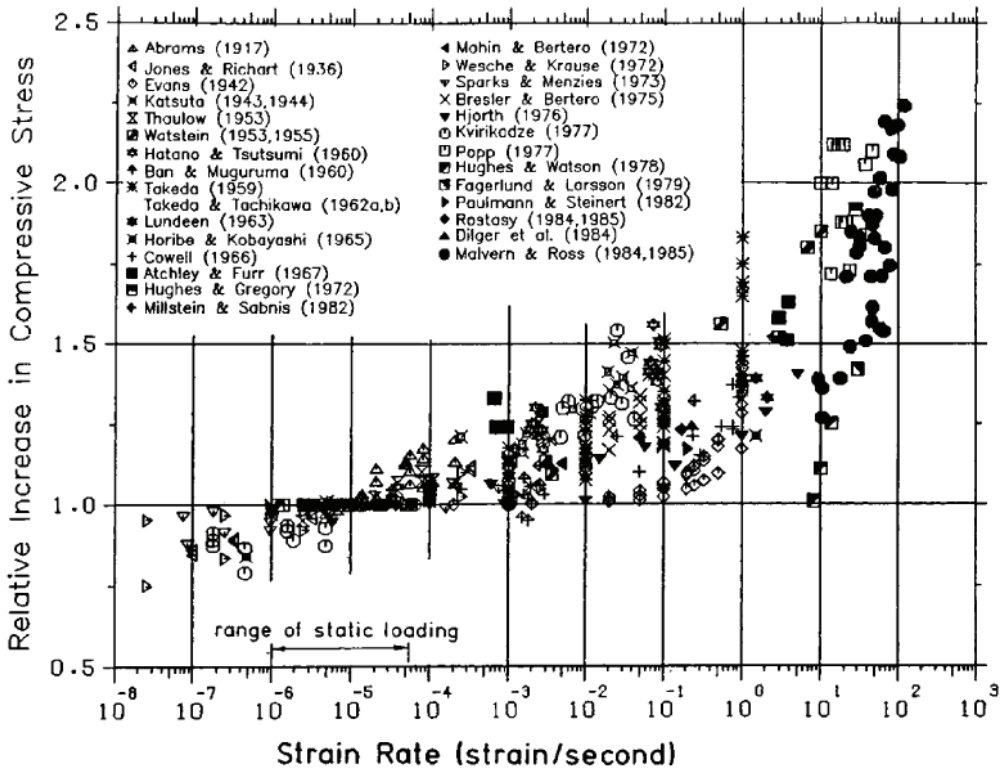

Figure 1.1. The change in concrete strength by strain rate
(Source: Bischoff and Perry, 1991)

From the collected test results, a logarithmic strength enhancement was observed by increasing strain rate. On the other hand, reasons of strength enhancement was also discussed, and strain-rate dependence of tensile micro-fracture and transition from uniaxial stress state to uniaxial strain by lateral inertia confinement were counted as possible reasons. It is concluded with an observation that, failure strain, strength, elastic modulus and Poisson's ratio increased by increasing strain rate in the vast majority of the studies.

Tedesco and Ross (1998) followed an experimental program to investigate the static and dynamic properties of concrete. For this purpose, direct compression and split tensile tests were performed on cylindrical concrete specimens having a length and diameter of 51 mm. For quasi-static tests, strain rate range was selected to vary from 10^{-7} to 10^{-5} 1/s while it was varied from 10^{-1} to 10^{3} 1/s for dynamic tests. Approximately 60 direct compression and 70 split tensile tests were conducted under high strain rates by means of an SHPB setup. From results, a critical strain rate was detected after which a significant strength increase was observed. These levels were pointed out to be 2 and 60 1/s for tension and compression, respectively. Material characterization results were then statistically analyzed and strain rate dependent constitutive equations for both tension and compression were developed in the study. Finally, developed constitutive equations were used to modify a hypo-elastic based nonlinear material model in ADINA finite element software.

Grote and Zhou (2001) focused on dynamic characterization of mortar and concrete material. For this purpose, quasi-static, SHPB and direct impact tests were conducted on circular specimens. Quasi-static tests were performed on specimens having a 76.2 mm diameter, a 152.4 mm length (L/D=0.5) and compressive strengths were detected as 30 and 46 MPa for concrete and mortar, respectively. Afterwards, SHPB tests were held on mortar specimens that ranged from 250 to 1700 1/s strain rate. The specimens had various L/D ratios with two specific diameters; either 19.05 or 12.70 mm. In the study, mortar was reported to exhibit rate-sensitive behavior in the range of 10^{-3} -1700 1/s and specifically above the strain rate of 400 1/s. Plate impact tests were performed on both concrete and mortar specimens with the dimensions of 76.2 mm diameter and 10 mm thickness. Projectile velocities varied between 277 and 330 m/s caused an average strain rate at the specimen on the order of 10^{4} 1/s with 1-1.5 GPa confining pressure. Average compressive strengths of mortar specimens at specific (290

and 330 m/s) impact velocities was detected to be 1.2 and 1.3 GPa, respectively, and identical impact velocities to the concrete specimens resulted in 1.55 and 1.7 GPa average compressive strength. Results indicated that the stress levels were at least eight times higher than those of SHPB tests, and high strain rate effect with lateral confining pressure (~1 GPa) was regarded as the cause of the increase in strength.

Li and Meng (2003) performed numerical analyses on concrete-like materials by SHPB setup simulations. The study basically concentrated on the source of strength enhancement of concrete material under high strain rates. Finite element (FE) simulations were conducted by ABAQUS/Explicit code using Drucker-Prager material model (Drucker and Prager, 1952) for concrete. This material model was plasticity based pressure dependent and strain rate insensitive model. Throughout the analyses, three different slenderness ratios (L/D) were investigated as 0.33, 0.5 and 1. From the results, it was seen that, in the range of selected slenderness ratio results did not vary significantly. On the other hand, a further analysis was made on the specimen with L/D ratio of 0.5. For this purpose, problem was solved at two different nominal strain rates as 27 1/s and 390 1/s. Hydrostatic pressure was found out to be one-third of uniaxial compressive stress in the 27 1/s test, and this finding yielded to a conclusion that there is no confinement effect caused by other two principle stresses (Figure 1.2).

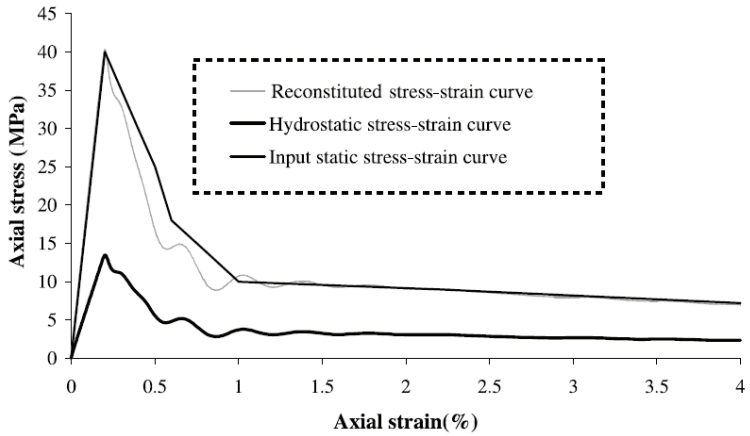

Figure 1.2. Axial stress and hydrostatic stress against axial strain at a strain rate of 27 1/s (Source: Li and Meng, 2003)

On the other hand, in the 390 1/s test, hydrostatic pressure was observed to be almost equal to uniaxial compressive strength and ultimate compressive strength was almost twice the quasi-static strength (Figure 1.3).Therefore; the study was concluded

that strength enhancement was strongly influenced by hydrostatic pressure due to lateral confinement effect.

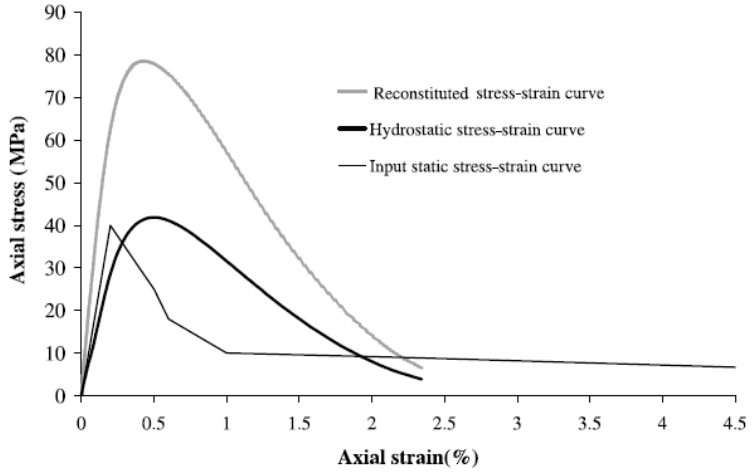

Figure 1.3. Axial stress and hydrostatic stress against axial strain at a strain rate of 390 1/s (Source: Li and Meng, 2003)

In order to understand the source of strength increase of concrete specimens tested by SHPB setup, studies were carried on to determine how the strength affected from different aspect ratios of specimens, bar-specimen friction interaction and the aggregates contained in the sample. The work of Hao et al. (2011) is one of the studies that have been made under this area. Authors have stated that empirical strength enhancement functions, which were proposed in the literature, are often suggested for concrete-like (aggregate-free or mortar) materials, and these functions may give inaccurate results for concrete. On the other hand, it has been mentioned that almost no studies conducted in previous years which have examined the effect of aggregates on the increase in material strength systematically. As a result, numerical studies were carried out by AUTODYN software at various volumetric percentages of aggregates (20%, 30% and 40%), and an analytical formulation was proposed to modify the previously obtained empirical strength enhancement functions under aggregate variability.

Two years later Hao et al. (2013) have conducted numerical and experimental studies to investigate the lateral confinement effect of the friction at the specimen-bar surfaces. Mesoscale numerical models with distinctive evaluation of various components in concrete specimens were created by AUTODYN software and analysis

were conducted parametrically (Figure 1.4). Five different friction coefficients and three different aspect ratios (0.5, 1 and 2) were selected.

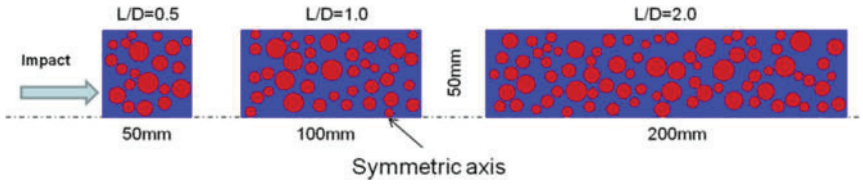

Figure 1.4. Mesoscale models with various L/D ratios

Under these conditions, parameters such as aspect ratio, coefficient of friction and strain rate significantly affected the stress-strain relation and fracture mechanisms of concrete. Finally, they proposed an empirical formulation which removes frictional effects from previously obtained empirical strength enhancement functions due to the fact that in experimental applications aforementioned effects could not be eliminated.

In the study of Guo et al. (2017) a test program was conducted on dynamic compressive behavior of high-strength concrete. Specimens had three different strengths (60, 80 and 110 MPa) with 10 mm maximum aggregate size and Φ 77 x 40 mm cylindrical geometry. High strain rate tests were performed to be in the range of 40-110 1/s throughout the tests. Figure 1.5 presents the variation of the dynamic increase factor (DIF). DIF is the ratio of dynamic strength to quasi-static strength and usually used to evaluate the strain rate sensitivity of the concrete. From the figure it can be observed that 60 and 80 MPa strength concretes were much more sensitive to strain rate compared to that of 110 MPa concrete. A comparison is made between the CEB-FIB (2010) and experimental data. It is observed that CEB-FIB (2010) equation fits better in normal strength concrete. FE code ABAQUS Explicit was also used to simulate SHPB tests on high strength concrete specimens. In the simulation, axisymmetric models were created using the concrete damage plasticity model. Strain rate dependence of material model was provided by scaling static response using DIF determined from tests. According to analysis results, it was seen that FE model based on quasi-static mechanical properties and including DIF obtained from experimental study is able to simulate SHPB tests and concluded that DIF values are reasonably representative.

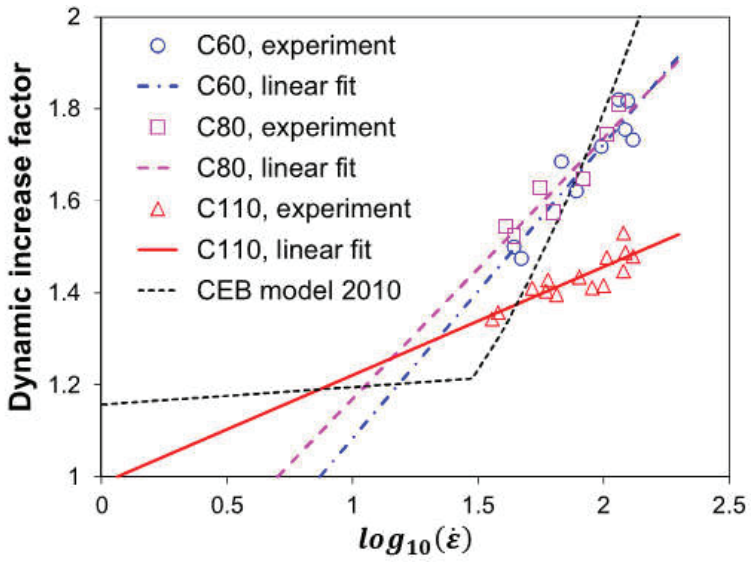

Figure 1.5. Dynamic increase factor of high strength concrete
(Source: Guo et al., 2017)

Table 1.1 summarizes loading methods, specimen sizes and range of strain rates presented in the mentioned studies with additional literature.

Table 1.1. The basic studies examining high strain rate behavior of concrete and reinforced concrete

Referrence	**Test Type**	**Specimen Size (diameter x length) (mm)**	**Strain Rate (1/s)**
Malvern, L. E. Et al. 1985.	SHPB	Φ76 x 76 Φ76 x 66	59 - 118
Jawed, I. et al. 1987.	Hydraulic and SHPB	Φ6.35 x 9.5 Φ12.7 x 19.1 Φ19.05 x 28.6	10^3
Gran, J. K. et al. 1989.	400 MPa explosive gas loader	Φ150 x 300	0.5 - 10
Ross, C. A. et al. 1989.	SHPB	Φ51 x 51	20 – 190
Tedesco and Ross 1998	SHPB	Φ51 x 51	10^{-1}-10^3
Grote and Zhou 2001.	SHPB and plate impact	Φ76.2 x 10 Φ12.70 x Varies Φ19.05 x Varies	250-1700 and 10^4
Wang, S. et. al. 2011	SHPB	Φ 77 x 38	10-300
Su, H. et. al 2014	SHPB	Φ 100 x 50	20-120
Xiao, J et. al 2015	SHPB	Φ 70 x 35	10-100
Deng, Z. Et. al 2016	SHPB	Φ 70 x 35	70-140
Guo et. al 2017	SHPB	Φ 77 x 40	40-110

There are also numerous numerical studies available in the literature on modeling the high strain rate response of concrete members. Magnusson et al. (2010) conducted FE simulation of RC beams exposed to air blast loading by ANSYS AUTODYN explicit solver. A previous experimental test program of authors was taken as reference source for the analyses. In simulations, beams with normal-strength (NSC) and high-strength concrete (HSC) were investigated and Riedel, Hiermaier and Thoma (RHT) material model (Riedel et al., 1999), which is a constitutive model including tensile failure criterion, was used. Strain rate sensitivity was introduced for both tensile and compression strength by an empirical function of a dynamic increase factor (DIF) offered by CEB (1990). Steel reinforcements were defined by means of both Johnson & Cook (Johnson and Cook, 1983) and modified Johnson & Cook material models (Westerling, 2005). In the study, an attempt to estimate the failure modes of beam members were made since such mechanisms are directly related with energy absorption capacity of an RC member. According to results of analyses, FE simulations with RHT model associated with a bi-linear crack softening model of concrete in tension is well suited for dynamic structural analysis of NSC and HSC members.

Lin et al. (2014) conducted numerical analysis of reinforced concrete slabs under blast effect using nonlinear finite element code LS-DYNA. In the study, geometrical and mechanical properties of slabs were taken from experimental studies in the literature. For this purpose, four slabs with three different geometrical configurations were selected. All slabs had an average concrete compressive strength of either 48 MPa or 40 MPa. Karagozian & Case Concrete Model-Release III (LS-DYNA Manual, 2014), which is a plasticity based and strain rate sensitive material model, was selected for concrete. Strain rate sensitivity was included for both tensile and compression strength through a DIF function offered by CEB (1990). Reinforcement bars were also modeled using a strain rate sensitive material model (Plastic Kinematic Model) in the simulation. Maximum center point deflections obtained from the experimental study and numerical analyses were compared with each other. Discrepancies did not exceed 11%, and the authors emphasized that the used FE model is effective and accurate for modeling the structural members such as slabs under high strain rate conditions.

Li et al. (2014) performed a parametric study on RC columns under blast loading. Parameters to be investigated were selected to be the length and depth of the

columns with variable longitudinal and shear reinforcement ratios. In order to simulate the behavior of columns, the model was initially attempted to be calibrated by means of a tested column. However, due to lack of column spall damage observation in the literature, an RC slab was selected for calibration. Once the model was calibrated, FE model of columns were built. The FE software (LS-DYNA), material model (Karagozian & Case Concrete Model-Release III) and strain rate sensitivity model were selected to be identical to the study mentioned above. Columns were subjected to identical blast loading scenarios in each set of analysis. It was observed that the spall damage was independent of flexural stiffness. It was discussed that spall damage occurred in a very short period of time before columns structurally responded to the blast load. On the other hand, longitudinal reinforcement ratio and depth of column were found to be parameters that have significant effects on spall damage by mitigating the damage.

The importance of behavior change of concrete and concrete like materials under high strain rates can be observed from the presented literature. However, these SHPB tests failed to achieve a commonly accepted DIF function which can reflect the true behavior of concrete under high strain rate conditions. As a result, numerous different models were developed and used to model concrete under high strain rates, each of which may give significantly different results. From this point of view, the proposed study will be one of the important and rare studies which investigate this problem using both experimental and numerical techniques through following a static and dynamic mechanic characterization methodology aiming to eliminate deficiencies in the present literature.

1.3 Thesis Organization

Following this chapter, Chapter 2 starts with the introduction of Holmquist-Johnson-Cook (HJC) material model theory. Concrete material characterization was described and determination of material properties followed. Later, numerical simulation of Split Hopkinson Pressure Bar (SHPB) to investigate the accuracy of detected material model parameters was presented in this chapter.

In Chapter 3, drop tower tests of six prismatic concrete specimens were presented, which were exposed to various boundary conditions and impact velocities.

Presentation started with description of test setup and continued by test results and discussion sections. Finally, chapter is closed by damage evaluation of specimens.

Chapter 4 starts with a detailed explanation of drop tower simulations. Obtained force histories both from tests and numerical analyses were compared. Discussion ends with a comparison of final state FE model crack prediction with those of tests. Accuracy of mechanical characterization and behavior of material under various strain rates, although relatively lower strain rates compared to SHPB, could be observed.

A brief summary and evaluation of tests and numerical studies were presented in Chapter 5. Recommendations for future studies were also presented in this chapter.

CHAPTER 2

CHARACTERIZATION OF CONCRETE MATERIAL

2.1 Introduction

In this chapter, theory of Holmquist-Johnson-Cook (HJC) material model and determination of material model parameters will be presented in detail. Afterwards, a numerical simulation of Split Hopkinson Pressure Bar (SHPB) to investigate the accuracy of determined material model parameters will be presented.

2.2 Theory of Material Model

Holmquist-Johnson-Cook model is well suited for concrete exposed to large strains, high strain rates and pressure. Additionally, theoretical background of the model is relatively simple and most of the significant cases of concrete behavior such as pressure, rate dependency, compaction and damage cracking are considered in the model. HJC is an elastic-viscoplastic material model and material response is expressed by deviatoric and hydrostatic stress contributions. The deviatoric stress response of concrete material is presented in Figure 2.1.

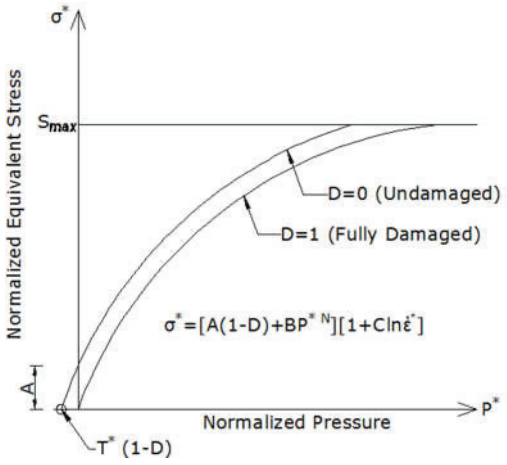

Figure 2.1. Deviatoric stress representation of HJC model with respect to normalized pressure (Source: Holmquist et al, 1993)

In the figure, vertical axis σ^* is the normalized equivalent stress defined by (σ/f'_c) where σ and f'_c denotes equivalent stress and uniaxial compressive strength of concrete material, respectively. Horizontal axis P^* is the normalized hydrostatic pressure given by (P/f'_c) where P denotes pressure. Normalized equivalent stress is expressed by functions of strain rate and pressure given by Equation (1).

$$\sigma^* = [\mathrm{A}(1-\mathrm{D}) + \mathrm{B}P^{*\,\mathrm{N}}][1 + \mathrm{C}\ln\dot{\varepsilon}^*] \leq \mathrm{S}_{\max} \quad (1)$$

In the equation, A, B, N and C are material constants which represent normalized cohesion strength, normalized pressure hardening, pressure hardening exponent and strain rate sensitivity, respectively. $\dot{\varepsilon}^*$ is the normalized strain rate, given by $\dot{\varepsilon}^* = \dot{\varepsilon}/\dot{\varepsilon}_0$ where $\dot{\varepsilon}$ is the strain rate and $\dot{\varepsilon}_0$ is the reference strain rate. D is the scalar damage variable resulting in reduction of the cohesive strength which ranges from 0 to 1. S_{max} is the maximum strength obtained by normalization of equivalent strength by uniaxial compressive strength f'_c.

The damage model of material is defined in terms of equivalent plastic strain and equivalent volumetric plastic (compaction) strain and given by Equation (2).

$$D = \sum \frac{\Delta\varepsilon_p + \Delta\mu_p}{f(P)} \quad (2)$$

In the equation $\Delta\varepsilon_p$ and $\Delta\mu_p$ are the equivalent plastic strain increment and equivalent volumetric plastic strain increment, respectively and $f(P)$ is the plastic strain to fracture under a constant pressure, P with the specific expression $(P^* + T^*)^{D_2}$ where D_1, D_2 are damage constants. T^* is the normalized hydrostatic tensile strength, as shown in Figure 2.2 . In the figure, lower $\varepsilon_{p\ min}^{f}$ limit is provided to ensure sufficient plastic strain which will prevent fracture due to low magnitude of tensile waves.

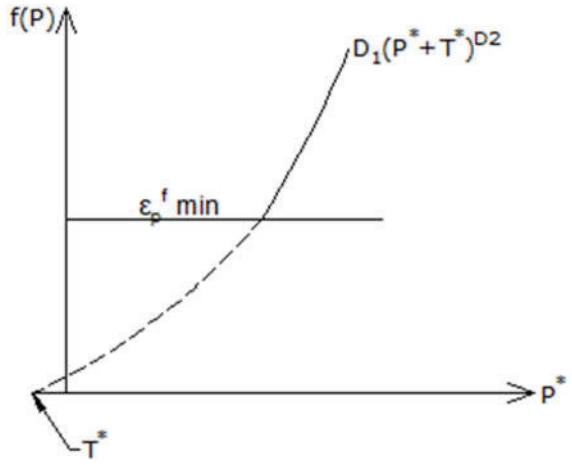

Figure 2.2. Damage model owing to effective plastic strain
(Source: Holmquist et al, 1993)

Volume-pressure (compaction) interaction is presented schematically in Figure 2.3.

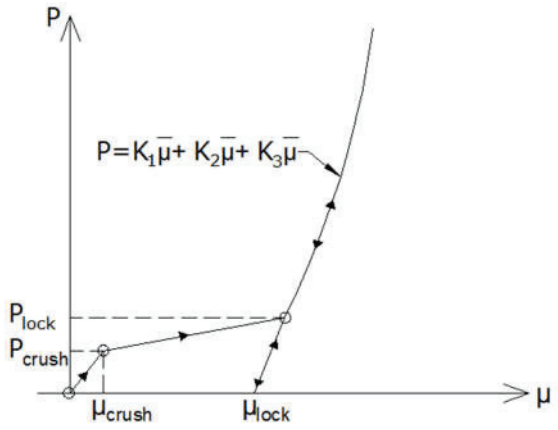

Figure 2.3. Volume-pressure interaction of HJC model
(Source: Holmquist et al, 1993)

In the figure, horizontal axis μ denotes volumetric strain, and vertical axis P represents hydrostatic pressure. In the axes the nodes P_{crush} , P_{lock} denote for crushing and locking pressure while μ_{crush} and μ_{lock} represent crushing and locking volumetric strains. Pressure-volume relation is evaluated in three regions. The first region is the linear elastic zone ($P \leq P_{crush}$) which can be expressed by elastic bulk modulus and defined as $K_{elastic} = P_{crush}/\mu_{crush}$. The second region is of a transition ($P_{crush} \leq P \leq P_{lock}$) from elastic to fully damaged concrete by air voids progressively extract from the

concrete and result with increase of plastic volumetric strain. Finally, the third region is fully compact zone ($P > P_{lock}$) and material assumed to be completely damaged and dense without tensile strength. The function of pressure is represented by $P = K_1\bar{\mu} + K_2\bar{\mu} + K_3\bar{\mu}$ where K_1, K_2 and K_3 are the material constants that is used to fit an equation to the hydrostatic pressure and shock Hugoniot data, and $\bar{\mu}$, the modified volumetric strain, is given by Equation (3). Shock Hugoniot data is a method of describing the relationship between the states on both sides of a shock wave in a 1D deformation in solids, and obtained by plate impact tests which generates very high strain rates and high pressures over the specimens.

$$\bar{\mu} = \frac{\mu - \mu_{lock}}{1 + \mu_{lock}} \quad (3)$$

2.3 Material Characterization and Determination of Model Parameters

Material characterization of concrete will be explained in this section. Discussion starts with the concrete mixture for production of concrete specimens. Quasi static tests at different strain rates follow. SHPB tests are presented afterwards and finally section is closed with a verification work of obtained material model constants by a numerical SHPB model.

2.3.1 Concrete Material

To obtain the required strength and quantity, a mix design for 130 liter concrete was performed. Concrete volume consists of approximately 75% by the aggregates (Erdoğan, 2013). Moreover, aggregates considerably contribute to the mechanical properties of concrete. Generally, aggregates have brittle and high strength nature. Durable and stiff aggregates also resists to the corrosive environmental influences. Additionally, workability properties and ingredient proportions of concrete mix will be highly affected by aggregates. As a result, detection of aggregate properties such as grading, maximum aggregate size, and water absorption capacity become an important issue. Among these properties, grading of aggregate was checked first. This procedure was performed by following ASTM C 136 code, which presents a test method for sieve

analysis. Using this sieve analysis method, the distribution of particle size of coarse/fine aggregates and maximum aggregate size can be determined.

In Figure 2.4, the gradation curve obtained from used aggregates are presented, including ASTM upper and lower limiting curves for coarse and fine aggregates. The maximum aggregate size (D_{max}) is observed to be 4.75mm. In the literature, concrete material is defined as a mortar mixture which also includes coarse aggregates (Erdoğan, 2013). According to ASTM C 125 code 4.75mm aggregate size is the separation point between coarse and fine aggregates. Therefore the mixture used in the specimen can be classified as concrete since it contains coarse aggregates.

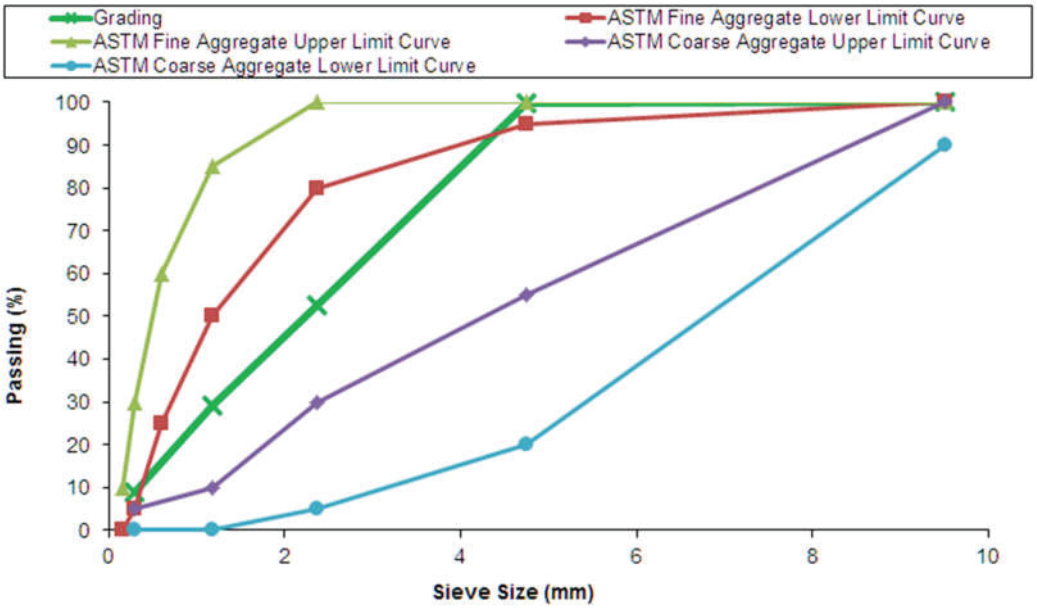

Figure 2.4. Aggregate gradation curve

Saturated surface-dry (SSD) bulk specific gravity, ratio of material density to water density, was determined according to ASTM C 127 code and obtained as 2.56. Water absorption capacity and moisture content of the aggregates were also determined and presented in the Table 2.1.

Table 2.1. Aggregate physical properties

Physical Property	
SSD Bulk Specific Gravity	*2.56*
Water absorption (%)	*3.9*
Moisture Content	*Dry*

The quality and amount of cement directly affects the mechanical strength of concrete. In this study, Portland cement CEM I 42.5R was used. ACI 211.1 was followed to calculate the concrete mix ingredient proportions considering slump, maximum aggregate size, mixing water weight, air volume, water/cement (W/C) ratio, cement weight, and aggregate amount. 150 mm to 175 mm slump was selected due to casting the concrete to the relatively small prism formworks. A maximum aggregate size of 4.75 mm was selected, which is large enough to classify the mixture as concrete and small enough not to violate 1/10 ratio of aggregate to specimen diameter at the SHPB tests. Required mix water amount in a meter cube concrete was determined from the table given in ACI 211.1 depending on chosen maximum aggregate size. W/C ratio was selected as 0.40 mainly based on the aimed strength of concrete and cement amount in a meter cube concrete was calculated accordingly.

130 liter concrete batch was produced for specimens. From the produced concrete; prism (45x45x220 mm), standard cube (150x150x150 mm) and cylinder (150 mm diameter with 300 mm length) specimens were taken and kept in water cure for 28 days. Concrete strength tests at 28^{th} day were performed by using a hydraulic press device. For this purpose five standard cylinder specimens were selected from the batch. Results are presented in Table 2.2.

Table 2.2. Compressive strength of standard cylinder specimens

Specimen	Cylinder #1	Cylinder #2	Cylinder #3	Cylinder #4	*Cylinder #5*
Concrete at 28^{th} day	*23.66*	*30.76*	*33.33*	*27.5*	*28.75*
Average Strength	*28.8 MPa*				

Concrete specimens that were used for static and dynamic characterization tests were cut precisely by core drills to have aimed geometry (Figure 2.5). Specimen surfaces must be parallel to each other. This is a significant parameter which effects the

test results of a material like concrete that have relatively low failure strain value of about 0.2%. Surface irregularities cause non-homogenous stress distribution over the specimens. Therefore, specimen surfaces were polished and ensure to have perfectly parallel faces.

(a) Concrete specimen

(b) Core drill

Figure 2.5. Precisely cut specimen

2.3.2 Static Tests

Static tests were performed at Dynamic Testing and Modeling Laboratory of Izmir Institute of Technology. Shimadzu AG-X universal testing machine, which has a tension and compression capacity of 300 kN, was used for the quasi-static tests (Figure 2.6).

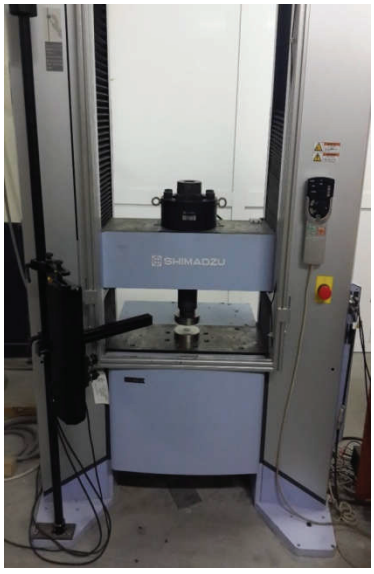

Figure 2.6. Shimadzu AG-X Testing Machine

In the quasi static tests, strain rate is directly related with cross head speed of the testing device. Therefore, three different cross head speeds were selected as 0.0045, 0.045, and 0.45 mm/s. Six specimens were tested with a cross head speed of 0.0045 mm/s, and data was recorded once a millisecond (ms) for Test 1, 2 and 3, while it was once every 30 ms, 300 ms and 200 ms for Test 4, 5 and 6. During tests, force, time and displacement variables were recorded, and the data obtained from Test 1 is shown in Figure 2.7 as a typical example. While force and time values were gathered directly from testing machine, deformation of specimen was followed both by a video extensometer and cross-head displacement. Video extensometer followed the stickers placed on the specimen and recorded the change in gauge length. However, cross-head displacement, which is also known as stroke, not only recorded the change in length of specimen but also all other elastic components of testing device. Therefore, as it can be observed from the figure, displacement measurement exhibits a significant difference between two measurement methods.

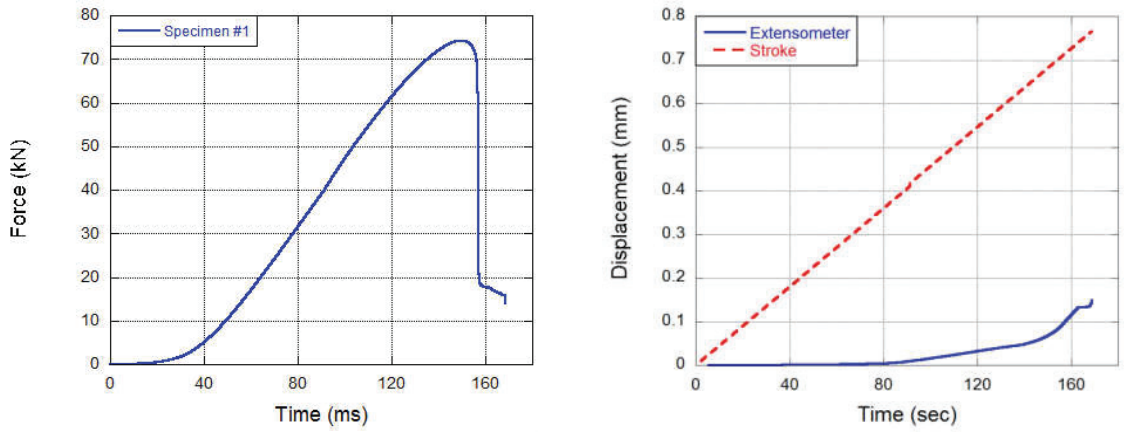

(a) Force history (b) Displacement history

Figure 2.7. Variable histories of Test 1

Strain measured from video extensometer was used for these tests since solely the change in gauge length is taken into account. Obtained stress-strain curves are presented in Figure 2.8. In tests 4 and 5, post-peak strains were not captured since stickers placed on the specimens have fallen due to crushing of concrete in these tests.

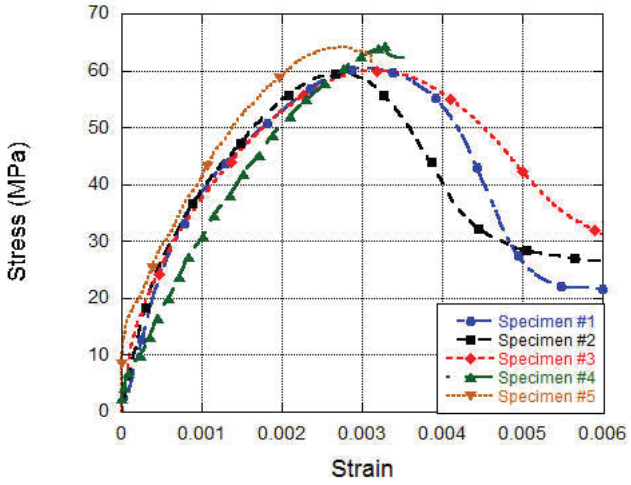

Figure 2.8. Stress-strain curves of quasi static tests with 0.0045 mm/s cross head speed

Failure stresses and corresponding strain values are presented in Table 2.3. It can be observed that, stress and strain values does not varies significantly for the five tests and results in an average strength of 62 MPa.

Table 2.3. Stress and strain values at failure

Specimens	#1	#2	#3	#4	#5
Strength (MPa)	*60.5*	*60*	*60*	*64.5*	*64*
Failure Strain	*0.003*	*0.0027*	*0.0031*	*0.0032*	*0.0029*

One additional specimen was tested under this cross head speed using strain gauges glued on the specimen parallel to the specimen axis, to measure the strains directly and to obtain the actual strain rate of the specimen (Figure 2.9).

Figure 2.9. Strain gauges glued on the axial and circumferential directions of the specimen

A strain gauge glued at the mid height of the specimen in transverse direction was also used to measure circumferential strains and thus obtain the Poisson's ratio. In Figure 2.10(a) Poisson's ratio is presented with stress variation against strain. For this specimen, compressive strength was found to be 62 MPa with a corresponding strain of 0.0035. Poisson's ratio was simply calculated by dividing the transverse strain to axial and obtained as 0.22 which is close to commonly reported in the literature. In Figure 2.10(b), strain-time curve is presented which was used to calculate the strain rate. For this purpose a linear fit was created and then the slope of the fit was considered to be the average strain rate of test specimen, which is found to be 3.55×10^{-5} 1/s. Average compression strength of six concrete specimens was detected to be 62 MPa.

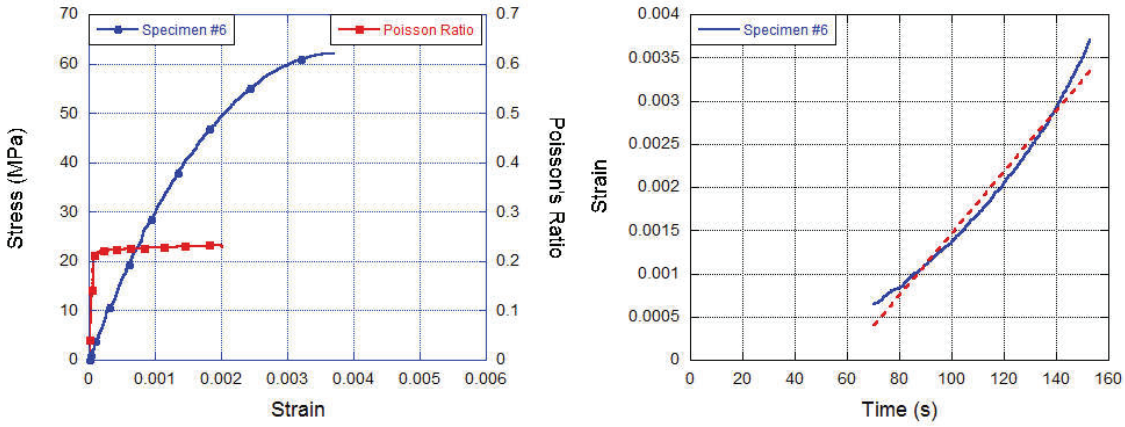

(a) Stress-strain curve and Poisson's ratio of material

(b) Strain history

Figure 2.10. Specimen with strain gauge at with 0.0045 mm/s cross head speed

Next, six tests were conducted with a cross head speed of 0.045 mm/s. Deformation measurements of five tests were performed by following the stickers located on the specimen with video extensometer similar to the previous test set. Gauge lengths of the specimens were measured to be: 20.38, 20.13, 20.23, 22.95 and 22.82 mm for the first, second, third, fourth and fifth specimens, respectively. Stress-strain relationships and stresses with corresponding strains are presented in Figure 2.11 and Table 2.4, respectively. According to results, it is understood that strength of concrete material did not vary significantly. However, failure strains of specimens tend to vary between 0.0022 and 0.0037.

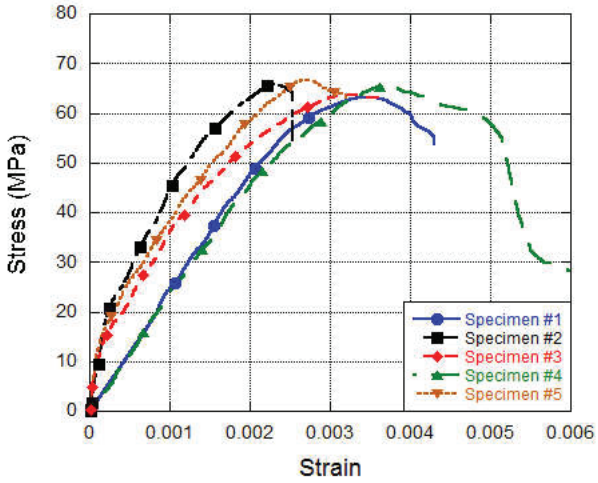

Figure 2.11 Stress-strain curves of quasi static tests with 0.045 mm/s cross head speed

Table 2.4. Stress and strain values at failure

Specimens	#1	#2	#3	#4	#5
Specimen (MPa)	*63*	*65.5*	*63.5*	*65.52*	*66.5*
Failure Strain	*0.0034*	*0.0022*	*0.0032*	*0.0037*	*0.0027*

One quasi static test at this cross head speed was performed with strain gauges on the specimen. In Figure 2.12(a) Poisson's ratio is presented with stress variation against strain, and peak stress was obtained to be 64 MPa with a corresponding strain of 0033. In Figure 2.12(b) strain is presented against time and a linear fit on the curve was created. The slope of the fit, in other words average strain rate of specimen was calculated to be 3.23×10^{-4} 1/s. Poisson's ratio of specimen was calculated following the same approach with the previous test group and obtained to be 0.19. Average compressive strength of six specimens was found to be 65 MPa.

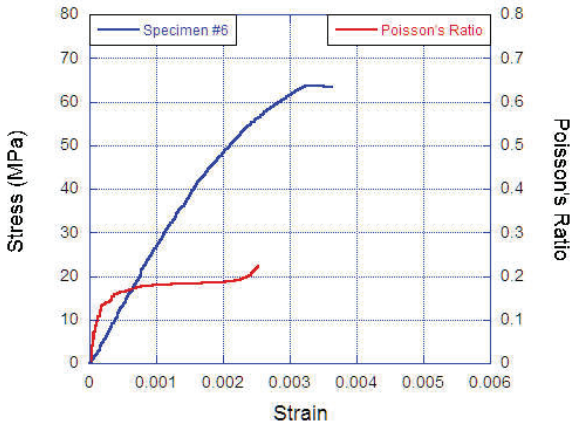

(a) Stress-strain curve and poisson's ratio of material

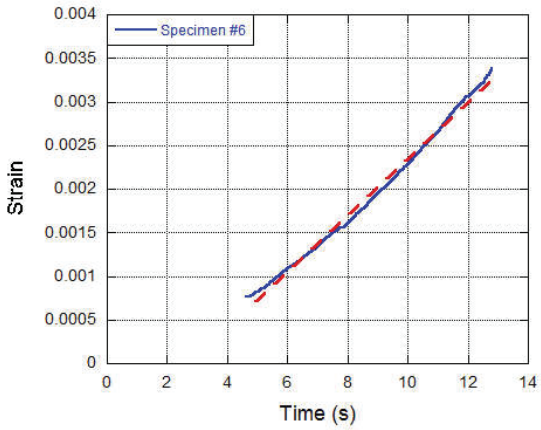

(b) Strain history

Figure 2.12. Specimen with strain gauge at with 0.045 mm/s cross head speed

Finally, three concrete specimens were tested with a cross head speed of 0.45 mm/s. Deformation measurements of first two tests were conducted with video extensometer while the last test with strain gauge. Gauge lengths were measured to be 22.33 and 21.84 mm for the first and second specimens, respectively. Obtained stress-strain curves are presented in Figure 2.13. From the figure it can be seen that the peak stresses of the specimens do not vary significantly, and failure strain values of the specimens are found out to be in close proximity to a value of 0.0024. In Figure 2.14, stress-strain and strain-time curves are presented for the final test performed with strain gauge. As it can be seen from the figure (a), strength is obtained to be 70 MPa while failure strain is 0.0036. Strain rate was found out to be 2.97×10^{-3} 1/s and a clear Poisson's ratio could not be detected due to noisy data gathered from the strain gauge located on circumferential direction. Average compressive strength of three specimens was found to be 67.50 MPa.

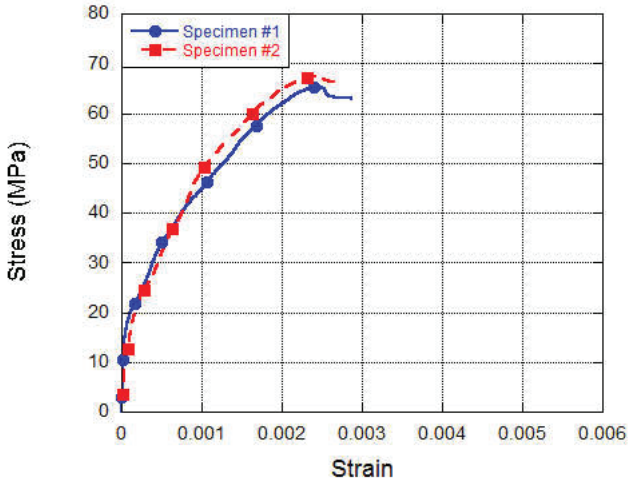

Figure 2.13 Stress-strain curves of quasi static tests with 0.45 mm/s cross head speed

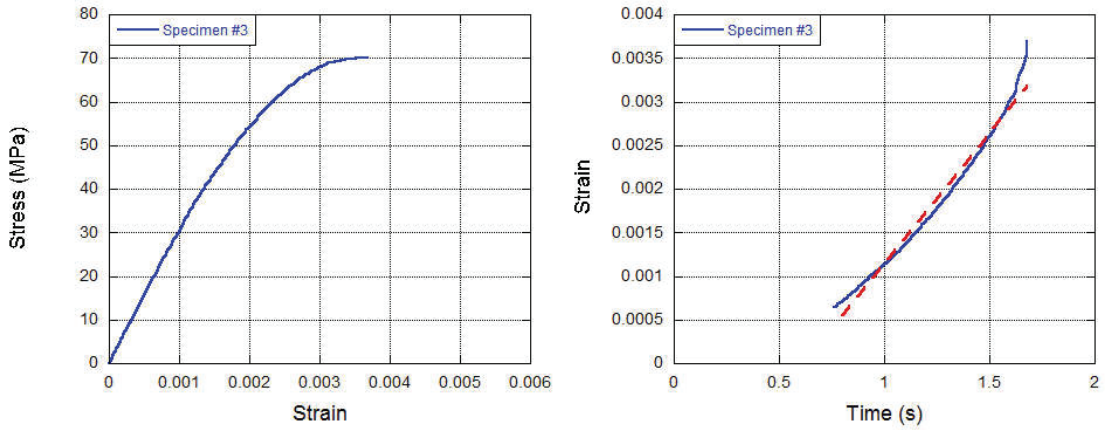

(a) Stress-strain curve (b) Strain history

Figure 2.14. Specimen with strain gauge at with 0.45 mm/s cross head speed

2.3.3 High Strain Rate Tests

High strain rate tests of concrete are performed by SHPB setup which basically consists of three bar components. These are striker, incident and transmitter bars. Concrete specimen is sandwiched between incident and transmitter bar and launched striker bar collides with incident bar. In order to launch striker bar, a gas gun is used by instant release of compressed gas. Collision speed can be easily controlled by the change of gas pressure (Figure 2.15). In conventional SHPB setup stress wave inside the bars is acquired by the strain-gages that are located on the bars. Therefore, incident

and transmission bars must stay in the linear elastic range during the tests so that surface strains of these bars are linearly associated with the stress waves inside the bars.

Figure 2.15 SHPB setup

Wave propagating along the bars are assumed not be dispersed, which also implies the validity of 1D wave theory. Dispersion is the result of 2D effects. Bars are free to move in the radial direction except restrained nodal regions and therefore bars accelerate in the radial direction as well. This leads to inertia-induced stress along the axial direction (Chen and Song, 2011). Dispersion effect can be prevented by selecting the bars sufficiently long or slender. However, during the tests, waves that propagate along the bars are still 2D inherently. Nevertheless, waves are considered as 1D while working with axial quantities through the tests.

Another important assumption is the stress homogeneity over the specimen. In other words, the stress equilibrium at both faces of the specimen must be established. Stress wave that propagates along the specimen reflects back and forward until it reaches a constant (uniform) stress state. However, wave reflection requires enough time to reach expected uniform stress state. Therefore, it is important to arrange the duration of incident loading pulse to be satisfactorily equal or longer than the time required for stress wave reflections over the specimen (Subhash and Ravichandran,

2000). Specimens with a relatively low failure strain such as concrete might fail before the stress equilibrium is established under very high strain rates. Consequently, premature failures may occur and the obtained data from the strain gages may not represent the actual compressive strength of material.

By using mentioned stress homogeneity assumption over the specimen, stress occurring at the transmitter bar face of specimen can be calculated by Equation (4). This is also known as 1-wave analysis.

$$\sigma_s(t) = E_0 A_0 \varepsilon_t(t)/A_s \qquad (4)$$

In the equations, E_0, A_s, A_0, $\sigma_s(t)$ and $\varepsilon_t(t)$ represent elastic modulus of bar, area of specimen and bar, specimen stress that is occurring at transmitter bar sides, and transmitted strain pulse, respectively. Specimen strain $\varepsilon_s(t)$ can be calculated from the integration of incident, reflected and transmitted wave by time, given by Equation (5).

$$\varepsilon_s(t) = \frac{C_0}{l_0}\int_0^t (\varepsilon_i(\mathrm{t}) - \varepsilon_r(\mathrm{t}) - \varepsilon_t(\mathrm{t}))dt \quad (5)$$

Here, C_0 represents the wave speed in the bars and l_0 is the length of the specimen while $\varepsilon_i(\mathrm{t})$ and $\varepsilon_r(\mathrm{t})$ denote incident and reflected strain pulses. Finally, specimen strain rate can be simply obtained by taking the derivative of strain function with respect to time -$d\varepsilon/dt$ - .

In this study, a modified SHPB setup was used throughout the high strain rate tests. Instead of obtaining the specimen stress through strain measurements as given in Equation (1), quartz crystals were installed to transmitter and incident bar/specimen interfaces in order to increase the sensitivity of measured forces and to obtain directly the forces rising at the specimen/bar interfaces. A quartz crystal is basically composed of two elements: silicon and oxygen, and they respond any mechanical stress by generating electrical charge due to piezo-electricity phenomenon. Boston Piezo-Optics X-cut quartz crystals with the thickness of 0.254 ± 0.01mm are used in the experiments. Crystals and the bars have the same diameter and very similar mechanical impedance (bar impedance: 14.19x10^6 kg/m^2/sec, quartz crystal: 15.11 x10^6 kg/m^2/sec with a ratio of 1.06) which minimizes the disturbance of the 1D stress wave propagation in the bar component. Quartz crystals are bonded to the transmitter and incident bar ends with

CircuitWorks CW 2400 conductive epoxy. Afterwards, crystals are covered with a 5mm thick aluminum platen in order to preserve the crystals during the tests. Modified SHPB setup is illustrated schematically in Figure 2.16

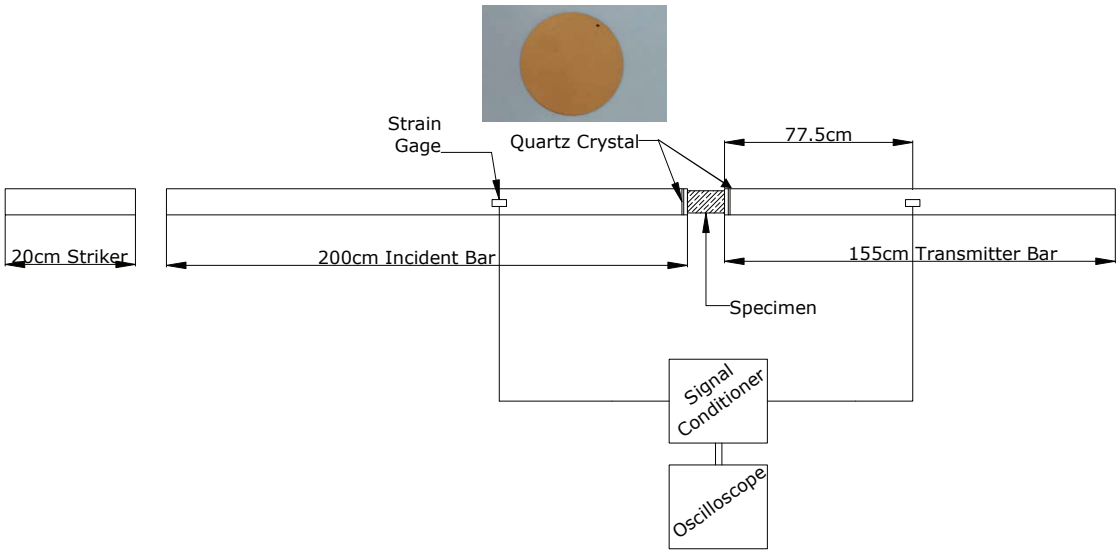

Figure 2.16. Schematical illustration of SHPB setup

The bars are made of 7075 T6 aluminum. Incident, transmitter and striker bars have 40.02 mm common diameter. Mechanical properties of bar components are presented in Table 2.5.

Table 2.5 Material Properties of 7075 T6 Aluminum bars

Elastic Modulus (GPa)	Density (kg/m3)	*Poisson's ratio*
71.7	*2810*	*0.3*

In high strain rate tests, three concrete specimens were tested which had identical geometric dimensions that of static tests with 1.14 L/D ratio. Voltage signal gathered from strain gauges during the SHPB Test 1 is presented in Figure 2.17. In the figure, solid line represents incident and reflected signals obtained from incident bar while dashed line represents the signals gathered from the gauge located on the transmitter bar. After the tests, voltage history was converted to equivalent strain history of bars by Equation (6).

$$\varepsilon(t) = 2V(t)/V_{exc}GF\ K_{gain}\ (1 + \upsilon) \quad (6)$$

In the equation, $V(t), V_{exc}, GF, K_{gain}$ and υ represent obtained voltage signals from strain gauges, excitation voltage, gain factor of strain gauges, conditioner constant and Poisson's ratio of aluminum bars, respectively.

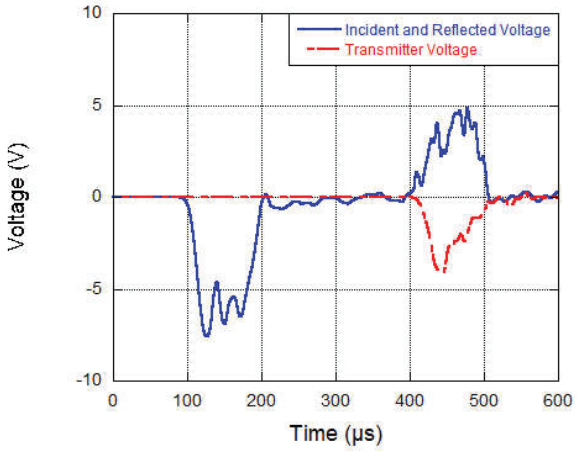

Figure 2.17. Voltage history of SHPB Test 1

As it can be seen from the figure above, the compressive wave in the transmitter bar raised after plenty of time (300 μs) from the first signal recorded at incident bar strain gauge, and stress on the specimen was determined from this wave by using Equation (4). Figure 2.18 illustrates the calculated stress of specimens both from strain gauge and quartz crystal against strain, and the specimens strain rate-strain was presented in Figure 2.19.

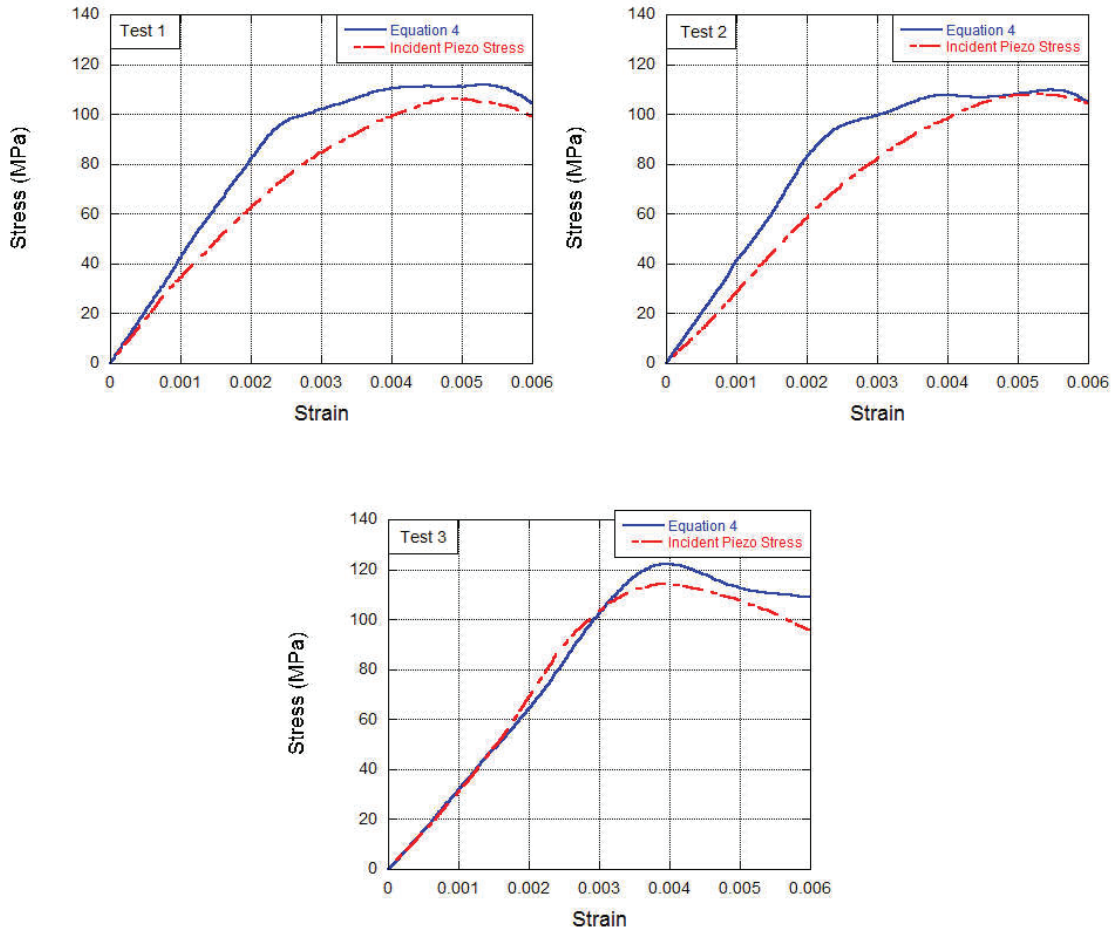

Figure 2.18. Stress-strain relation of SHPB Test 1, 2 and 3

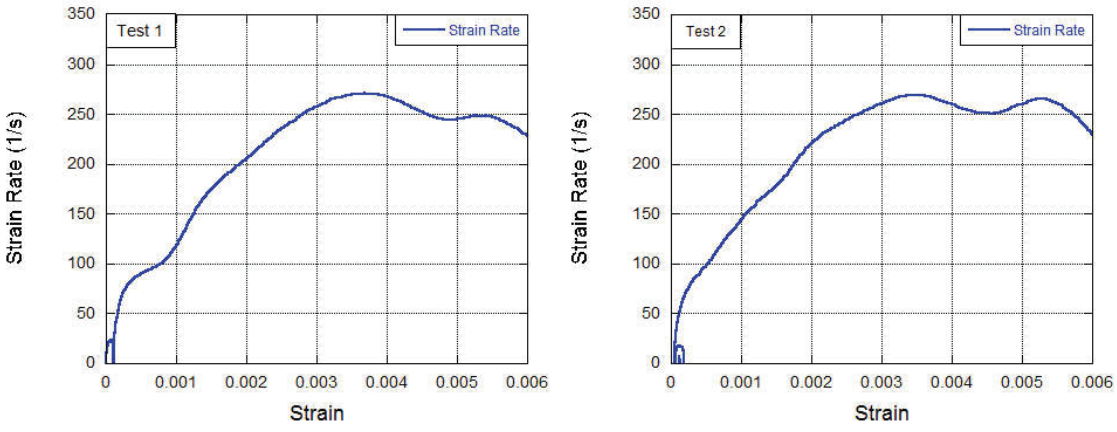

Figure 2.19. Strain rate-strain relation of SHPB Test 1,2 and 3

(cont. on next page)

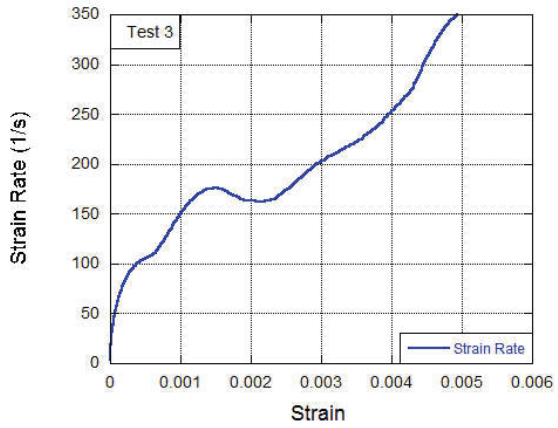

Figure 2.19. (Cont.)

Peak stresses and corresponding strains are given in Table 2.6. In general, peak stresses of the tests did not significantly dispersed from each other.

Table 2.6. Peak stresses and failure strains of the tests

Test	*#1*	*#2*	*#3*
Stress (MPa), Gauge/Quartz Crystal	111/106	109/107	122/114
Failure Strain	0.0053	0.0055	0.0040

Calculated stress-strain relation was compared by the stress-strain curve of piezoelectric quartz crystal to check the accuracy and to validate the work. As can be seen from the Figure 2.18, in Test 1 peak load between two types of data processing differed 3.70%. From the Figure 2.19, it can be observed that the strain rate of the specimens is not constant over the whole testing duration. Therefore, representative strain rates were selected to be the strain rate at failure of specimen which were obtained as 235, 260 and 245 1/s for three of the specimens.

2.3.4 Model Parameters

The study to be performed in order to determine the parameters of the material model was primarily started with determination of the physical properties of the concrete. First, concrete density was calculated using a cylinder specimen by dividing the mass by volume and it was determined as 2183 kg/m^3.

Average compressive strength of concrete was calculated previously as 62 MPa at the lowest cross head speed 0.0045 mm/s (Figure 2.20 (a)). ACI 318-08 standard was followed to calculate the elastic modulus of concrete by the slope of the line drawn from zero to 45% of compressive strength, which yielded to an average elastic modulus of 32 GPa (Figure 2.20-b) for three specimens equipped by strain gauges. The shear modulus (G) was calculated by $E/2(1+\upsilon)$ formulation and resulted with 13.32 GPa.

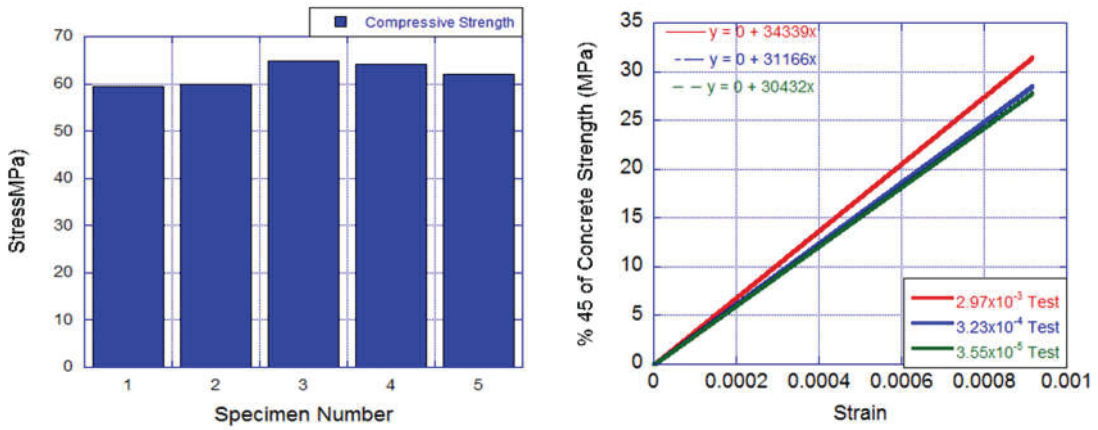

(a) Compressive strength of specimens at 0.0045 mm/s cross head speed

(b) Elastic modulus curves

Figure 2.20. Mechanical properties of test specimens

Strength constants of HJC model were determined next. As the first step, detection of strain rate sensitivity parameter (C) will be explained. To determine strain rate sensitivity parameter static test results of concrete specimens were used. In the HJC material model, the effect of strain rate to the normalized compression strength is defined by $1+C\ln(\dot{\varepsilon}/\dot{\varepsilon}_{ref})$ function. Reference strain rate ($\dot{\varepsilon}_{ref}$) was selected to be the lowest strain rate ($3.55x10^{-5}$) in the function. Figure 2.21 (a) presents compressive strengths obtained from static tests under slow (static) strain rates normalized with respect to average strength obtained at reference strain rate. Figure 2.21 (b) presents the same data but including results obtained from high (dynamic) strain rate tests. Change in strength by various strain rates define the strain rate sensitivity parameter, therefore, a straight line was drawn from least squares fit through the data points and the slope provided the strain rate sensitivity parameter as 0.0205 and 0.0472 for C_{static} and $C_{dynamic}$, respectively. The reason of strength enhancement at high strain rate is not only based on strain rate sensitivity but also increased pressure effects (Holmquist et al,

1993). This is specifically true at higher strain rates in which stress state turns into tri-axial case. To estimate the pure strain rate effect aforementioned pressure effects must be eliminated, therefore, in the analyses C_{static} was selected and used. A preliminary numerical analysis was undertaken with the detected constants to check the validity of the assumption, and given in the next section.

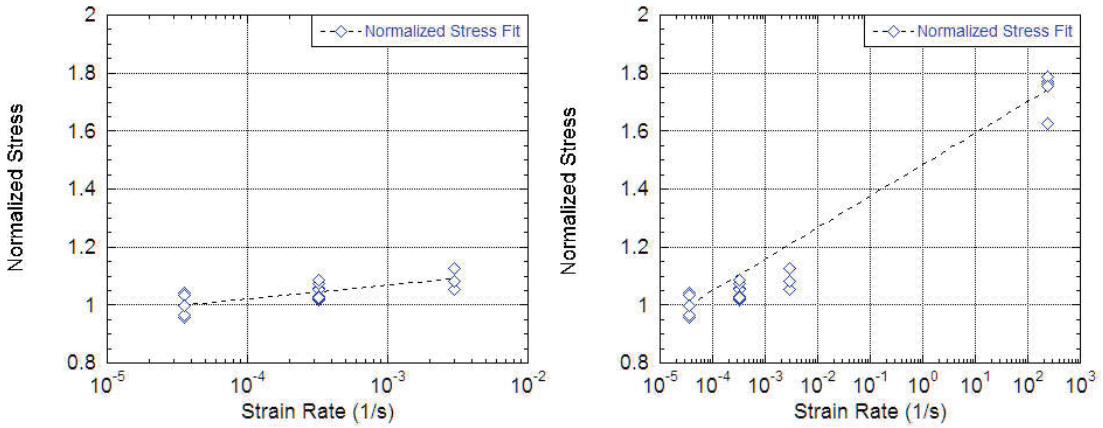

(a) Fit of C_{static} (b) Fit of $C_{dynamic}$

Figure 2.21. Normalized concrete strength change versus strain rate

Strength constant A, which is also known as normalized cohesive strength of concrete at a reference strain rate, is identified as the difference between undamaged (D=0) material strength and completely fractured (D=1) material strength at a known pressure value, and taken from the literature (Holmquist et al, 1993) as 0.79 since confined tests were not conducted in the current study. In order to calculate normalized cohesive strength, the only available confined compression (triaxial) test, which was performed by Ehrgott (1989) and summarized by Hanchak et al (1992), in the literature was used (Figure 2.22) by Holmquist et al. (1993). In the figure, vertical axis represents shear strength (τ) defined by maximum stress difference as $\tau = (\sigma_a) - (\sigma_r)$ where (σ_a) is axial and (σ_r) radial stress and horizontal axis represents hydrostatic pressure as $(\sigma_a + 2\sigma_r)/3$. In the study of Holmquist et al. (1993), it is stated that even though the test data provides a general description of concrete behavior in various pressure ranges, there is not much data available at lower pressures such as P^*<4 in which cohesive strength of concrete material is the most apparent. Due to lack of test data in the interest zone, the cohesive strength is assumed to be 75% of normalized equivalent

stress for quasi static conditions ($\dot{\varepsilon}^* = 0.001$) and normalizing to reference strain rate 1 results in A=0.79.

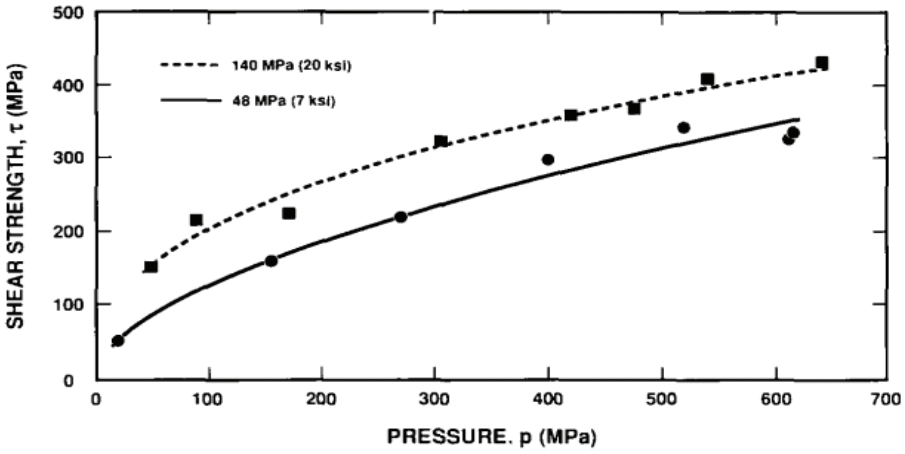

Figure 2.22. Shear strength-pressure relation (Hanchak et al, 1992)

Afterwards, normalized maximum strength (S_{max}) was determined. In Figure 2.22, shear strength-pressure relation of concrete material with 48 and 140 MPa uniaxial compressive strengths are presented and curves are observed to be almost parallel to each other. Therefore, in the current study, S_{max} was determined by interpolation of shear strengths for 62 MPa average strength of concrete. For this purpose first, a point was determined on each curve considering that the zone where there is no stress increase by increasing pressure. Afterwards, using corresponding shear strengths of two detected points and the difference of material strengths at these points (470, 48 and 62 MPa) interpolation could be performed. Finally, the detected specific shear stress for the material was normalized by uniaxial compressive strength and S_{max} calculated to be 5.70.

Constants B and N identify the fractured material strength at normalized strain rate with respect to previously mentioned reference strain rate. Parameters are determined by curve fit to obtain the lower borderline of the normalized equivalent stress versus normalized pressure data (Figure 2.1). Constant N is taken as 0.61 as found from the literature (Holmquist et al, 1993) and B is obtained through numerical analysis trials as 0.90 which was well suited with the transmitter bar stress of the SHPB test result.

Next, constants of volume-pressure interaction model are determined. Elastic bulk modulus ($K_{elastic}$) in the linear elastic region ($P \leq P_{crush}$) was obtained by using elasticity theory with the $K_{elastic} = E/3(1-2\upsilon)$ formulation and calculated as 17.77 MPa. Crushing pressure P_{crush} was calculated by $f_c'/3$ expression given in Holmquist et al. (1993) and found out to be 21 MPa. Thus, crushing volumetric strain μ_{crush} could be determined by $P_{crush}/K_{elastic}$ formulation and found out to be 0.001. Locking volumetric strain μ_{lock} is calculated from $\rho_{grain}/\rho_0 - 1$ expression where ρ_{grain} is the aggregate density and ρ_0 is the initial concrete density. μ_{lock} was determined to be 0.173 using experimentally found ρ_{grain} (2560 kg/m^3) and ρ_0 (2183 kg/m^3). P_{lock} is the locking pressure where all the air voids are extracted from concrete due to compaction and taken from the literature (Holmquist et al, 1993) as 800 MPa since it provided a best fit to the data shown in Figure 2.3. K_1, K_2 and K_3 are the constants at fully compact region which was also taken from literature as 85000, -171000 and 208000 MPa respectively (Holmquist et al, 1993) for granite and quartz (Marsh, 1980).

T^* parameter is the normalized maximum tensile hydrostatic pressure and given by T/f_c' relationship where T is the ultimate principle tensile stress that the material can resist. In order to find tensile strength of concrete, three split tensile tests were performed by specimens having 24 mm length and 39.5 mm diameter (Figure 2.23). For this purpose ASTM C496 (2011) code was followed and average strength was found to be 6.3 MPa.

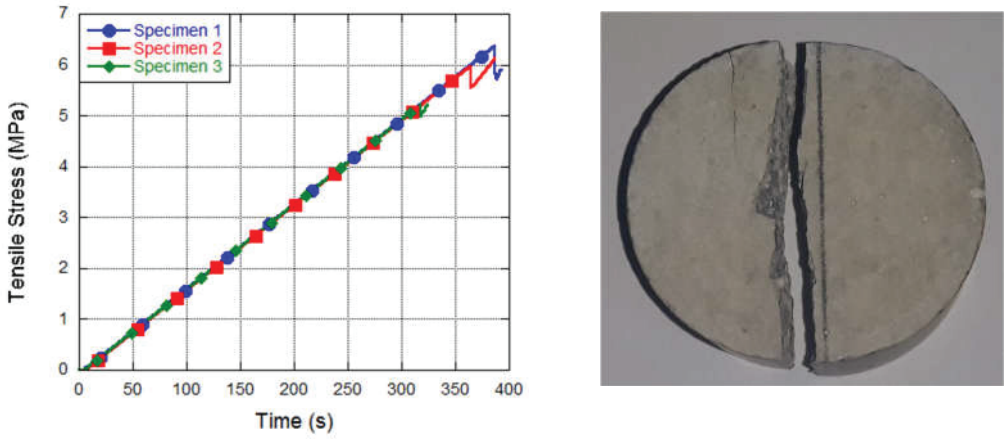

(a) Tensile stress history (b) Crack profile

Figure 2.23. Split tensile tests

D_1 and D_2 are the damage model constants which were taken from literature due to insufficient data(Holmquist et al, 1993). All constants used for material characterization are presented in Table 1.

Table 2.7. Summary of Constants

Strength Constants	***Value***
A	0.7900
B	0.9
N	0.6100
C	0.0205
$f_c^{'}$	0.0620 (GPa)
S_{max}	5.7000
G	13.3200 (GPa)
Damage Constants	***Value***
D_1	0.04
D_2	1
$EF_{min}\,(\varepsilon_p^{\,f})$	0.01
Pressure Constants	***Value***
P_{crush}	0.0210 (GPa)
μ_{crush}	0.001
K1	85 (GPa)
K2	-171 (GPa)
K3	208 (GPa)
P_{lock}	0.80 (GPa)
μ_{lock}	0.173
T	0.0063 (GPa)

2.4 A SHPB Numerical Simulation

Numerical modeling studies were performed by using LS-DYNA (v971, Livermore Software Technology Corporation) software to perform a verification work of obtained parameters. LS-DYNA is capable of performing nonlinear finite element analysis by use of explicit time integration method. SHPB test setup was created to have six main parts (striker, incident, and transmitter bars; two protective aluminum disks

and specimen) in the numerical model using 317,950 eight node hexahedral solid elements with one integration point (Figure 2.24).

In solid elements, stresses and strains are calculated at the integration point. Using one integration point does not yield any strain even though a deformation occurs in the solid element, which results to zero energy modes (hourglass modes). Thus, hourglass control (Flangan-Belytschko type) was utilized to prevent the aforementioned modes.

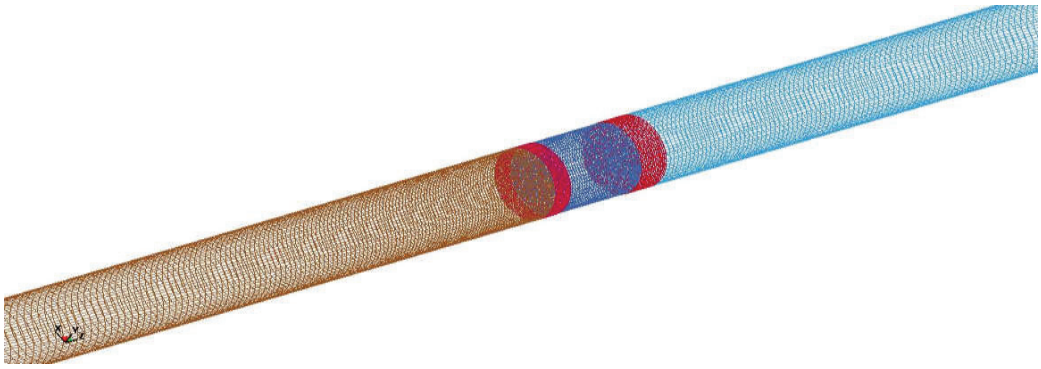

Figure 2.24. Numerical model of SHPB test setup

Surface to Surface and Nodes to Surface contact interfaces were created between the surface of the bars (striker-incident) and specimen-bar surfaces, respectively, to provide more accurate prediction of finite element analysis. Static and dynamic friction coefficients used in the contact definition are 0.3 and 0.2 for bar to bar and 0.1 and 0.05 for bar to specimen surfaces. A parametric study about the effect of bar to specimen surface friction was also performed.

MAT_JOHNSON_HOLMQUIST_CONCRETE material model, (Holmquist et al, 1993), which was explained in detail previously, was assigned to the sample in the numerical model and the initial velocity of striker bar at the experiment was given to the striker bar to collide with the incident bar. A compression wave propagated in the incident bar similar to the experimental program. Required data such as force were gathered from the strain gauge locations on the incident and transmitter bars in the models and detected results are compared to the experimental results.

In the current study, numerical analyses were initiated with a preliminary study to investigate the friction restraint between the specimen and bars. Throughout the tests bar-specimen faces were lubricated properly. Although, the friction effect could not be neglected totally for a brittle material like concrete which has a coarse surface,

practically polishing and lubrication makes frictional effects insignificant and reduces the coefficient to 0.1 or less (Li and Meng, 2003). Figure 2.25 presents transmitter bar stress histories of real test case and numerical analyses with static and dynamic friction coefficients varying from 0.05 to 0.4. From the figure it can be seen that coefficient of friction have an insignificant effect up to peak stress, and only a minor effect at post-peak for a specimen with L/D ratio of 1.14. A similar conclusion was also drawn by Hao et al. (2013) for specimens having L/D ratio greater than or equal to one when friction coefficients vary from 0.3 to 0.5. As a result, selection of dynamic and static friction coefficients were made with considering the existence of proper lubrication. Thus, static friction coefficient was selected to be 0.1 and since moving a still object requires a higher force than that of an object in motion, dynamic coefficient of friction was taken to be half of static (0.05).

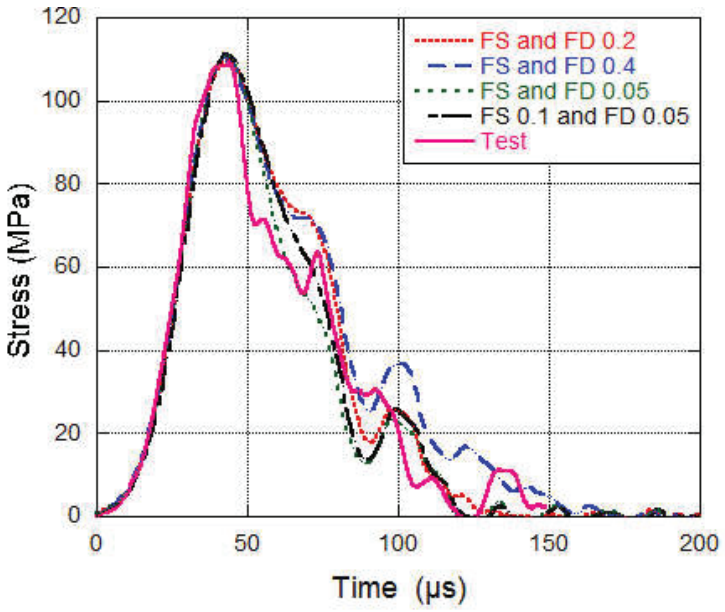

Figure 2.25. Transmitter bar stress history with various friction coefficients

Although a clear strength increase is reported by the majority of researchers for concrete under high strain rate conditions, there is a debate about the reason of this behavior. In the literature, some various approaches are offered as: influence of inertia at (1) micro crack and (2) structural levels and (3) viscous behavior of bulk material due to water content.

Concrete is a porous material with micro cracks inherently. Its behavior during the static uniaxial loading is affected by propagation of micro cracks internally which are due tensile stresses and primarily orientated in the axial direction. In a rapid loading case, time required for micro crack development or propagation is significantly reduced due to inertial effects. Therefore, strain rate dependent behavior of micro cracking can influence the response when concrete is subjected to high strain rates during an impact or blast loading. Additionally, structural inertial forces are as the source of another type of inertia. Material turns into a discontinuous structure with severe internal cracking that result in dilatation when loaded to failure. The static strength might be quickly exceeded since the specimen does not have enough time to unload in the lateral direction and hence producing an effective confining stress on the central core of the specimen. This event can be explained by also transition from a uniaxial stress state to a uniaxial strain state. (Bischoff and Perry, 1991; Ozbolt and Sharma, 2012). Finally, existence of viscous behavior of bulk material (viscosity owing to water content) results in a strain rate dependent behavior (Ozbolt and Sharma, 2012). In the current study strain rate sensitivity and inertial effects were tried to be observed by analyzing the effect of C parameter. For this purpose, stress developing on the specimen was determined using three different C values in the material model: C is equal to zero, C_{static} and $C_{dynamic}$. Results are presented with quasi-static test results in Figure 2.26.

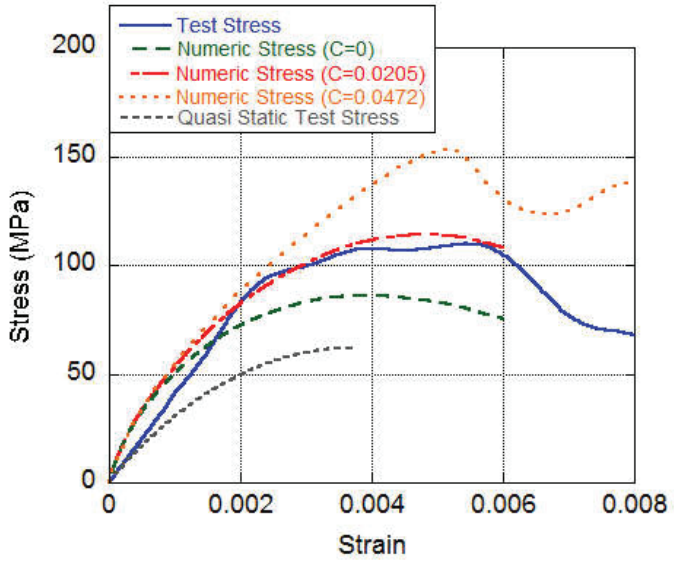

Figure 2.26. Effect of strain rate sensitivity parameter

Note that C taken as zero can be interpreted as numerical model neglects the strain rate sensitivity of concrete. As seen in Figure 2.26, analysis done with C=0 results higher stresses compared to quasi-static stresses. This increase in stress can be attributed to the stress increase in concrete due to confinement effects resulting from lateral inertia, since no other strain rate sensitive parameter is involved in the model. Difference between the stress-strain curve obtained from an analysis with C=0 and quasi-static test result is illustrated in Figure 2.27 as inertia effect.

However, as seen in Figure 2.26, analysis with C=0 gives lower stresses compared to test results, which shows that lateral confinement is not the only factor that causes a stress increase. The difference between the test result and the analysis result with C=0 can be attributes to the strain rate sensitivity of concrete, which is given in Figure 2.27 as strain rate sensitivity effect. Thus, total increase in stress at a given strain at high strain rates can be taken as the sum of radial inertia effects and strain rate dependent material behavior effects, which is also shown in Figure 2.27.

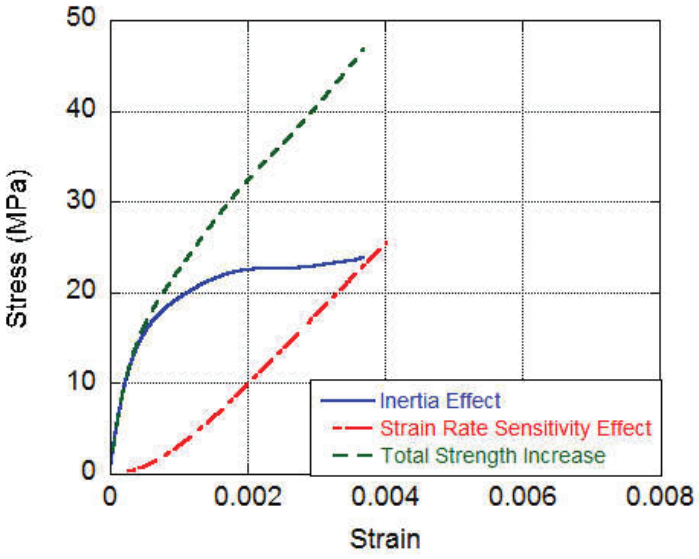

Figure 2.27. Effect of inertia and strain rate sensitivity

Relative contribution of lateral inertia confinement and strain rate sensitivity of material to the stress increase is presented in Figure 2.28. It is clear from the figure that at the onset of loading lateral inertia is highly responsible from the observed stress increase while strain rate sensitivity of the material has lower effect. However, lateral

inertia confinement drops as the specimen is strained further, while material strain rate sensitivity becomes more effective.

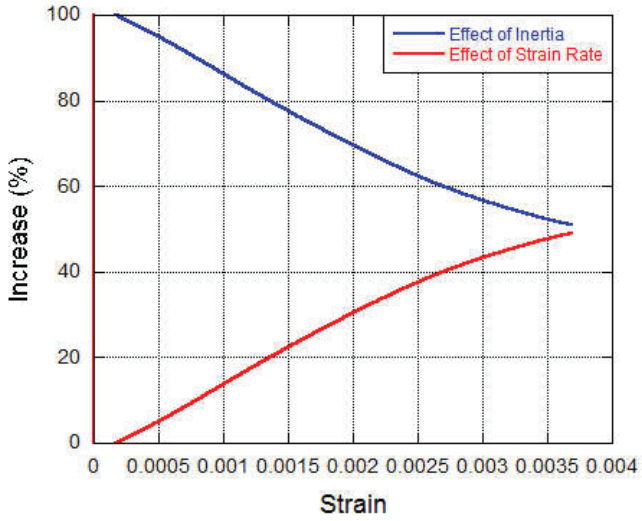

Figure 2.28. Inertial and strain rate effects

In Figure 2.26, it is seen that analysis with $C=C_{dynamic}$ overestimated the stresses significantly, since this parameter was found from high strain rate test results which includes stress increase due to both confinement resulting from radial inertia and strain rate sensitive behavior of concrete. In other words, using $C=C_{dynamic}$ takes confinement effects into account twice, resulting an over estimates stress-strain response. Using $C=C_{static}$ gave best match with test results, since this parameter was derived from quasi-static tests, in which lateral inertia effects was insignificant. Thus, analyses with $C=C_{static}$ reflects true strain rate sensitive behavior of concrete and all following analyses were conducted using this value.

Experimental numerical results are presented in Figure 2.29 to validate the simulation and to verify the determined material model parameters. As it can be seen from the figure, stress-strain curves of Test and Simulation 1 overlaps with each other after 0.002 strain. The curves obtained from Test were detected by use of signals gathered from strain gauges in Equation 4, and it is observed that the curves obtained from incident piezoelectric quartz crystal exhibits a variation from the test and simulation in all strain ranges. Peak stress found in numerical analysis was calculated to be 7.5% higher than that of measured by quartz crystal.

In Test and Simulation 2, a discrepancy between stress-strain curves continues up to 0.002 strain, after which they converge to each other. Stress-strain curve obtained from incident piezoelectric quartz crystal slightly differs from the test and numerical analysis except in a strain range that is higher than 0.0055.

Stress-strain curve obtained from Test 3 and its incident piezoelectric quartz crystal exhibit a good agreement with each other until a strain of 0.0015, after which they start to diverge. There is a discrepancy between Analysis 3 results and test results.

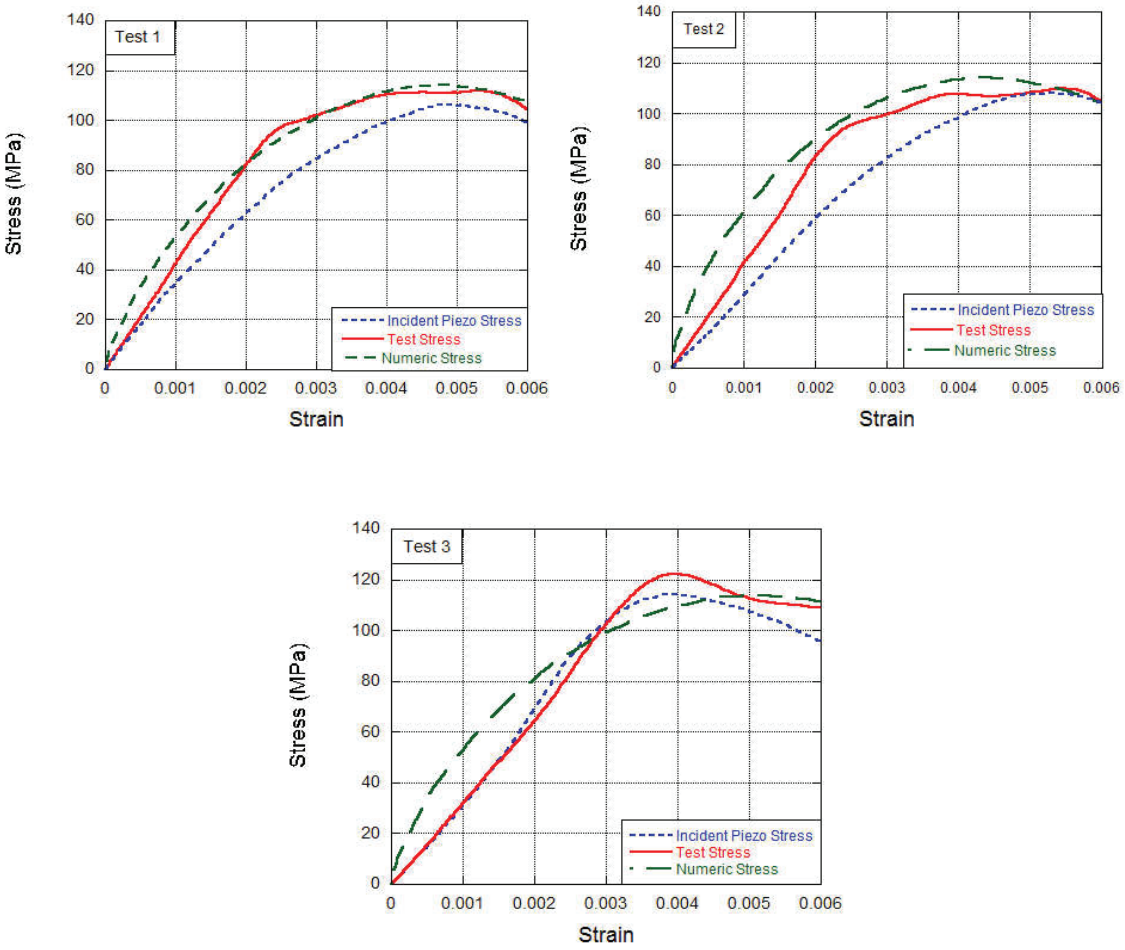

Figure 2.29. Stress-strain comparison of experimental work and corresponding numerical analysis

As previously mentioned, in classical SHPB setup stress waves are recorded from strain gauges located at certain points on the transmitter and incident bars. Relatively larger diameter bars were used in concrete these tests, which causes dispersion in the propagating stress/force waves occurring at the specimen/bar interfaces affecting the measurements obtained from strain gauges. Piezoelectric quartz

crystals inserted at the sample-bar interface led the recording of stresses with minimum amount of dispersion. Therefore, quartz crystals increased the sensitivity of measured forces. Proximity of obtained stresses from strain gauges to piezo stresses proved the validity of classical data gathering method as well.

CHAPTER 3

DROP TOWER TESTS

3.1 Introduction

Drop tower tests of six prismatic concrete specimens had been performed to form a basis for the numerical analyses that were developed to check the accuracy of detected material model parameters under various loading implementations, specimen geometry and boundary conditions. Discussion starts with test setup, specimen dimensions and continues by presentation of obtained force, energy and velocity histories of each test. Afterwards, a boundary condition based comparison of test histories are performed and presented with a discussion. Chapter is closed by damage evaluation of specimens.

3.2 Drop Tower Test Setup

Concrete specimens, which were taken from previously poured concrete batch, used in these tests were cast into steel molds as shown in Figure 3.1 (a), obtaining prisms of 200 mm x 200 mm x 20 mm in dimension (Figure 3.1-b).

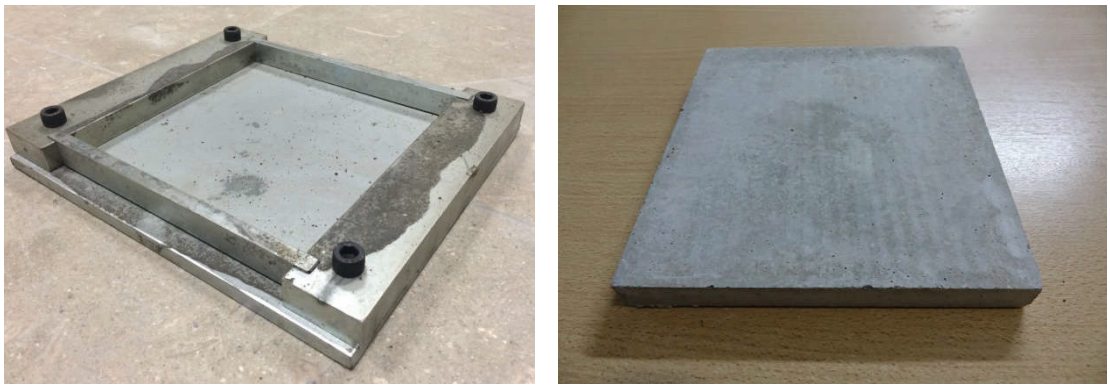

(a) Prismatic steel mold (b) Concrete specimen

Figure 3.1. Drop tower test specimen

A protective box, which is designed to prevent possible damage to the high speed camera and test equipment, is designed and manufactured (Figure 3.2-a). To investigate the behavior of concrete specimens under different boundary conditions, specimen holder that is located inside the protective box was drilled to have a hole with 100 mm diameter (Figure 3.2- b). Three different plugs were produced to obtain 80 mm and 60 mm diameter holes and an unperforated flat surface. Drop tower tests were performed at different loading velocities and boundary conditions by using CEAST Fractovis Plus drop tower testing device (Figure 3.3).

(a) Protective box (b) Specimen holder with plugs

Figure 3.2. Drop tower test setup

Figure 3.3. Drop tower testing device

Testing device can perform tests up to 20 m/s impact velocities through the springs located in high speed module. A striker equipped with strain gauges capturing the impact load up to 90 kN is used. The striker had a hemispherical insert at the tip with a 10 mm radius (Figure 3.4), and to obtain the desired load on the specimen, it had additional masses totaling 15.68 kg. Tests were conducted by the following procedure: Inserting the appropriate plug to the specimen holder which resulted in desired hole diameter as boundary condition, fitting the specimen on top of the holder without any restrictions, and adjusting it to receive the strike at the center point.

Figure 3.4. Hemispherical insert

3.3 Test Results and Discussion

The drop tower tests were started with Test 1 which had unperforated flat surface boundary condition and target impact velocity of 1 m/s. Variation of impact force with time is presented in Figure 3.5. As can be seen from the graph, impact force increases nearly linearly in the time interval of 0-2 milliseconds and starts to decrease after reaching the peak force of 9 kN. The test was completed in around 4 milliseconds. The dissipated energy variation with time, which was calculated by the area under force-tip displacement curve, is given in Figure 3.6. Dissipated energy in 0-2 milliseconds reached to 7.6 Joule with a rapid rising curve depending on the tip displacement, and the maximum energy dissipated was 8.9 Joule. Figure 3.7 shows the velocity versus time. Here, the actual velocity of the striker tip at the moment of impact is determined to be 1.05 m/s, afterwards the velocity decreased throughout the test and test ended with a negative velocity due to rebound of striker tip.

In Test 2, target impact velocity was selected to be 3 m/s and the boundary condition was identical to the first test (unperforated flat surface). Variation of impact force with time is presented in Figure 3.5. From the figure, it can be seen that the force increases nearly linearly similar to the first test up to a maximum value of 19.5 kN at 0.4 millisecond and afterwards starts to decrease by time. The test lasted shorter than the previous test and ended in 2 milliseconds. The dissipated energy variation with time is presented in Figure 3.6. The dissipated energy between 0 to 0.4 milliseconds reached to 12.3 Joule, and when the test ended at 2 milliseconds, total dissipated energy reached to 36 Joules. Figure 3.7 shows the velocity versus time. Here, the actual velocity of the striker tip at the moment of impact is determined to be 3.17 m / s and decreased rapidly by time. However, velocity at the end of the test decreased down to vicinity of 2.4 m/s and striker kept moving downwards after penetrating through concrete plate.

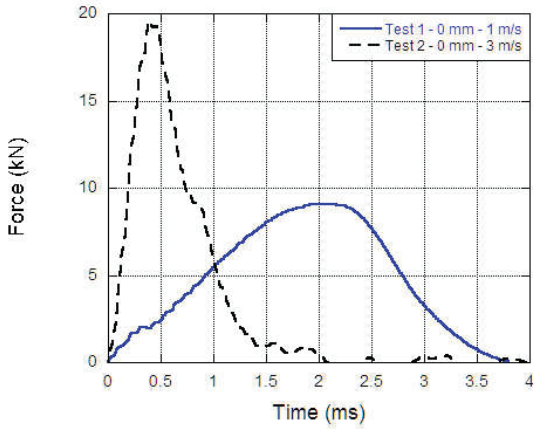

Figure 3.5. Force history of Test 1 and Test 2

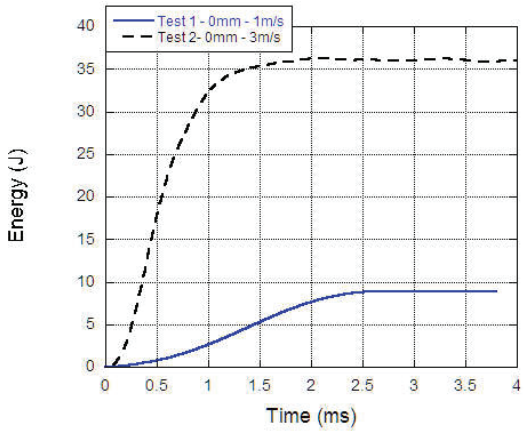

Figure 3.6. Energy history of Test 1 and Test 2

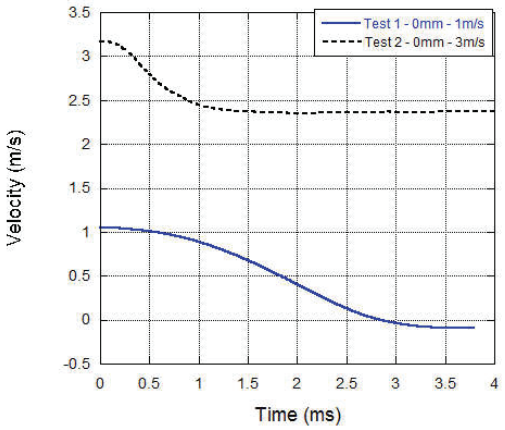

Figure 3.7. Velocity history of Test 1 and Test 2

In Test 3, boundary condition at the specimen holder was changed to a hole at the bottom surface with a 60 mm diameter. Similar to the previous test set, the impact velocity of the striker tip was arranged to be 1 m/s. As can be seen from the Figure 3.8, the maximum force was determined to be 11 kN, which was reached approximately in 1 millisecond. In Figure 3.9, energy versus time graph is presented and 5.80 Joule energy dissipated at the moment when the force reached to its maximum value. Throughout the test, 8.60 Joule energy is dissipated in total. In Figure 3.10, velocity history is presented. Actual velocity of the striker tip at the impact moment is determined to be 1.07 m/s which decreased afterwards.

In Test 4, the boundary condition was identical to previous test (a hole at the bottom surface with 60 mm diameter). However, impact velocity was targeted at 3 m/s in this test. An increase in force and energy was observed as expected with increased striker velocity. In Figure 3.8, variation of impact force with time is presented. The maximum force was obtained as 15.80 kN after 0.3 milliseconds of first contact between striker and concrete specimen. Dissipated energy corresponding to the moment of maximum force was determined to be 8.40 Joule from the dissipated energy- time curve (Figure 3.9). Total dissipated energy was obtained as 26.15 Joule at the end of the test. Actual velocity of the striker tip at the moment of impact is determined to be 3.17 m/s and decreased rapidly by time (Figure 3.10). However, velocity at the end of the test decreased down to vicinity of 2.5 m/s and striker kept moving downwards after penetrating through concrete plate.

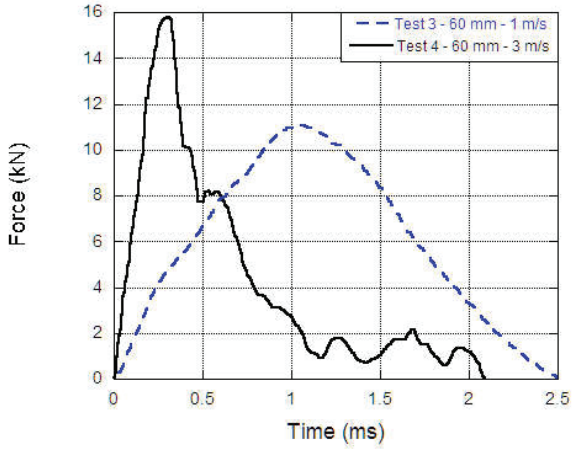

Figure 3.8. Force history of Test 3 and Test 4

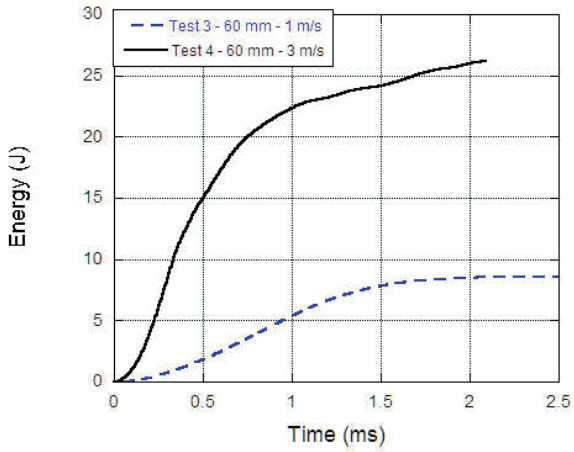

Figure 3.9. Energy history of Test 3 and Test 4

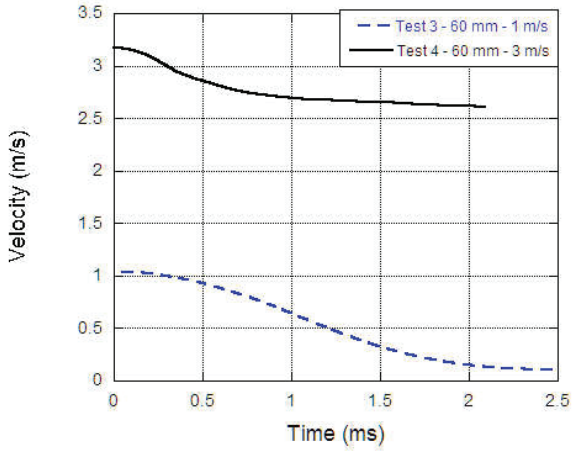

Figure 3.10. Velocity history of Test 3 and Test 4

In Test 5, a third and final boundary condition was applied at the bottom surface with a hole of 100 mm diameter. Impact velocity of the striker tip was arranged to be 1 m/s for initial test. The force-time graph of fifth test is presented in Figure 3.11. Maximum force reached to 5.7 kN (in 0.8 milliseconds) in the test. Dissipated energy-time graph is shown in Figure 3.12 and the dissipated energy at the moment that the maximum force was reached observed to be 2.3 Joule. A total of 5.40 Joule energy was dissipated throughout the test. In addition, the actual velocity of the striker tip at the moment of impact can be determined to be 1.05 m/s, Figure 3.13. However, velocity at the end of the test decreased down to vicinity of 0.67 m/s and striker kept moving downwards after penetrating through concrete plate.

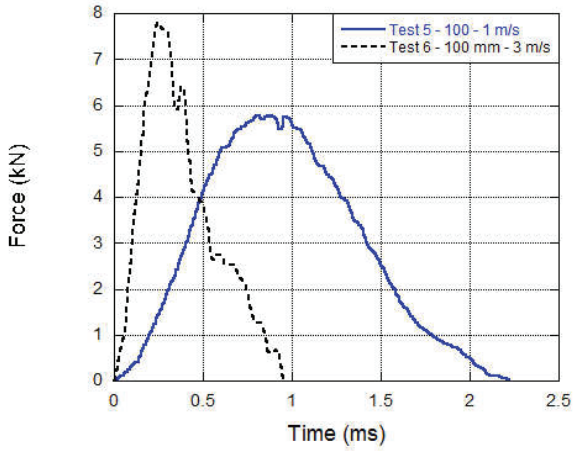

Figure 3.11. Force history of Test 5 and Test 6

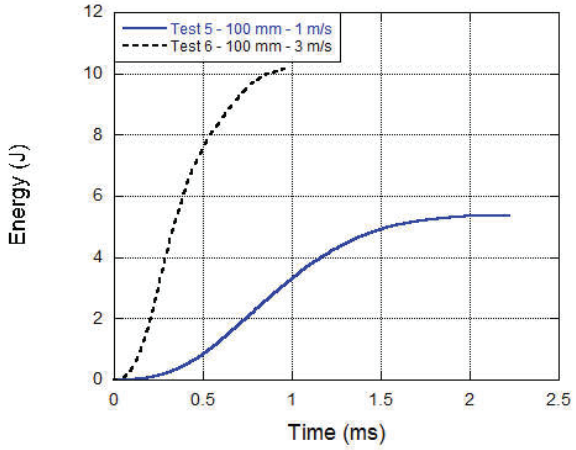

Figure 3.12. Energy history of Test 5 and Test 6

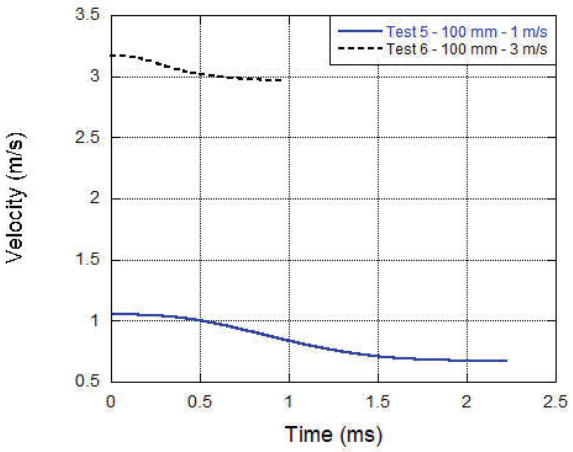

Figure 3.13. Velocity history of Test 5 and Test 6

Test 6 was carried out at a striker velocity of 3 m/s and bottom surface with 100 mm hole of diameter similar to the previous test. The maximum value of force was determined to be 7.8 kN during the test and accessed in 0.25 milliseconds, Figure 3.11. The energy dissipated at maximum force value is measured as 3 Joule, Figure 3.12. Maximum energy dissipation throughout the test is 10.1 Joule. It is seen from the Figure 3.13 that the actual velocity of the striker is 3.17 m/s at the moment of impact. However, velocity at the end of the test decreased down to vicinity of 2.97 m/s and striker kept moving downwards after penetrating through concrete plate.

Figure 3.14 (a,b and c) compares the tests of 3 m/s impact velocity with three different boundary conditions. Comparison is based on force, displacement, energy and velocity histories. From Figure 3.14-a it can be observed that as the diameter of surface hole increases, the highest force reached in the tests decrease. For example, Test 2 exhibit 1.23 times higher peak force than Test 4 and 2.5 times higher than that of Test 6. In this set of tests, striker broke through the specimens and kept on moving downwards. Therefore, tip displacement increased linearly by time. Similar trend of force-hole relation is also observed over energy history of tests such that Test 2 consumed 1.37 and 3.56 times higher energy throughout Test 4 and 6, respectively. Finally, the time-dependent decrease in velocity was changed inversely proportional to the hole diameter. A summary of drop tower test results are presented in Table 3.1.

Figure 3.15 (a,b and c) presents the comparison of the force, displacement, energy and velocity history of the tests with three different boundary conditions for the impact velocity of 1 m/s test. When the force histories of tests are investigated, peak

force of Test 1 (with unperforated flat surface boundary condition) is below the highest force reached in Test 3 (with a 60 mm hole at the surface). The lowest peak force is obtained with the third boundary condition of surface as expected. Main reason of this phenomenon is that the rigidity of specimens increases with unperforated surface. Tip displacements in this set of tests exhibit a nonlinear behavior due to rebound of striker. For example, in Test 1 tip displacement starts to decrease after 3 ms. The highest energy level is observed in the first test and the lowest energy level in the fifth test. When the velocity history is investigated, it was found that, except for the first test, the time-dependent decrease in velocity was changed inversely proportional to the hole diameter.

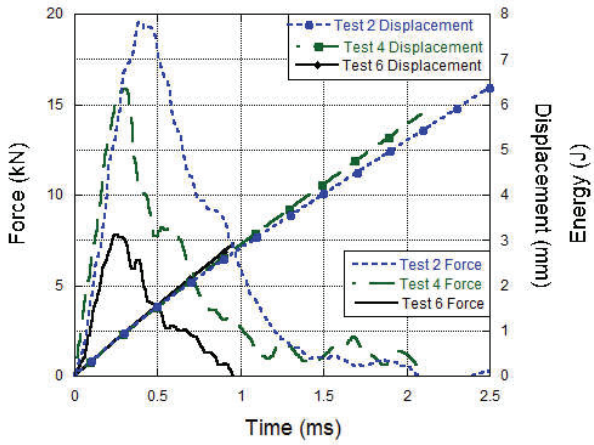

(a) Force history

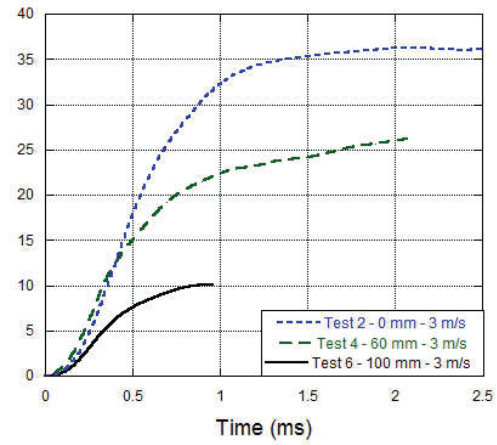

(b) Energy history

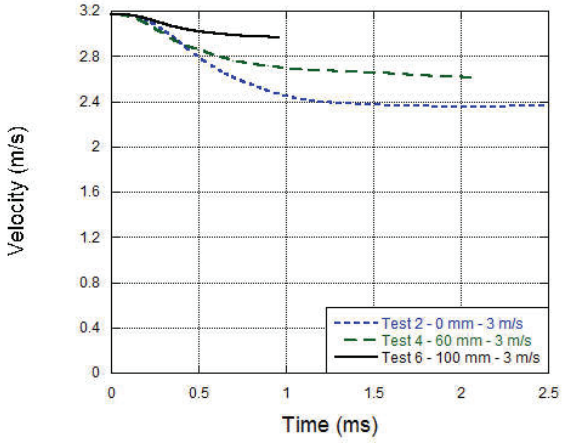

(c) Velocity history

Figure 3.14. 3 m/s impact effect on force, energy and velocity

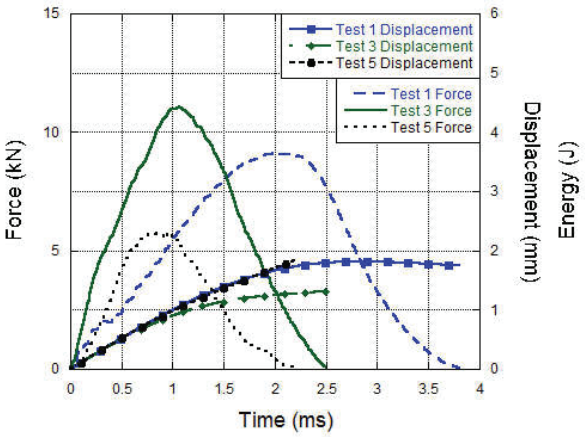

(a) Force history

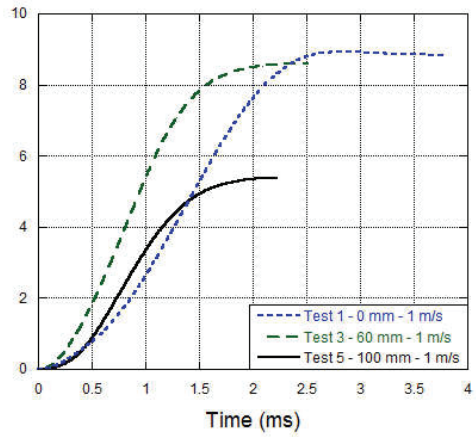

(b) Energy history

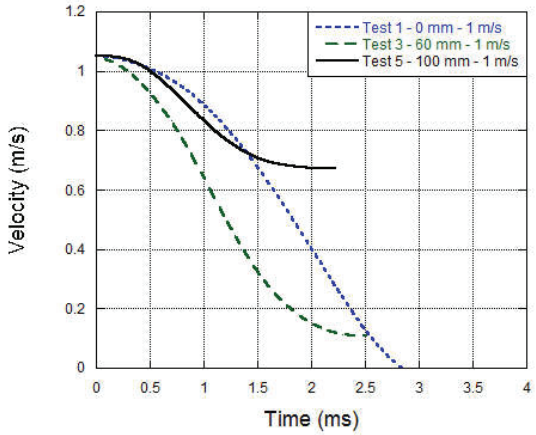

(c) Velocity history

Figure 3.15. 1 m/s impact effect on force, energy and velocity

Table 3.1. Summary of drop tower test results

	Surface Hole (mm)	*Striker Velocity (m/s)*	*Peak Force (kN)*	*Total Energy (J)*
Test 1	0	1.05	9	8.90
Test 2	0	3.17	19.50	36
Test 3	60	1.07	11	8.60
Test 4	60	3.17	15.80	26.15
Test 5	100	1.05	5.70	5.40
Test 6	100	3.17	7.80	10.1

CHAPTER 4

NUMERICAL MODELING OF DROP TOWER TESTS

4.1 Introduction

Simulations of drop tower tests were performed by LS-DYNA (v971, Livermore Software Technology Corporation) software. Force and damage histories of the tests and numerical analysis are compared to check the accuracy of mechanical characterization and behavior of material under lower strain rates compared to SHPB.

4.2 Numerical Simulation Description of Drop Tower Tests

Drop test model basically consisted of three parts: striker tip, specimen and the holder. A full-scale model was created for all three components and discretized in space by using a total of 415,328 eight node hexahedron solid elements (Figure 4.1). Prismatic elements used to model concrete specimens were cube in shape with a side length of 1.25 mm. Support of specimen holder was not modeled explicitly. Instead, rotational and translational restraints were assigned to X, Y and Z directions for the nodes that are located on the bottom face of specimen holder since the support component of holder was sufficiently rigid. Striker was represented by tip only and therefore a total mass of 15.68 kg assigned to the striker part. Mass was distributed to each element of striker tip proportional to their volumes. Eroding Single Surface type contact algorithm was selected and defined for the three parts that are in contact with each other. Static and dynamic coefficient of friction was taken to be 0.3 and 0.2, respectively. This type of contact enables the surface to be updated as the elements on free surface are deleted due to material failure. Force Transducer Penalty type contact algorithm, which has no effect to the solution except recording the contact forces created by previously introduced contact algorithm, was also defined and assigned to striker part. Holmquist-Johnson-Cook material model was selected for concrete specimen similar to the SHPB simulations and previously found parameters were used in the model. Elastic and rigid material models were defined for striker and specimen holder, respectively, and 192000

MPa elastic modulus, 7820 kg/m^3 density and 0.30 Poisson's ratio where assigned for both. Loading is introduced in the model by assigning the impact velocity of the striker as initial velocity with a time step of 50 microseconds. Termination time span of each numerical analysis was selected to be identical to that of testing time.

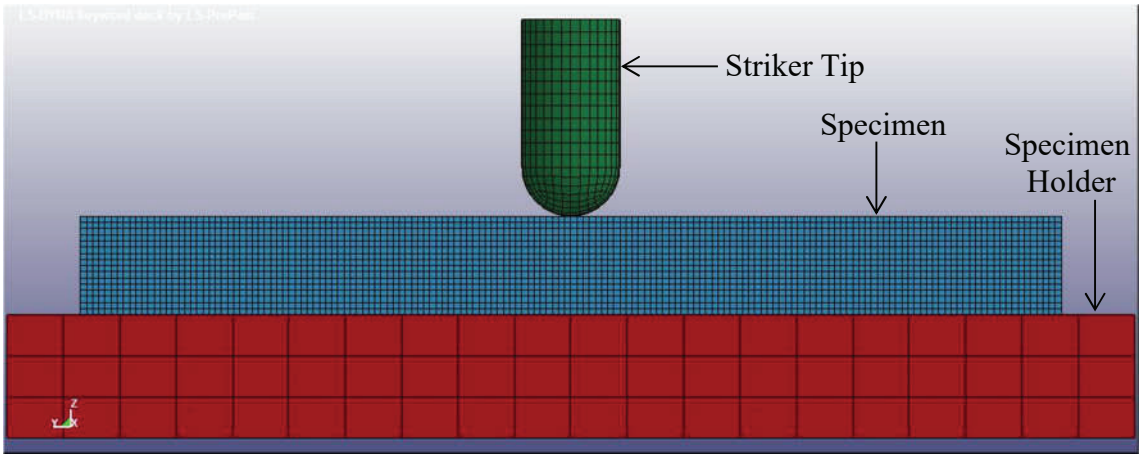

Figure 4.1. Numerical model of Drop Tower test setup

4.3 Comparison of Experimental and Numerical Results

The force- time, displacement-time and energy-time curves obtained from the numerical analyses and the tests are compared in Figure 4.2 and Figure 4.3 for Test 1 and 2, respectively. Peak forces were obtained as 9 kN and 9.15 kN for Test and Analysis 1 at about 2 ms. Test ended by force reaching to zero at 3.80 ms while the force measured to be 1.40 kN in this time interval for the analysis case. Increase and decrease trends of forces obtained from the Test and Analysis 1 displayed similar behavior to each other. On the other hand, both displacements exhibit nonlinear behavior. However, rebound of striker was observed in the test unlike the numerical analysis. If the dissipated energies are investigated, both curves had an almost parallel path until 2 ms, which is the time peak force was reached, from the beginning (Figure 4.3). At this moment of time 22% higher energy was dissipated by test, and afterwards, the separation between the curves decreased till the end of testing duration.

In Test 2, impact speed increased by three times and boundary conditions kept identical with previous test. The peak force reached in the test and numerical analysis was found out as 19.6 and 18.3 kN, which corresponds to 7% difference, with 0.15 ms

time lag (Figure 4.2). Test ended by force reaching to zero at 2 ms while the force measured to be 2.5 kN in this time interval for the analysis. Increase trend of forces fitted well with each other for both of the cases. However, separation of post peak behavior became more pronounced in the time range of 1 ms to 2 ms. Additionally, displacements of both cases increased almost linear by time in overlapping form. If the dissipated energies are investigated, both curves had a parallel path till the region where forces first time started to separate each other (0.8 ms). At this point, Test 2 dissipated 25% higher energy than that of Analysis 2.

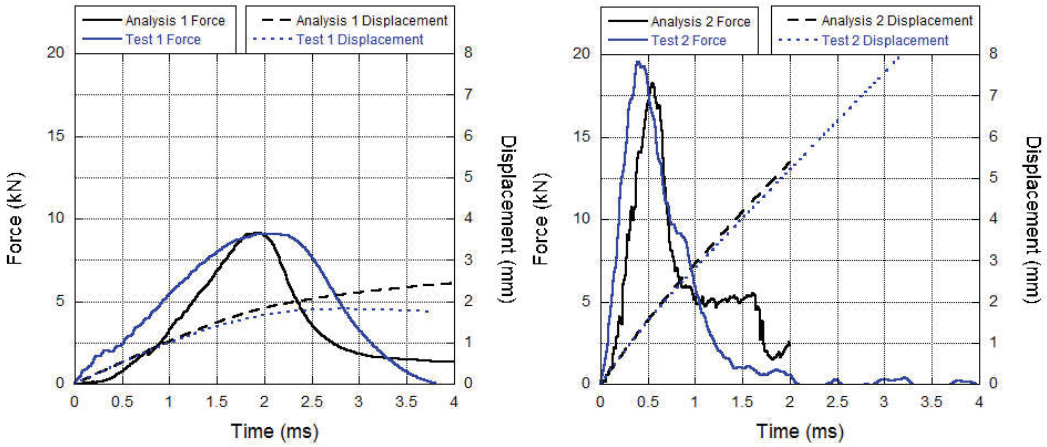

Figure 4.2. Experimental and numerical force history comparison of Test 1 and 2

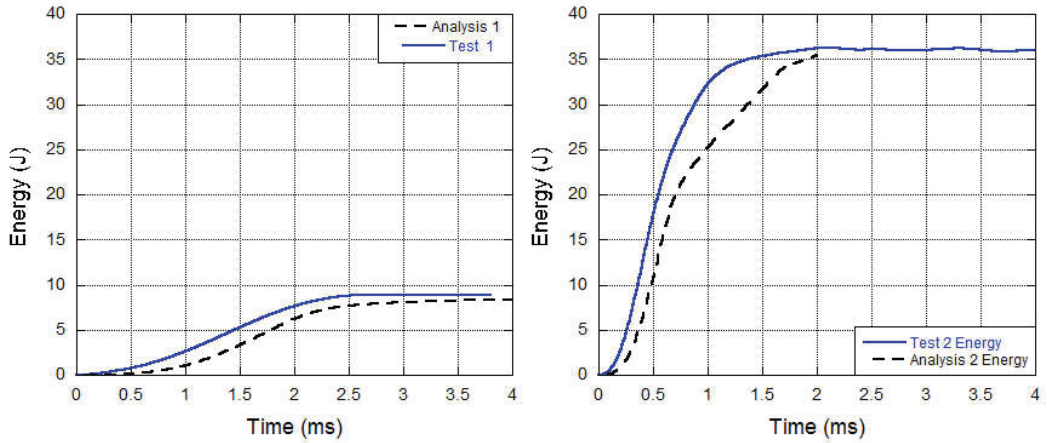

Figure 4.3. Experimental and numerical energy history comparison of Test 1 and 2

Next, boundary condition at specimen holder was changed to a hole at the bottom surface with 60 mm diameter in the following two tests. The force- time, displacement-time and energy-time curves obtained from the numerical analyses and the tests are presented comparatively in

Figure 4.4 and Figure 4.5 for Test 3 and 4, respectively. Test 3, which had an impact speed of 1m/s, reached to 11 kN maximum force while in the numerical analysis it is observed to be 10 kN in 1 ms. Test ended by force reaching to zero at 2.5 ms while the force measured to be 2 kN in this time interval for the analysis case. Sharp increase trend of forces, which is obtained from the Test and Analysis 3, performed similar behavior with each other. However, numerical analysis exhibited a fluctuating trend at post peak region. On the other hand, displacement of both cases exhibited nonlinear behavior, specifically after 0.5 ms. When the dissipated energies are investigated, both curves followed a parallel path which is in close proximity with each other until 2 ms (Figure 4.5). At this point, Test 3 dissipated 17% higher energy than that of Analysis 3 and the gap between the curves nearly closed at the end of testing time span.

Test and Analysis 4 investigation followed. In the test, impact speed increased by three times and boundary condition kept identical with previous test. The peak force reached in the test and numerical analysis was detected as 15.70 and 15.10 kN, respectively, which is a good approximation for concrete. Peak forces were reached at 0.3 and 0.4 ms in the test and in the analysis, respectively, with a 0.1 ms time lag (Figure 4.4). Test ended by force reaching to zero at 2 ms while the force measured to be zero in this time interval for the analysis case as well. Increase and decrease trends of forces obtained from the Test and Analysis 4 performed similar behavior with each other. On the other hand, displacements of both cases increased almost linear by time in overlapping form. Similar to the previous tests and analyses, energy curves performed a parallel path with a certain amount of energy difference between the curves (20%) until 0.8 ms (Figure 4.5). After this moment of time, separation in energy started to increase, and ended by Test 4 having 36% higher energy dissipation than that of Analysis 4.

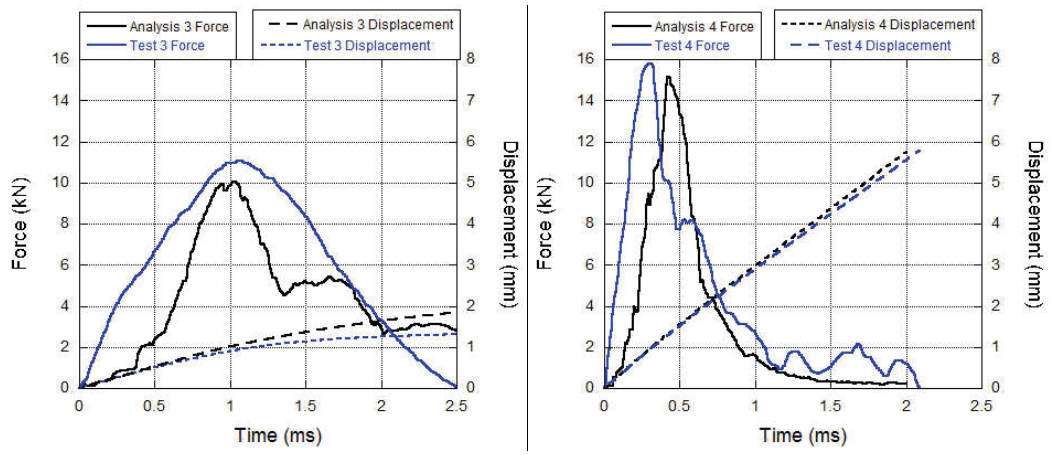

Figure 4.4. Experimental and numerical force history comparison of Test 3 and 4

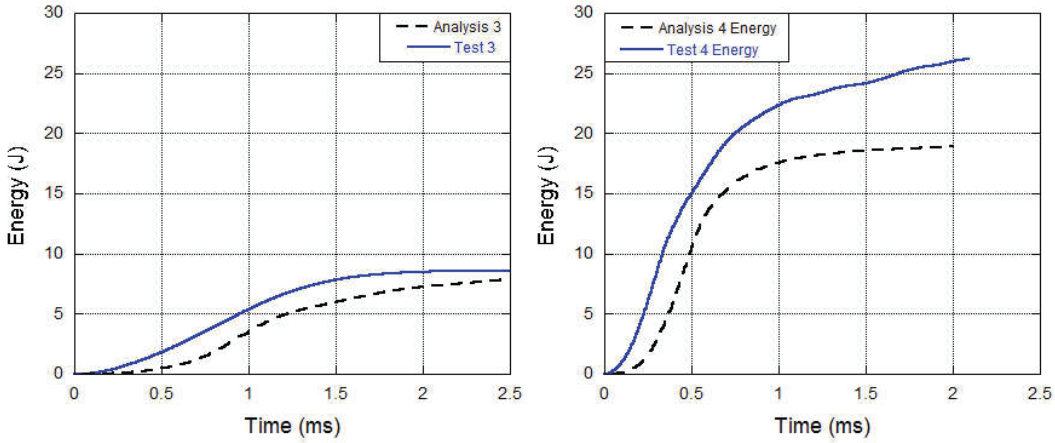

Figure 4.5. Experimental and numerical energy history comparison of Test 3 and 4

The boundary condition at the specimen holder was changed to a hole at the bottom surface with 100 mm diameter in the following final two tests. Force- time, displacement-time and energy-time curves obtained from the numerical analyses and the tests are presented comparatively in Figure 4.6 and Figure 4.7 for Test 5 and 6, respectively. Test 5, which had an impact speed of 1 m/s, reached to 5.80 kN maximum force while in the numerical analysis maximum force was found to be 5.2 kN. Time to reach peak was 0.85 ms in test and 0.93 ms in the analysis. Test and analysis ended by force reaching to zero at 2.2 and 2.5 ms, respectively. Sharp increase trend of forces obtained from Test and Analysis 4 performed a good fit. Similar to previous tests and analyses, energy curves performed a parallel path with a certain amount of energy difference between the curves (approximately 18%) till 1.5 ms (Figure 4.7) which is the

starting moment of force history post-peak curve separation. After this moment of time, separation in energy started to decrease.

Test 6 and simulation investigation followed. In the test, impact speed increased by three times and boundary condition kept identical with previous test. The peak force reached in the test and numerical analysis was 8.15 kN and 7.80 kN, respectively, which is a good approximation for concrete material. Time to reach peak force was 0.27 ms and 0.25 ms for the test and analysis, respectively (Figure 4.6). Test and numerical analysis ended by force reaching to zero at 1 ms. Specifically, increasing trends of forces until the peak load fits quite well with each other, and at 0.40 ms of post-peak region, separation between the curves became clearer. On the other hand, displacements of both cases increased almost linear by time in overlapping form. In Test and Analysis 6, energy histories overlapped with each other until 0.4 ms due to close approximation of force and displacement histories (Figure 4.7). After this moment of time, separation in energy started owing to the separation of force history, and ended by Test 6 having 31% higher energy dissipation than that of Analysis 6.

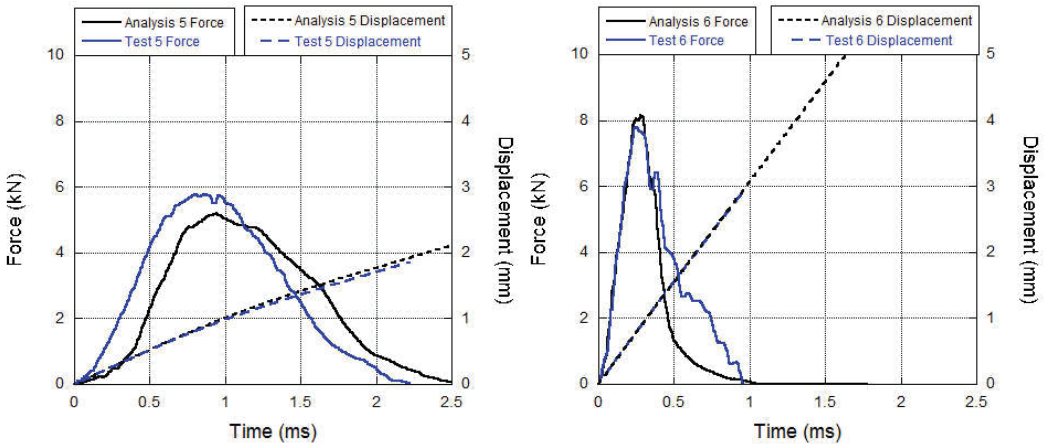

Figure 4.6. Experimental and numerical force history comparison of Test 5 and 6

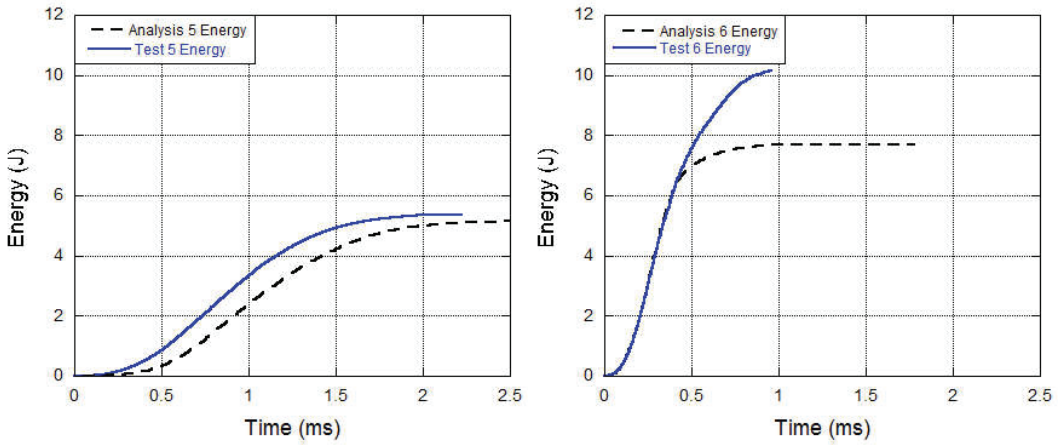

Figure 4.7. Experimental and numerical energy history comparison of Test 5 and 6

4.4 Investigation of Specimen Crack Profiles and Strain Rate Variations

Final state of damage on the prismatic specimen for both front and rear faces of Test 1 is compared with LS-DYNA estimation, and illustrated in Figure 4.8 and Figure 4.9, respectively. Front face stands for the impact surface while rear face is the surface facing the specimen holder for the following discussions. Though no macroscopic damage was observed on the front and rear faces of experimental specimen, FE model predicted specimen to be divided into four main symmetrical pieces. Additionally, on the front face of specimen LS-DYNA predicted a local scabbing damage, which surrounds crushed concrete located at impact zone (Figure 4.8 (b)). High speed camera record of the specimen is also presented in Figure 4.10 to observe the crack initiation and development. No cracks were observed at the side surface facing the camera.

Final state of damage on the prismatic specimen for both front and rear faces of Test 2 is compared with LS-DYNA estimation, and illustrated in Figure 4.11 and Figure 4.12, respectively. Increasing the impact speed three times resulted in specimen damage with three-part structure, and also material crushing at the impact zone with pulverization (Figure 4.11 (a)). Similar observations could be made for LS-DYNA prediction both for the existence of material crushing at the impact zone and having a four-part structure (Figure 4.11 (b)). High speed camera record of the specimen throughout the test is presented in Figure 4.13. Unlike the previous specimen, a crack is observed at 0.5 milliseconds on the side surface of the specimen, which corresponds to

the time of peak force obtained from the striker tip. Width of this crack has increased by time.

Changing the boundary condition to a hole at the bottom surface with 60 mm diameter caused damage profile of the specimen shift into a five-part structure in Test 3 (Figure 4.14 (a)). However, LS-DYNA predicted a damage profile with four-part structure including a truncated circular crack which was locally formed at the impact zone of front face (Figure 4.14 (b)). On the other hand, as it can be seen from Figure 4.15 (b), truncated circular crack on the rear face of specimen was observed more severely than that of front face which is eventually proportional to the diameter of boundary condition. High speed camera record of the specimen throughout the test is presented in Figure 4.16. From the figure, permanent deformation on the specimen became clearly visible as tension crack on the side surface at 1.5 milliseconds, which exceeds time interval of peak load 0.5 ms.

Increasing the impact speed by three times in Test 4 did not significantly affect the crack pattern except for presence of crushing and pulverization of the material on the front face and spalling of material on the rear face, as seen in Figure 4.17(a) and Figure 4.18 (a). On the other hand, aside from four-part symmetric structure of damage, for the first time radial cracks were observed in LS-DYNA damage predictions that are occurring both on the front and rear faces, as seen in Figure 4.17(b) and Figure 4.18 (b). High speed camera record of the specimen throughout the test is also presented in Figure 4.19 to observe the crack initiation and development. From the figure, tension crack becomes visible on the side surface of the specimen at 0.3 milliseconds. This is also the time when the force obtained from the striker tip is the highest. Afterwards, damage rapidly propagates with the advance of time from 0.3 milliseconds to 0.9 milliseconds.

For Tests 5 and 6, boundary condition was changed to a hole at the bottom surface with 100 mm diameter. Although in front and rear damage states of the specimen a four-part structure was observed in test, LS-DYNA predicted a symmetrical form (Figure 4.20 and Figure 4.21). High speed camera record of the specimen throughout the test is also presented in Figure 4.22 to observe the crack initiation and development. From the figure, the first hairline thick tension crack on the side face is observed around 0.8 milliseconds. This is also the time when the force obtained from

the striker tip is the highest. The crack is observed to be more pronounced at the end of the test.

Increasing the speed by three times resulted in multiple pieces of cracks on the front and rear face of specimen after Test 6. Additionally, a circular damage was also observed at the central part of specimen in proportion to the hole diameter of support condition (Figure 4.23-a and Figure 4.24-a). On the other hand, LS-DYNA predicted a damage profile mainly divided into four symmetric sections with partially radial cracks in both of the faces. Similar to the damage observed from the test, a circular crack was detected (Figure 4.23-b and Figure 4.24-b). High speed camera record of the specimen throughout the test is presented in Figure 4.25. From the figure, the first hairline thick crack formation is observed on the side face at around 0.3 milliseconds which slightly exceeds the time interval of force obtained from the striker tip is the highest. The crack width and depth has increased noticeably at the end of the test.

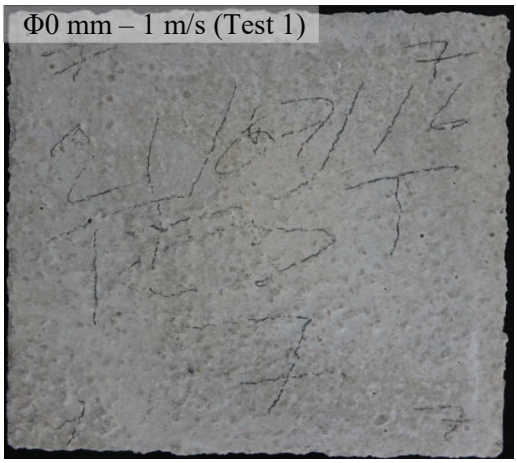

(a) Experimental

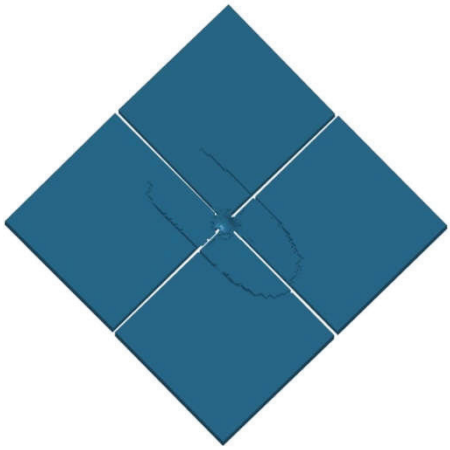

(b) Numerical model

Figure 4.8. Test 1 final damage state on front (impact) face of specimen

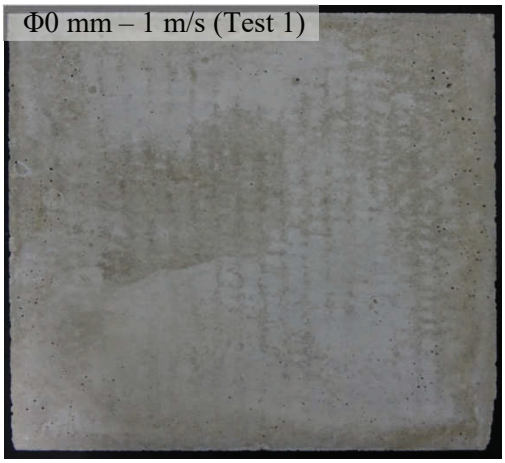

(a) Experimental

(b) Numerical model

Figure 4.9. Test 1 final damage state on rear face of specimen

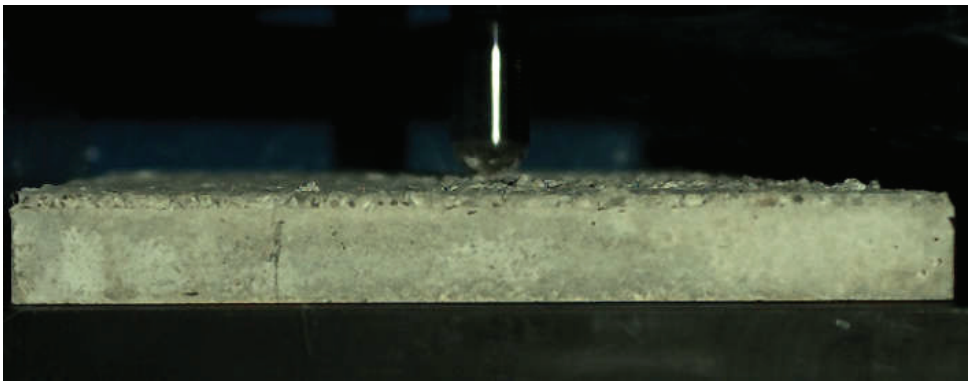

0 ms

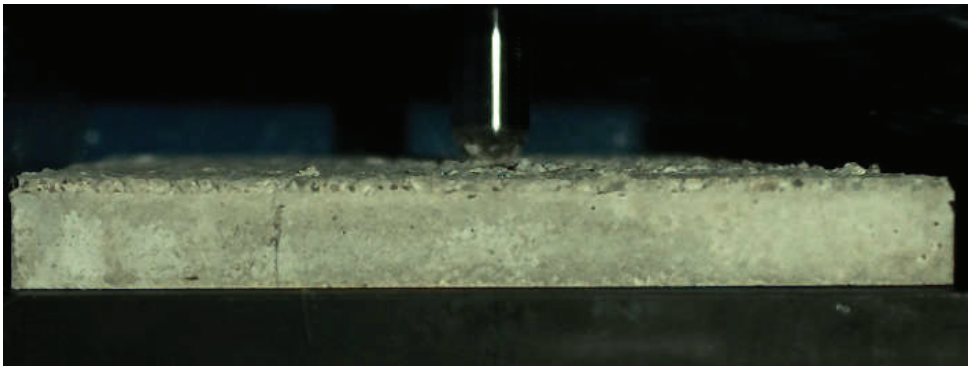

1 ms

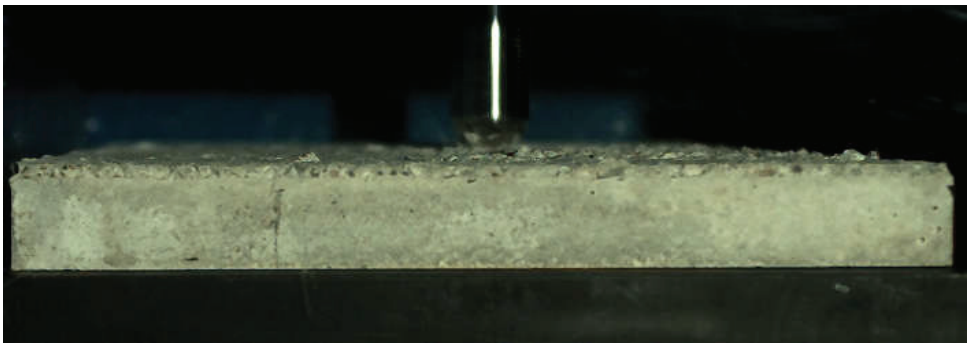

2 ms

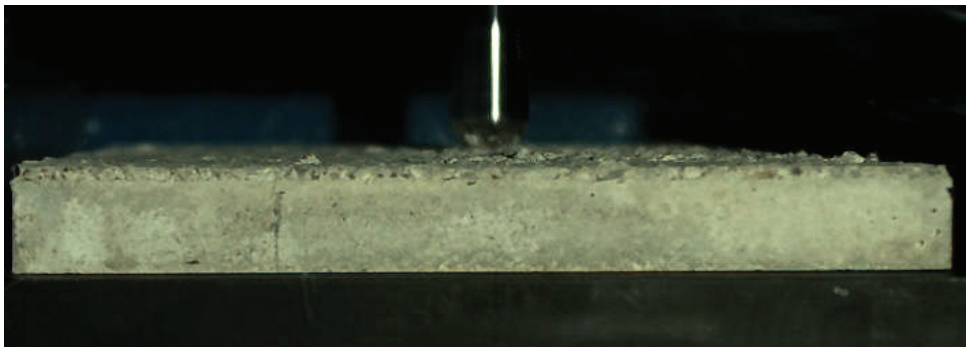

3 ms

Figure 4.10. Damage history of drop tower Test 1 (10000 fps)

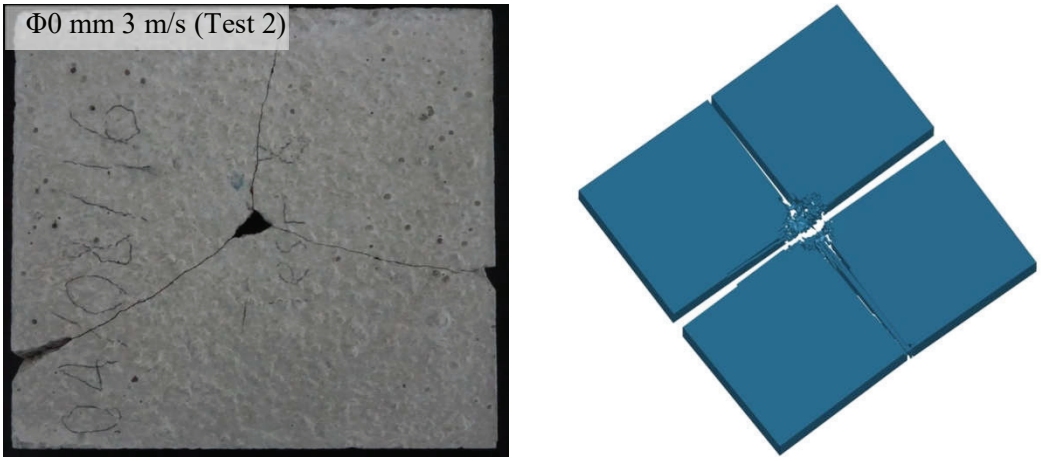

(a) Experimental (b) Numerical model

Figure 4.11. Test 2 final damage state on front (impact) face of specimen

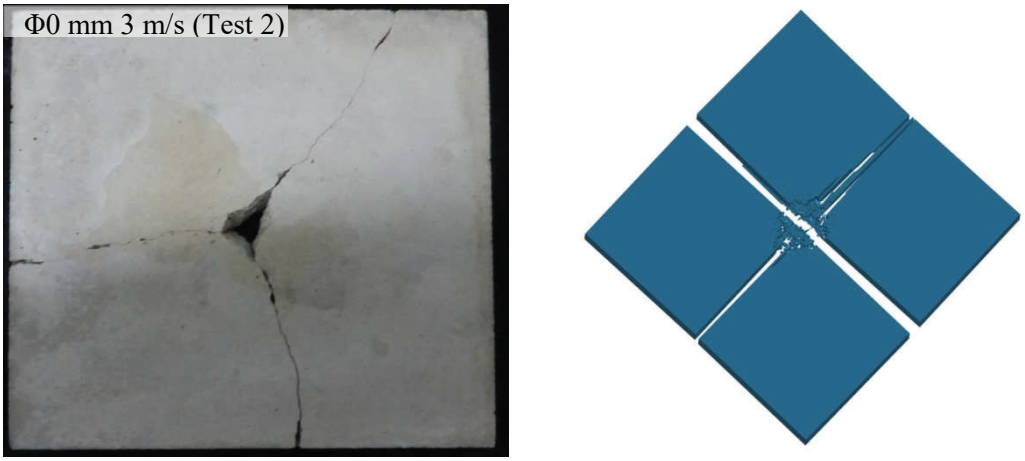

(a) Experimental (b) Numerical model

Figure 4.12. Test 2 final damage state on rear face of specimen

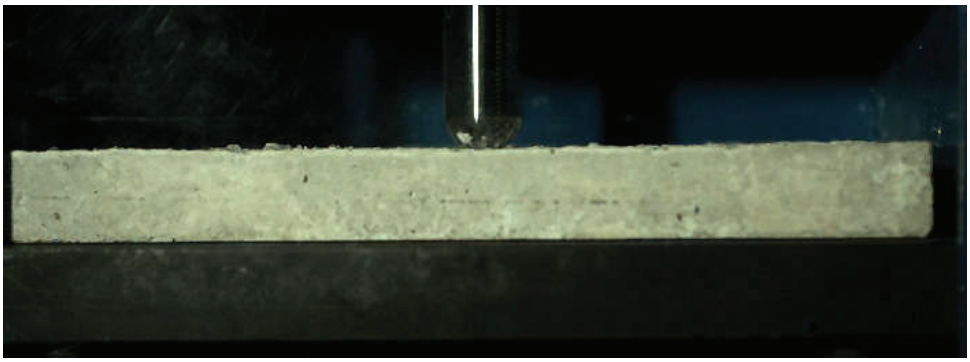

0 ms

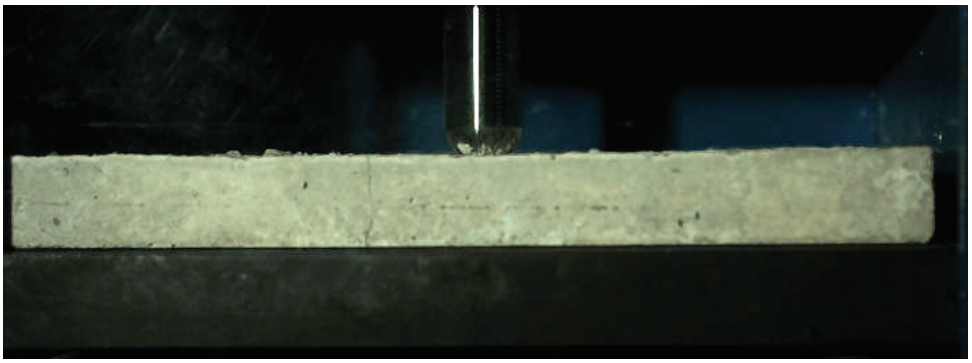

0.5 ms

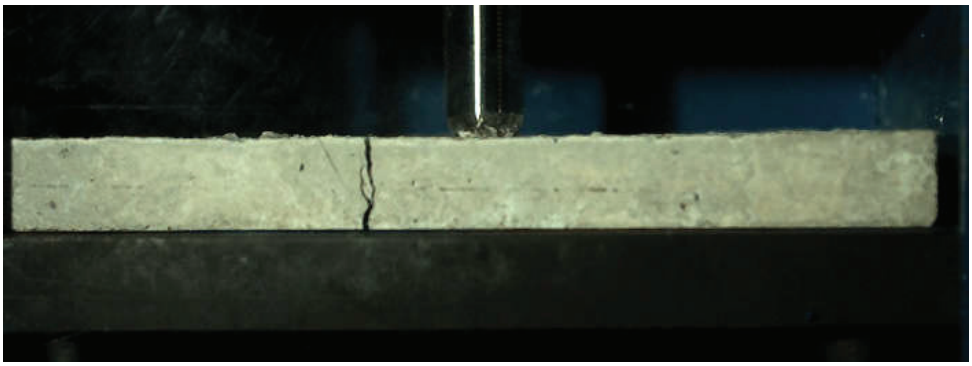

1 ms

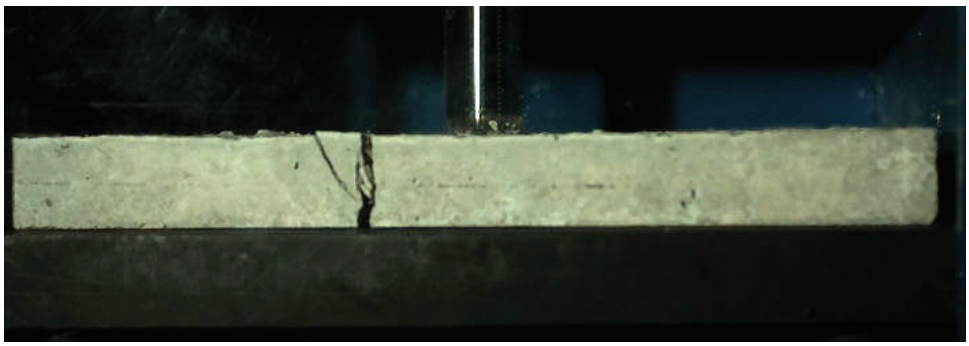

1.5 ms

Figure 4.13. Damage history of drop tower Test 2 (10000 fps)

(a) Experimental (b) Numerical model

Figure 4.14. Test 3 final damage state on front face of specimen

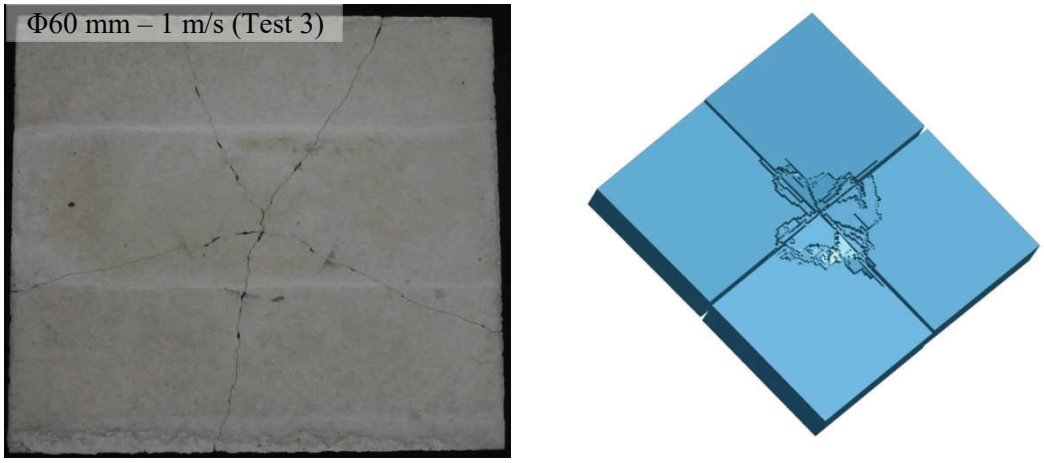

(a) Experimental (b) Numerical model

Figure 4.15. Test 3 final damage state on rear face of specimen

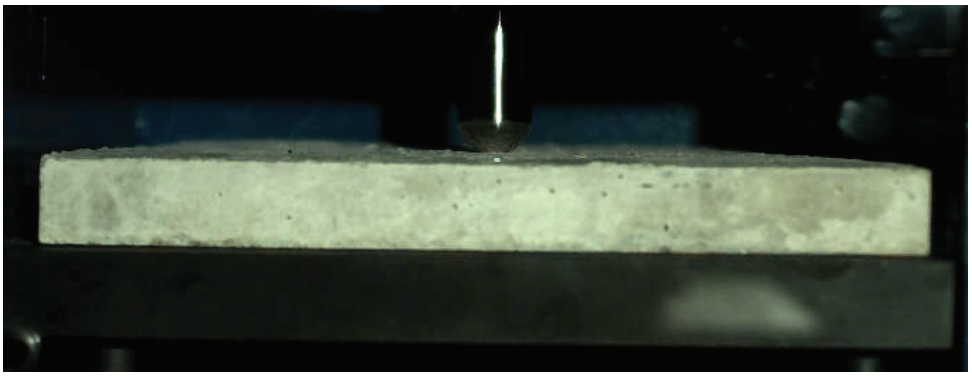

0 ms

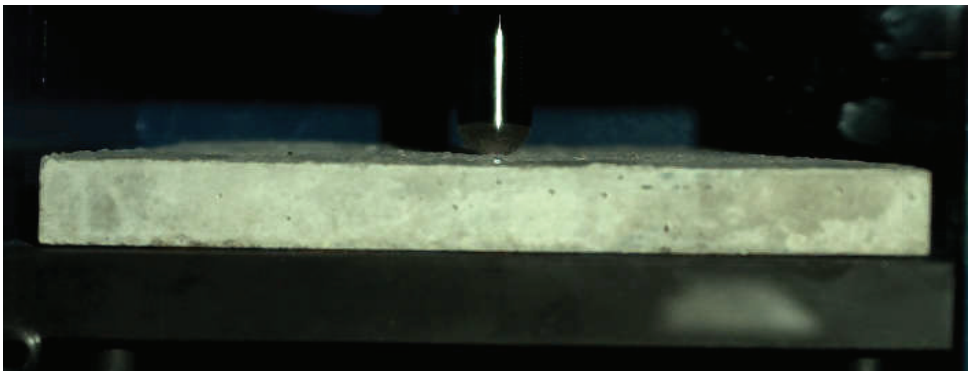

0.5 ms

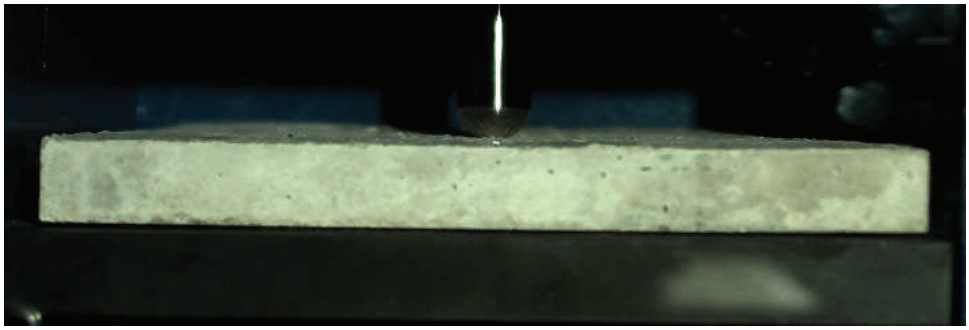

1 ms

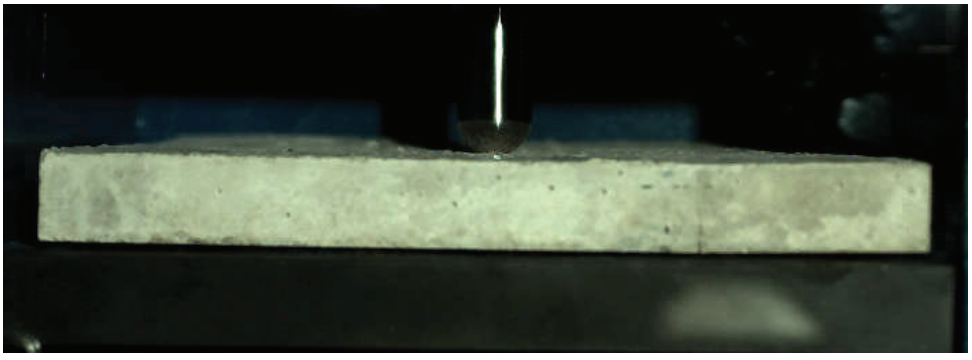

1.5 ms

Figure 4.16. Damage history of drop tower Test 3 (10000 fps)

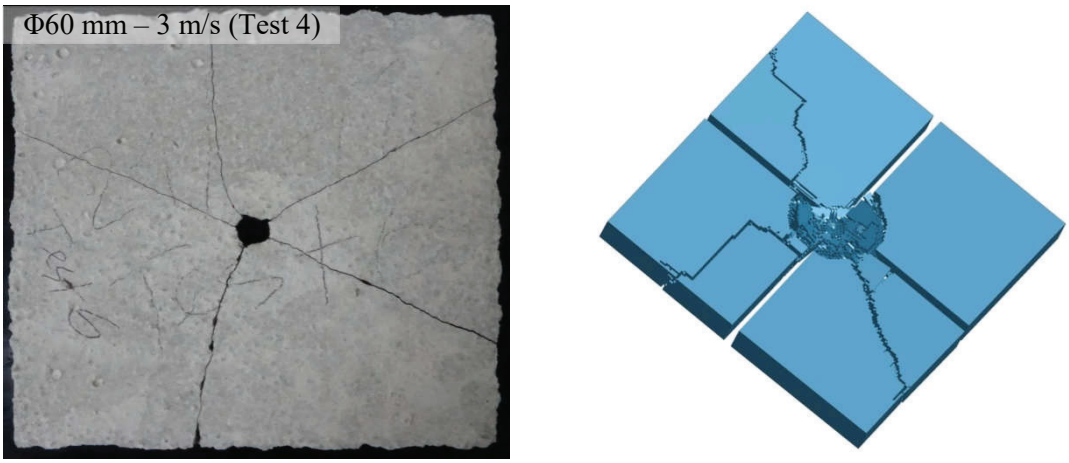

(a) Experimental (b) Numerical model

Figure 4.17 Test 4 final damage state on front face of specimen

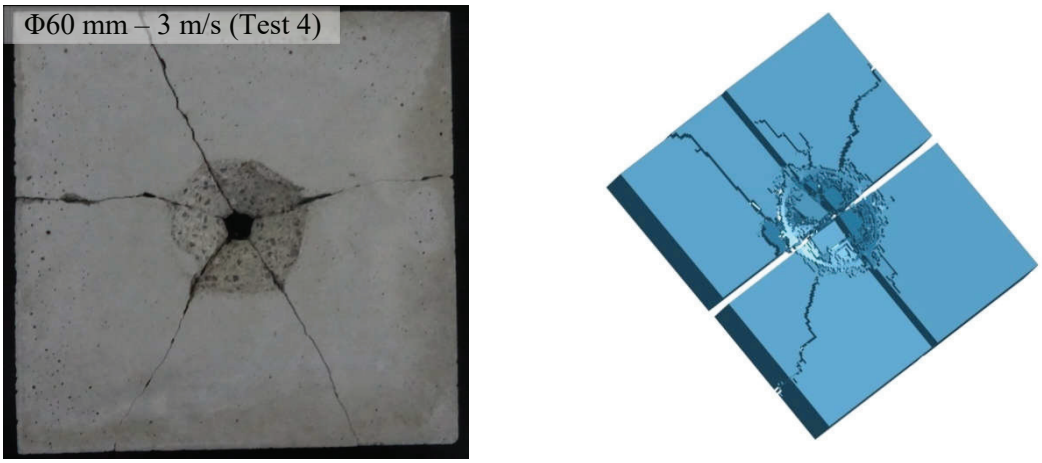

(a) Experimental (b) Numerical model

Figure 4.18. Test 4 final damage state on rear face of specimen

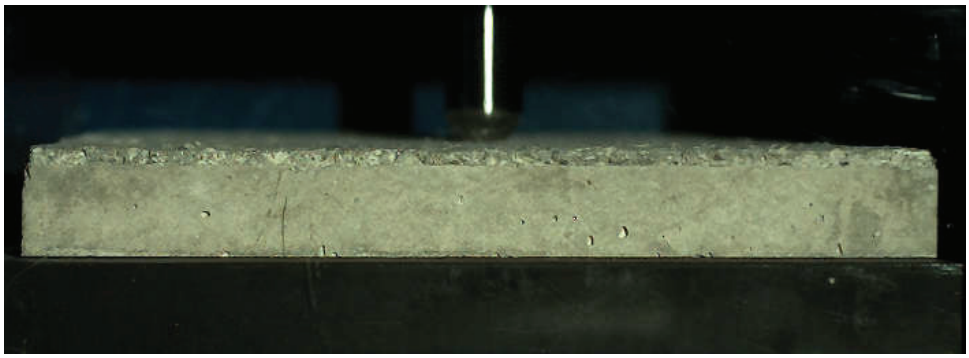

0 ms

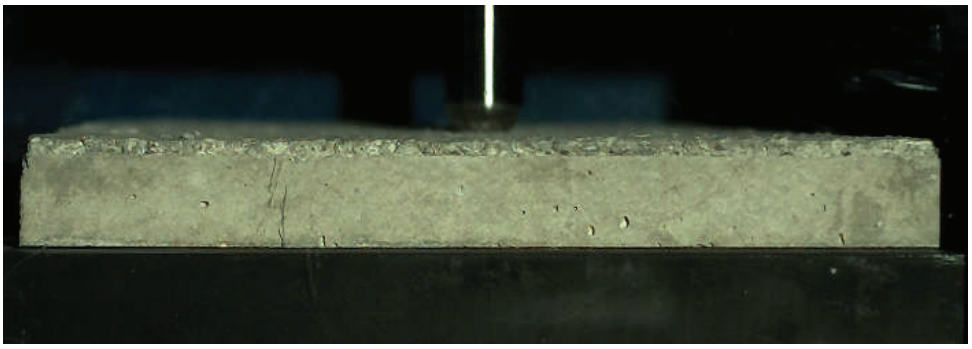

0.3 ms

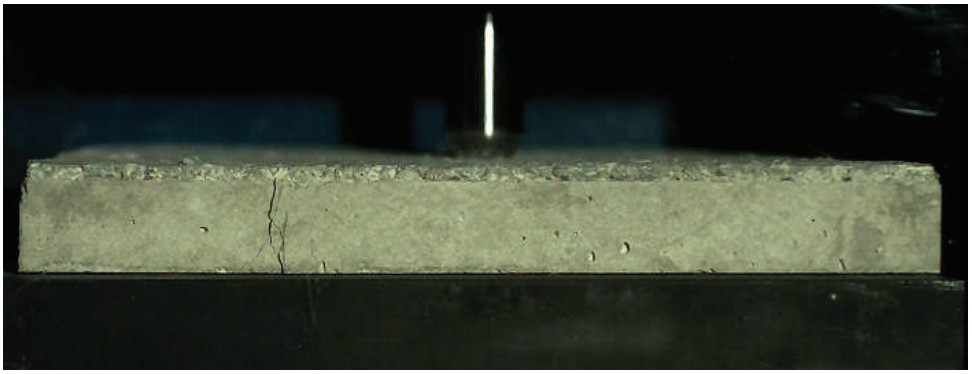

0.6 ms

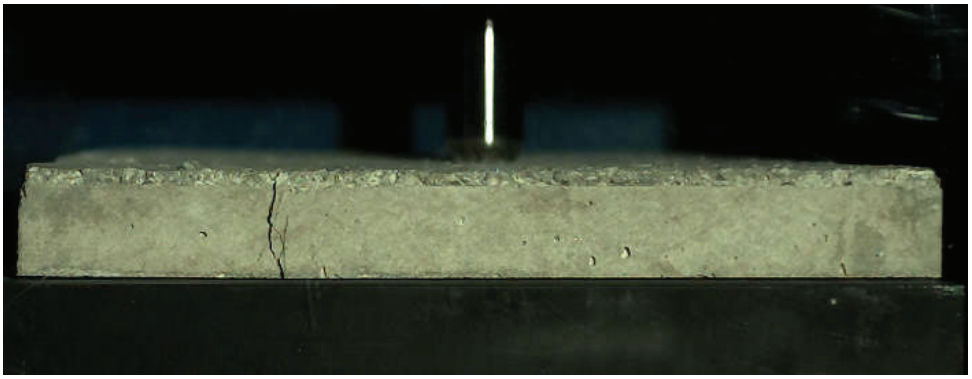

0.9 ms

Figure 4.19. Damage history of drop tower Test 4 (10000 fps)

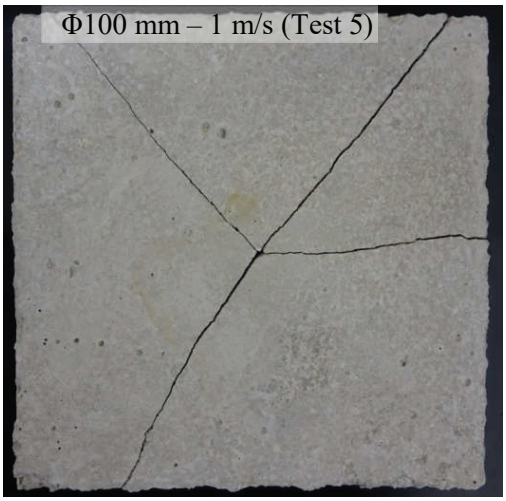

(a) Experimental

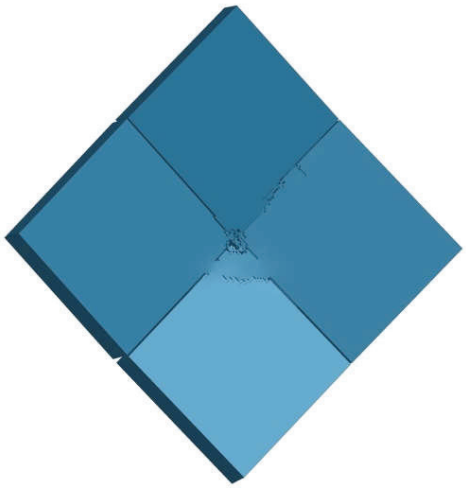

(b) Numerical model

Figure 4.20. Test 5 final damage state on front face of specimen

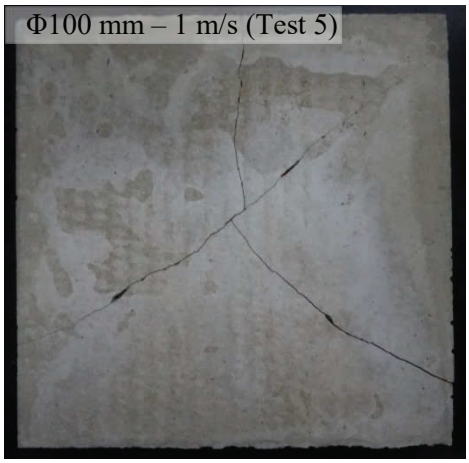

(a) Experimental

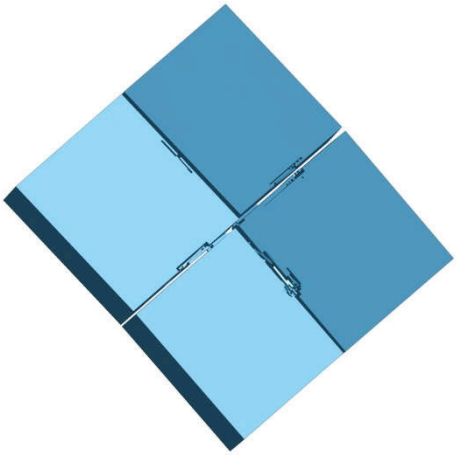

(b) Numerical model

Figure 4.21. Test 5 final damage state on rear face of specimen

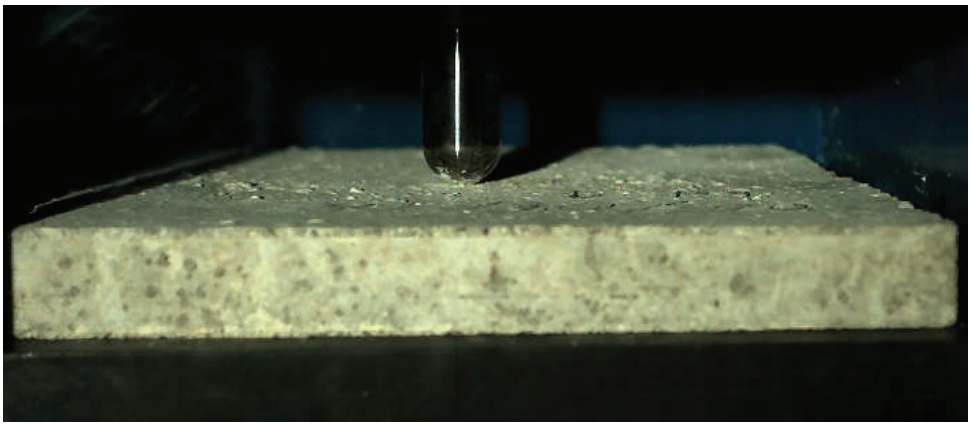

0 ms

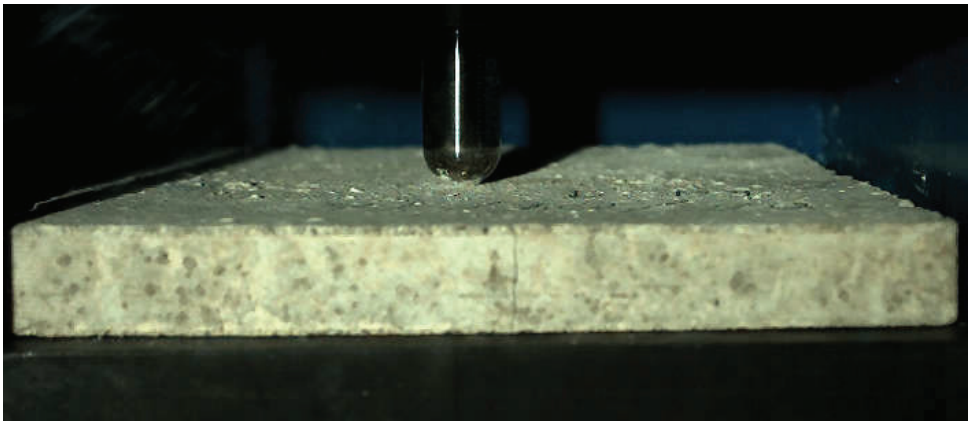

0.8 ms

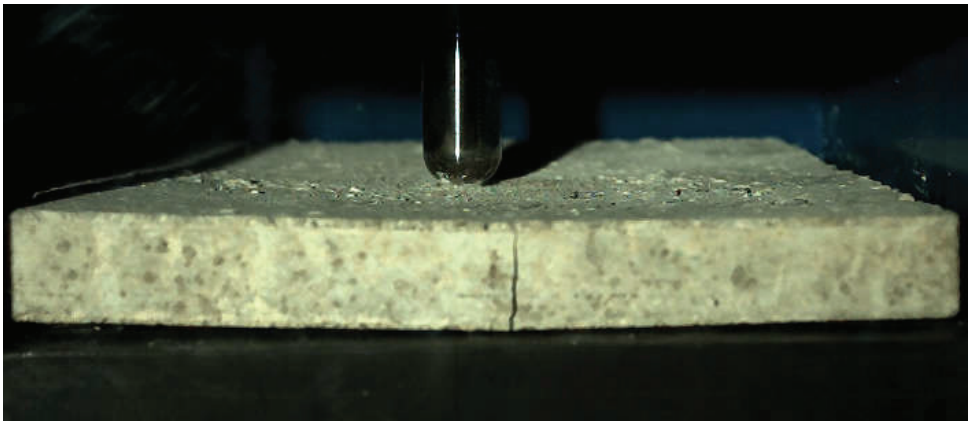

2.5 ms

Figure 4.22. Damage history of drop tower Test 5 (10000 fps)

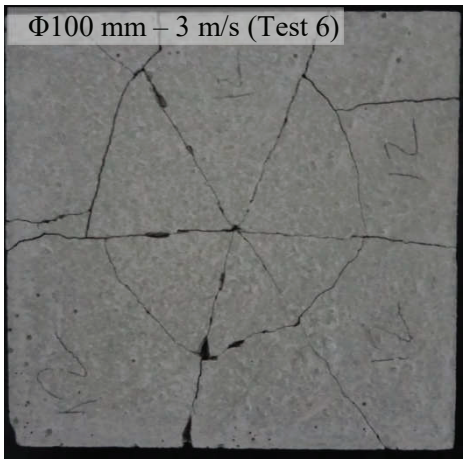

(a) Experimental

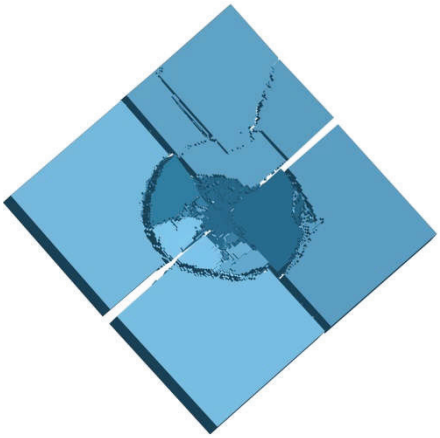

(b) Numerical model

Figure 4.23. Test 6 final damage state on front face of specimen

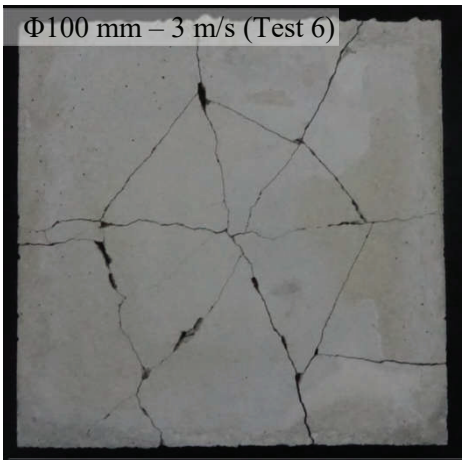

(a) Experimental

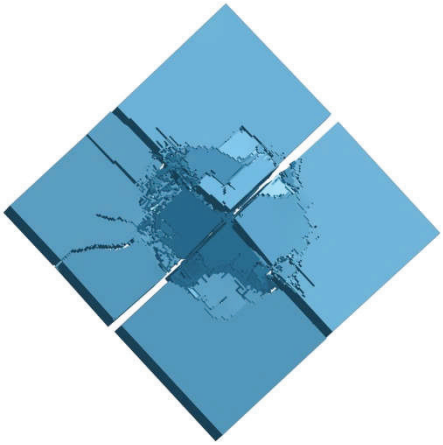

(b) Numerical model

Figure 4.24. Test 6 final damage state on rear face of specimen

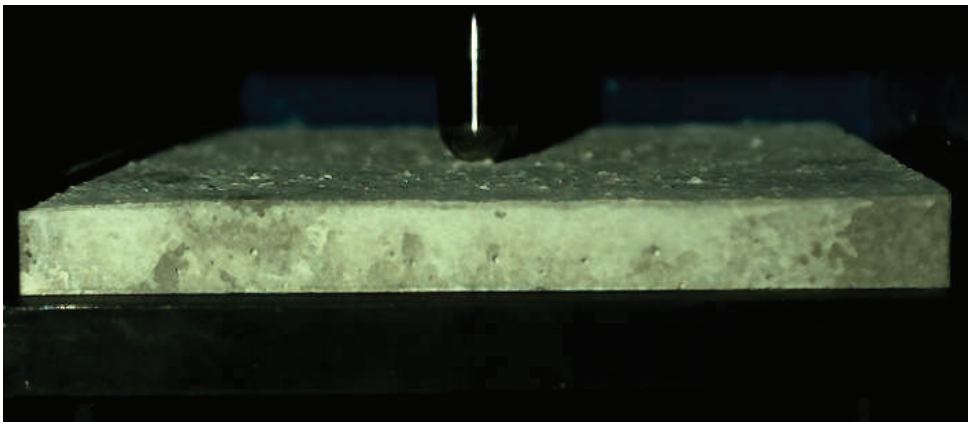

0 ms

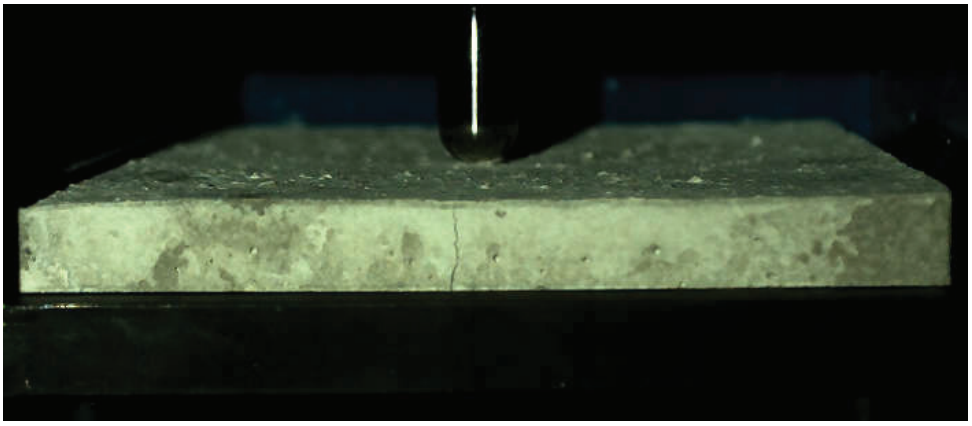

0.3 ms

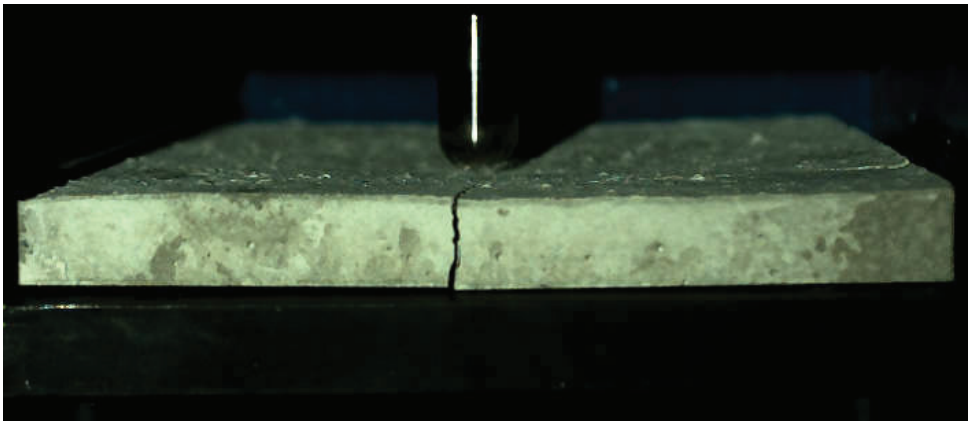

1 ms

Figure 4.25. Damage history of drop tower Test 6 (10000 fps)

Strain rate of the specimens were also investigated. For this purpose, strain rate of first and third principle strain were selected on the solid elements which enables to observe the maximum tensile and compression strains induced by the loading condition. Selection of representative solid elements were made sufficiently close to the impact

zone on the front face of specimen considering the damage occurring at the impact zone and thus to prevent misleading evaluation of strain rate. Figure 4.26 and 27 (a) present the strain rate history of selected element for Test 1 and 2 both without hole at the specimen holder and all the presented figures below has a time unit of microsecond. In Test 1 maximum strain rates from first and third principle strain were detected at the moment of peak force, and were reached (2.2 and 2.1 ms) as 686 and 454 1/s. However, in Test 2 highest strain rates of first and third principle strains were determined 0.4 and 1.9 ms after the peak force reached as 147 and 3880 1/s. Figure 4.26 (b and c) and Figure 4.27 (b and c) present strain rate variation on the front face of specimen for the first and third principle strains of Test 1 and Test 2, respectively.

Strain rate history of Test 3 and 4, both having 60 mm hole at the specimen holder, are presented in Figure 4.28 and 29 (a). In Test 3 the maximum strain rates of first and third principle strain were determined 1 ms later than the peak force reached and found out to be 740 and 718 1/s, respectively. In Test 4 it is determined 0.3 ms later than the peak force reached and detected to be 830 and 1030 1/s, respectively. Figure 4.28 and 29 (b and c) present strain rate variation over the specimen on front face of Test 3 and 4. From the figures it can be seen that the maximum strain rates for both of the tests were specifically detected to be in the central region of circular crack.

Strain rate histories of Test 5 and 6 are presented in Figure 4.30 and 31 (a). In Test 5 the maximum strain rates of first and third principle strain were determined at 1.8 ms as 133 and 124 1/s respectively. In Test 6 strain rates were obtained before the moment of peak force reached during the test. Highest values were found at 590 and 340 1/s for the strain rates of first and third principle strain. Figure 4.30 and 31 (b and c) present strain rate variation over the specimen on the front face. The impact region had the highest strain rate.

Generally, strain rates in overall except the damaged regions are lower than that of SHPB tests. Using HJC material model with the detected parameters for the numerical analyses of drop tower tests resulted in good agreement with specifically increase trend of forces and crack profile. Additionally, maximum 10% strength difference was observed between the drop tower numerical analyses and tests.

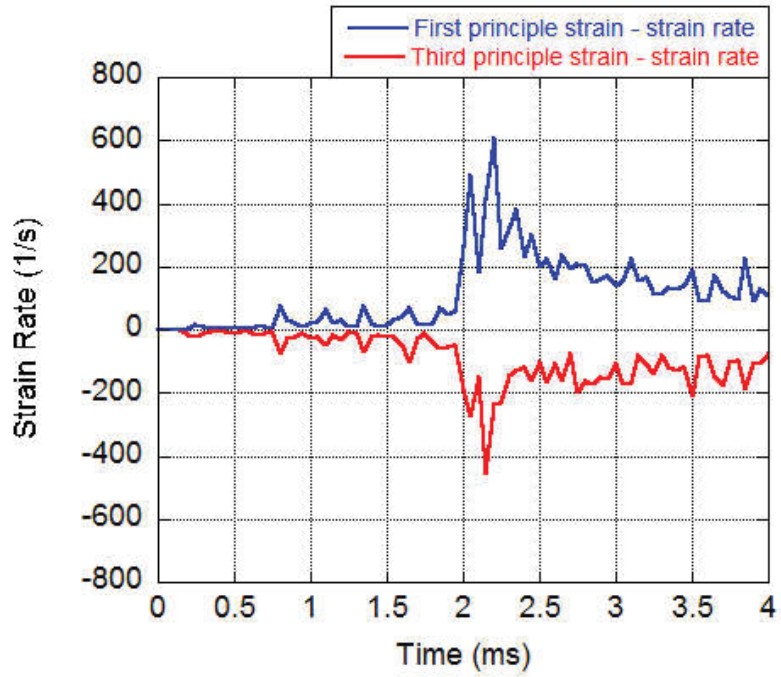

(a) Strain rate history

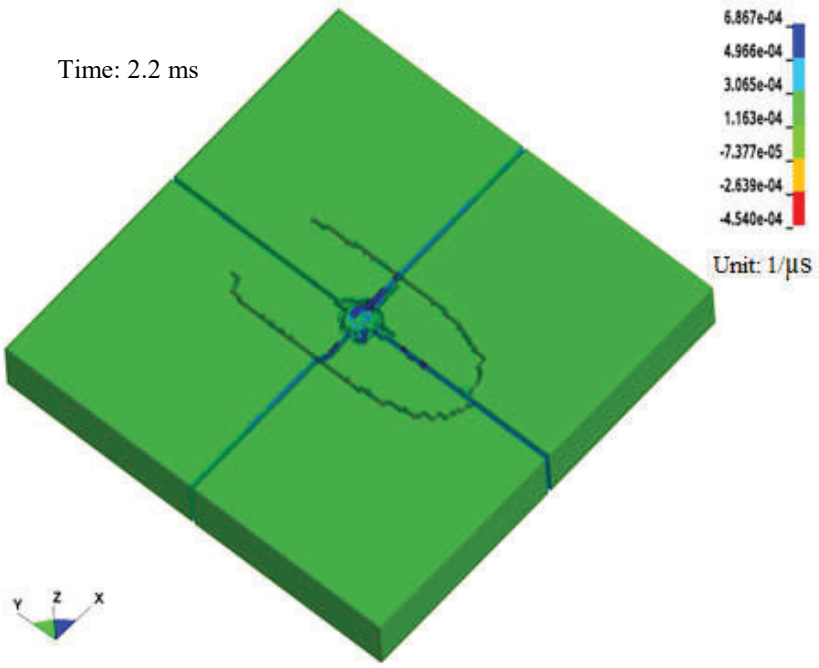

(b) Strain rate variation of first principle strain

Figure 4.26. Strain rate investigation of Test 1

(cont. on next page)

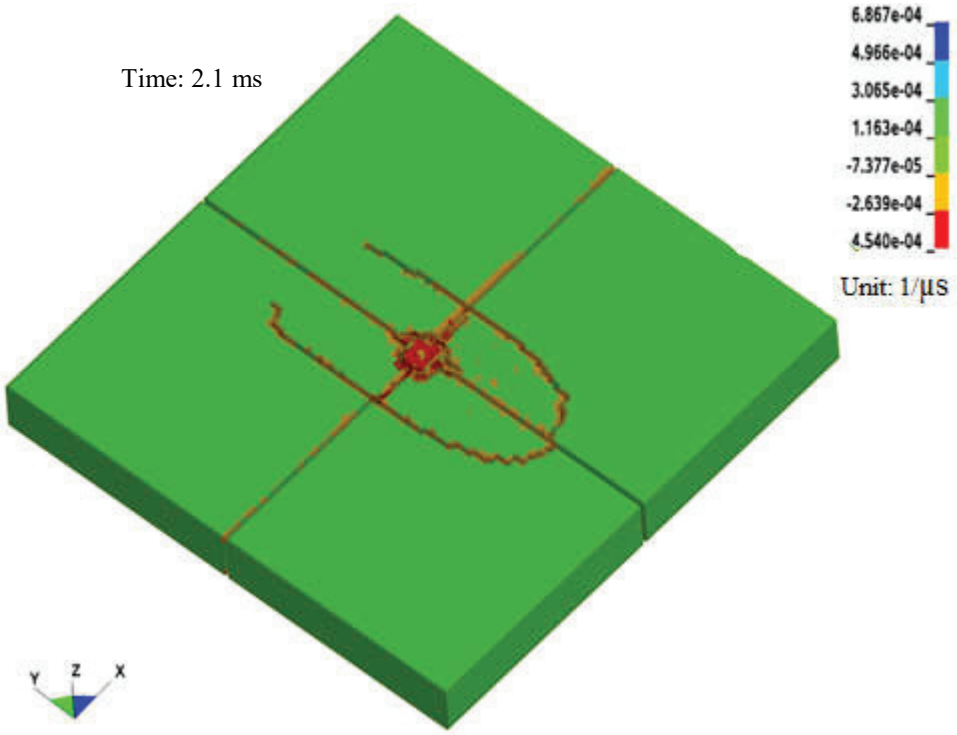

(c) Strain rate variation of third principle strain

Figure 4.26. (cont.)

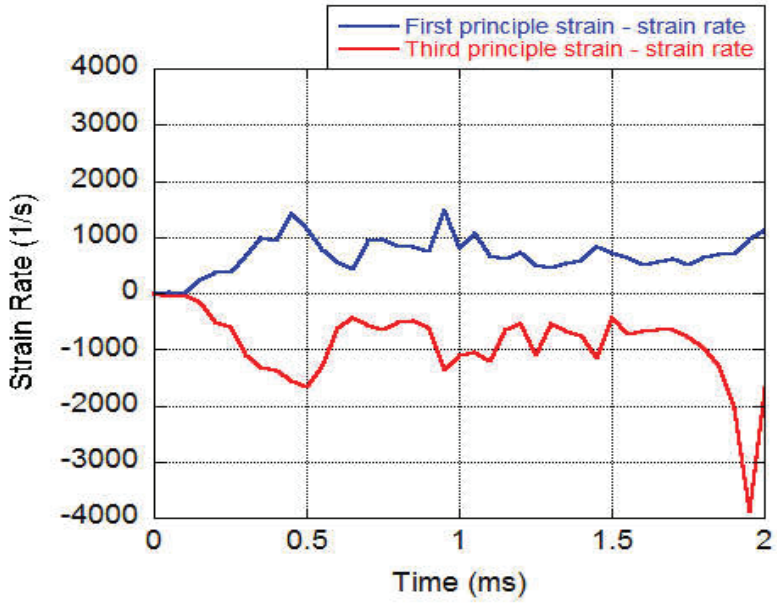

(a) Strain rate history

Figure 4.27. Strain rate investigation of Test 2

(cont. on next page)

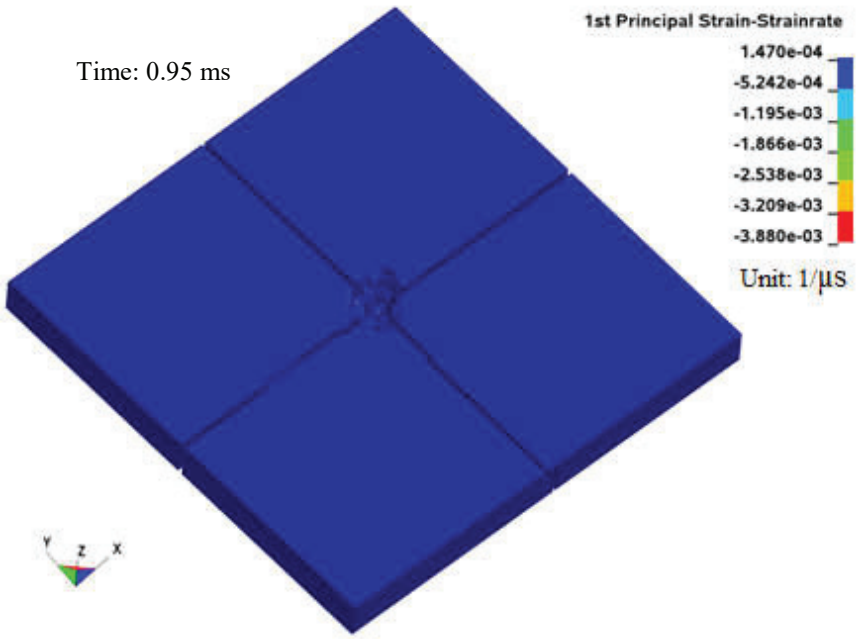

(b) Strain rate variation of first principle strain

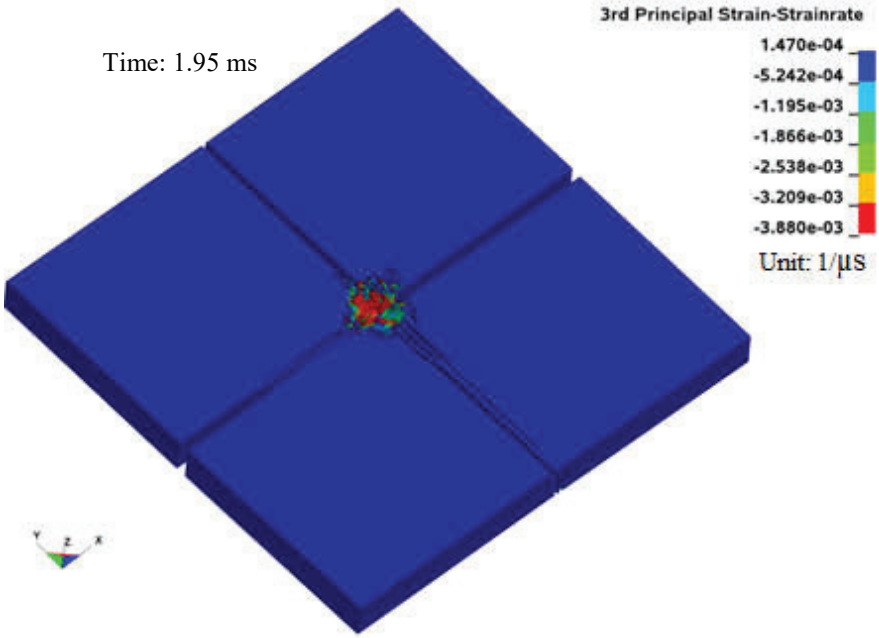

(c) Strain rate variation of third principle strain

Figure 4.27. (cont.)

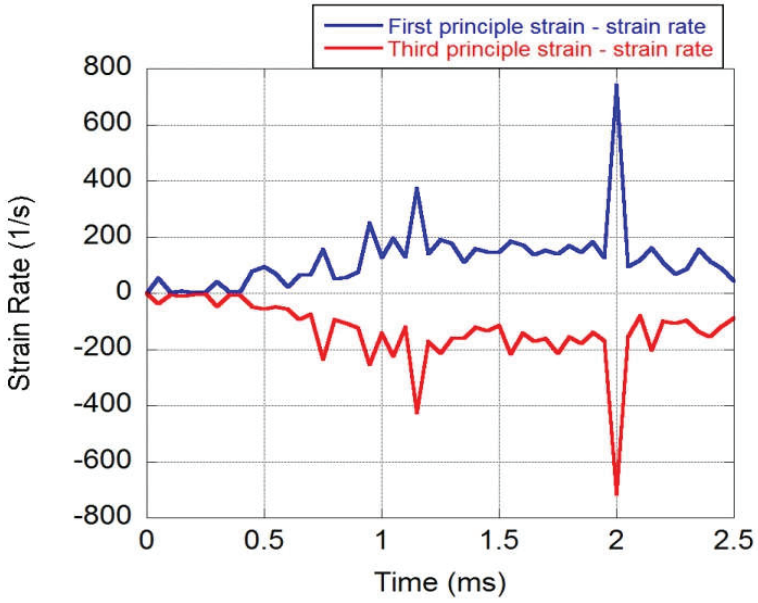

(a) Strain rate history

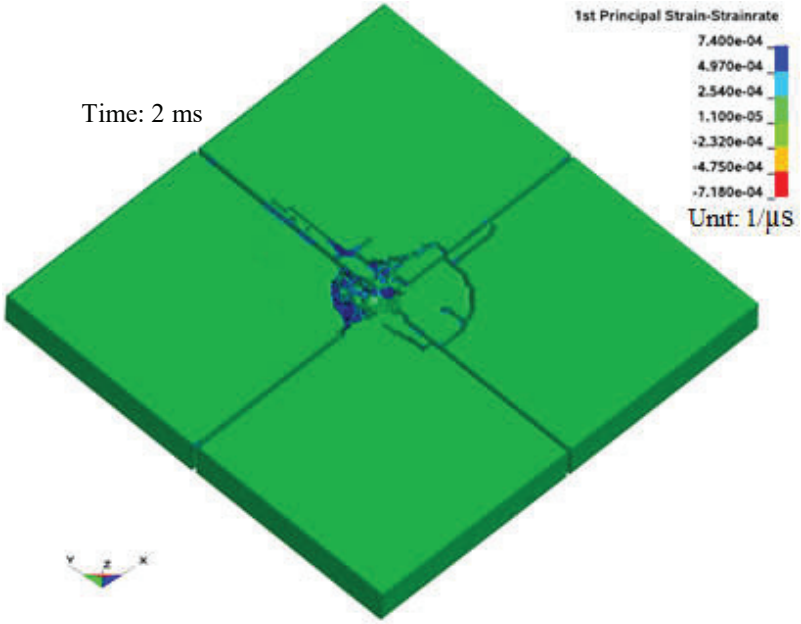

(b) Strain rate variation of first principle strain

Figure 4.28. Strain rate investigation of Test 3

(cont. on next page)

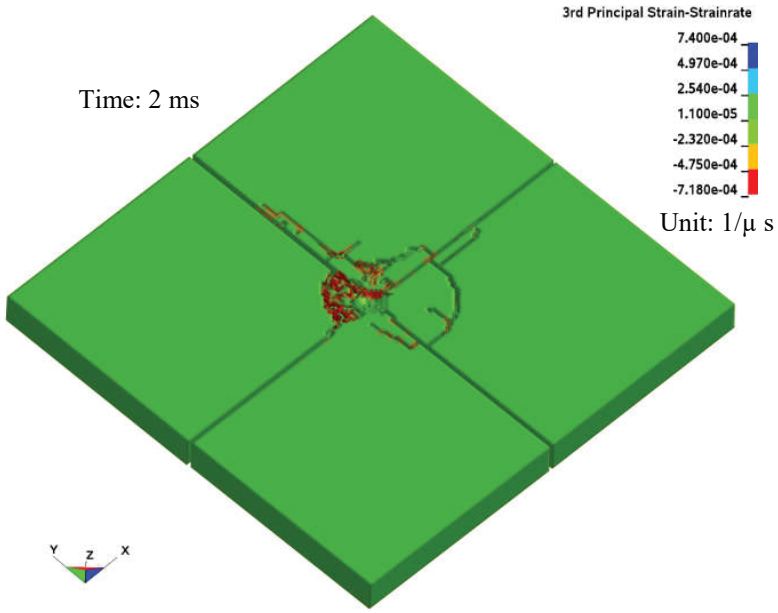

(c) Strain rate variation of third principle strain

Figure 4.28. (cont.)

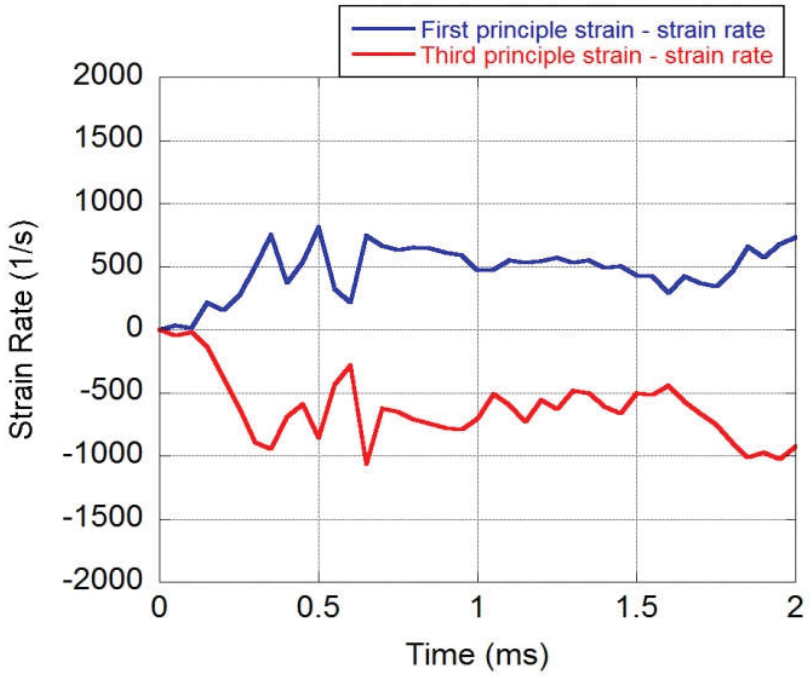

(a) Strain rate history

Figure 4.29. Strain rate investigation of Test 4

(cont. on next page)

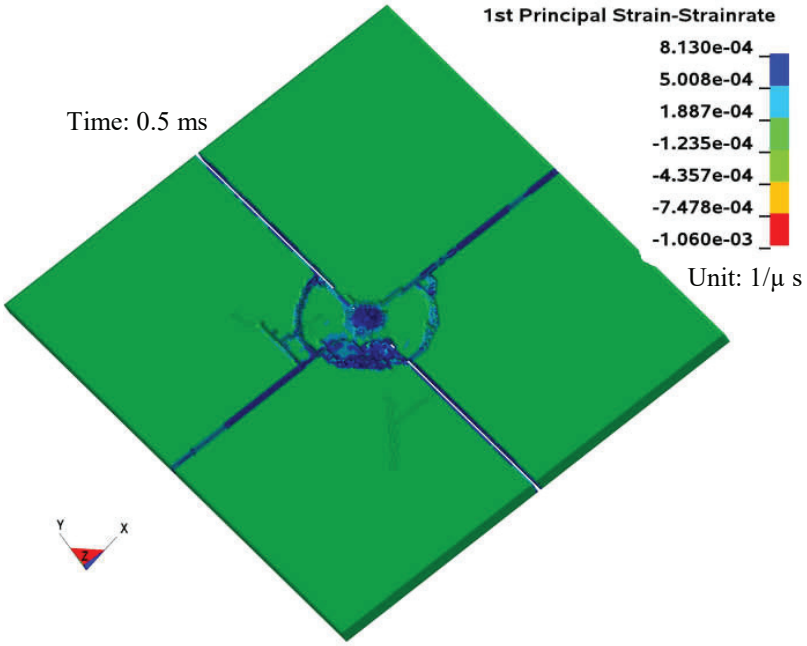

(b) Strain rate variation of first principle strain

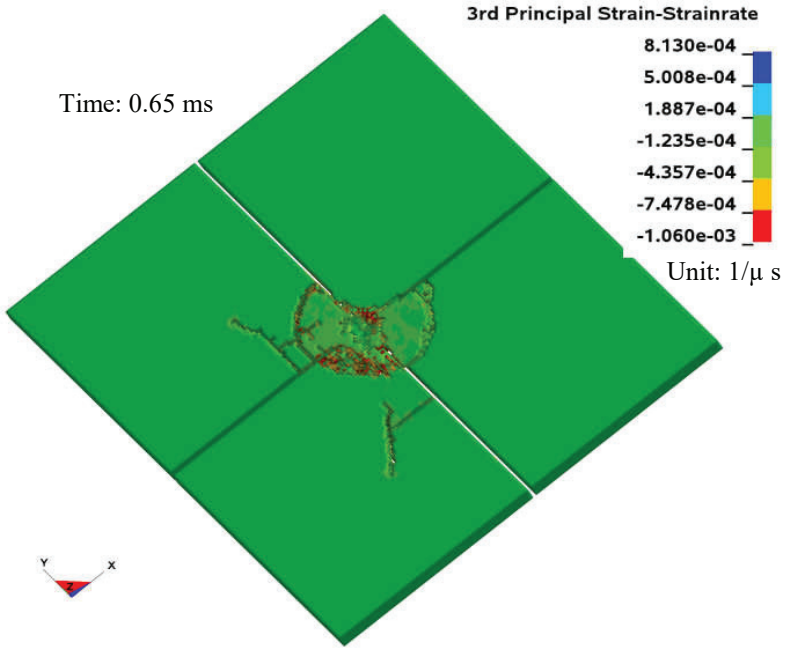

(c) Strain rate variation of third principle strain

Figure 4.29. (cont.)

(cont. on next page)

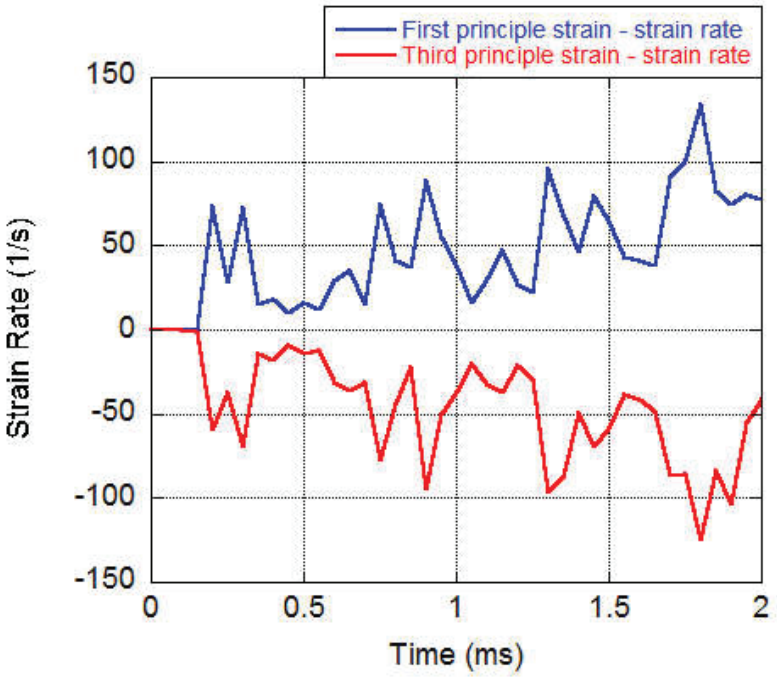

(a) Strain rate history

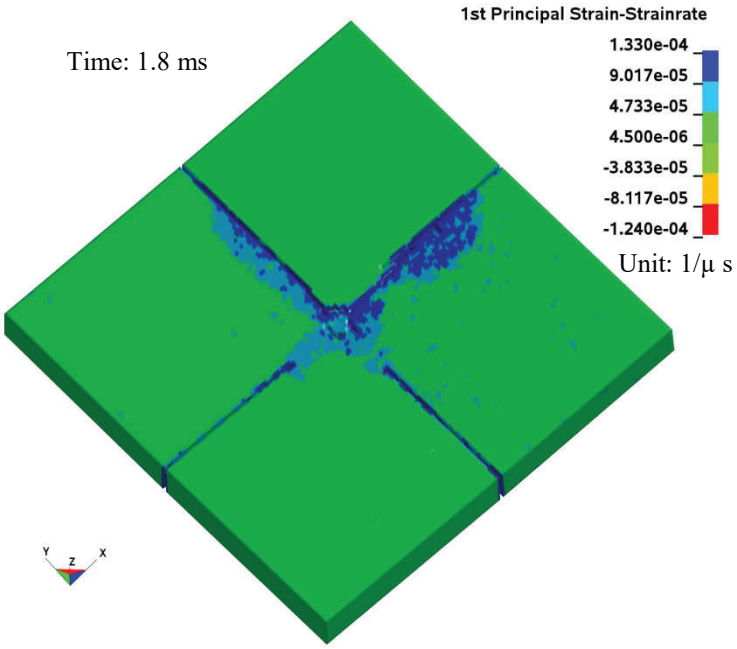

(b) Strain rate variation of first principle strain

Figure 4.30. Strain rate investigation of Test 5

(cont. on next page)

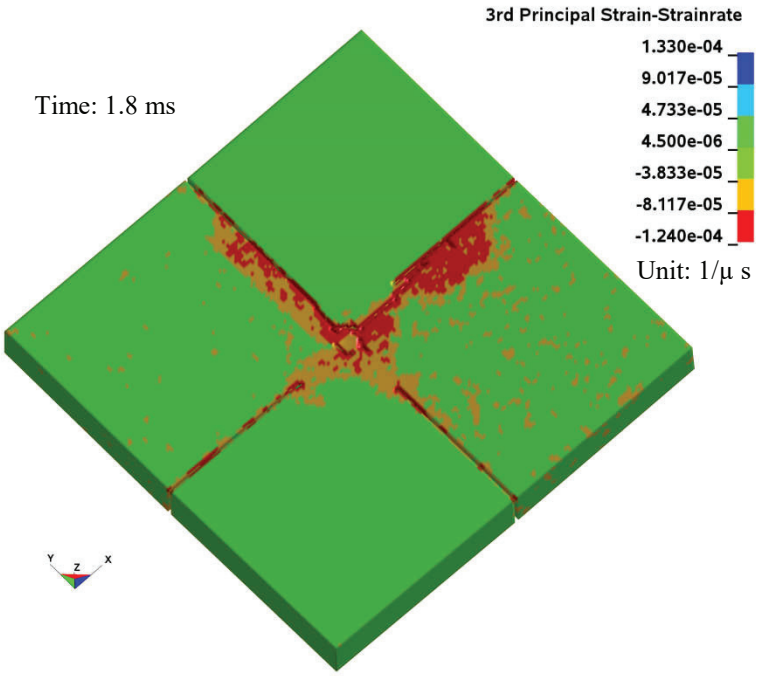

(c) Strain rate variation of third principle strain

Figure 4.30. (cont.)

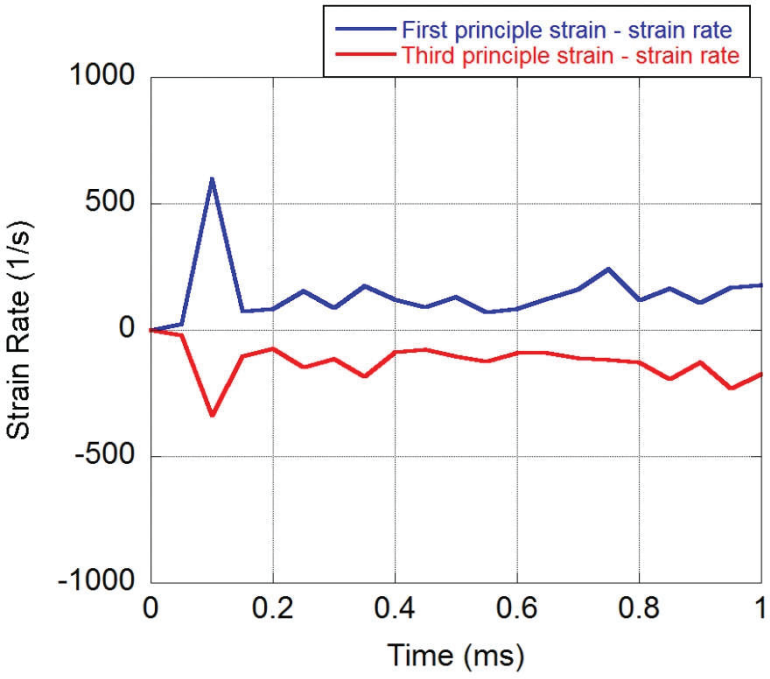

(a) Strain rate history

Figure 4.31. Strain rate investigation of Test 6

(cont. on next page)

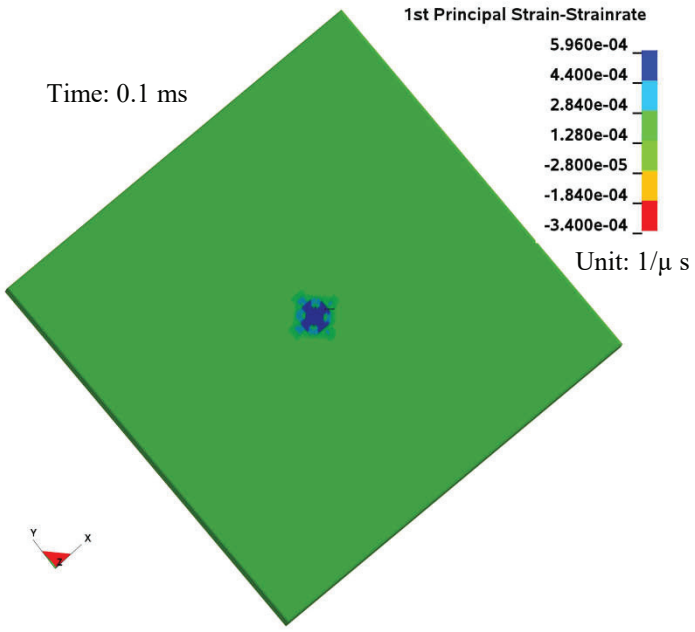

(b) Strain rate variation of first principle strain

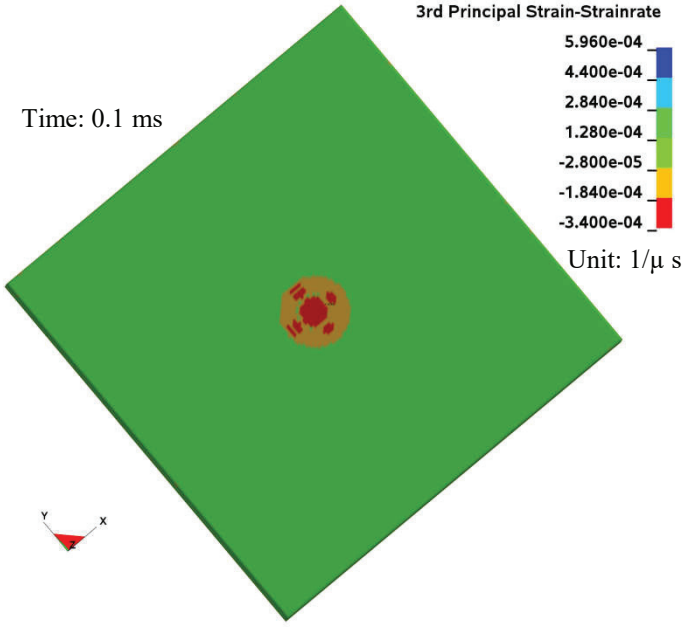

(c) Strain rate variation of third principle strain

Figure 4.31. (cont.)

CHAPTER 5

CONCLUSIONS

In the light of conducted experimental program and numerical analyses, the most important outcomes may be summarized as follows:

- Experimental studies carried out using Split Hopkinson Pressure Bar (SHPB) setup revealed that at strain rates even in the quasi-static regime ($3.55x10^{-5}$, $3.23x10^{-4}$, $2.97x10^{-3}$ 1/s) concrete shows a strain rate dependent behavior. Compressive strength slightly increased as strain rate was increased at lower strain rates, and almost doubled at high strain rate tests (240 1/s) compared to quasi-static loading rates.

- Holmquist-Johnson-Cook (HJC) model was found to be successful in finite element (FE) modeling of the high strain rate behavior of concrete. However, it was found that when determining the C parameter of HJC model that incorporate strain rate sensitive behavior of concrete into the model, considering high strain rate strength obtained from SHPB tests can be misleading. Confining stresses due to radial inertia develop in samples significantly contribute to the observed strength gain at such high strain rates, since concrete strength is highly dependent on hydrostatic stresses. Determining C parameter using these data points resulted in an overestimation in numerical analyses, since by this way strength gain due to radial inertia was counted twice. On the other hand, completely ignoring strain rate effects (C=0) yielded underestimated strength in numerical analyses, hinting an inherent strain rate dependent behavior of the material. At quasi-static strain rates, lateral confinement due to radial inertia is negligible but still a strength gain is observed with increasing strain rates. Determining C value according to this range yielded accurate predictions in numerical analysis. Therefore, as seen in this study, caution is required when concrete behavior is modeled under

high strain rates and strain dependent behavior is taken into account. Determining parameters using high strain rate tests by attributing entire strength gain on the strain rate dependent behavior can be misleading since only a small proportion of observed strength gain is solely due to strain rate dependent behavior.

- FE model of drop tower tests validated the HJC model used with determined model parameters. Force history comparisons between analyses and experimental results obtained under various boundary conditions and impact velocities have shown very good agreement with a maximum 10% peak strength difference. Crack profiles also showed a good agreement. Validating the model parameters under completely different test conditions increased the confidence on the previous conclusion.

Beyond drawn conclusions, this study also provided the literature with data obtained from a well-executed experimental program, which can be used for further studies. For example, there are various FE software and constitutive material models available to evaluate the impact and blast effects on concrete material. In addition to Johnson-Holmquist-Cook concrete model and nonlinear FE software LS-DYNA, further studies can be conducted using other constitutive models and FE software to investigate the observed behavior in more detail. .

REFERENCES

Malvern, L. E., et al. (1985). Dynamic Compressive Testing of Concrete. *Proceedings of Second Symposium on the Interaction of Non-Nuclear Munitions with Structures*. Panama City Beach, Florida

Ross, C. A., Thompson, P. Y., Tedesco, J. W. 1989. Split-Hopkinson Pressure-Bar Tests on Concrete and Mortar in Tension and Compression. *ACI Materials Journal*, 86, 475-781.

Bischoff, P. H. & Perry, S. H. 1991. Compressive Behavior of Concrete at High Strain Rates. *Materials and Structures*, 24, 425-450.

Tedesco, J. W. & Ross C. A. (1998). Strain-Rate-Dependent Constitutive Equations for Concrete. *Journal of Pressure Vessel Technology*, 120, 398-405.

Grote, D. L., Park, S. W. & Zhou, M. (2001). Dynamic Behavior of Concrete at High Strain Rates and Pressures: I. Experimental Characterization. *International Journal of Impact Engineering*, 25, 869-886.

Li, Q. M. & Meng, H. (2003). About the Dynamic Strength Enhancement of Concrete-like Materials in a Split Hopkinson Pressure Bar Test. *International Journal of Solids and Structures*, 40, 343-360

Drucker, D. C. & Prager, W. (1952). Soil Mechanics and Plastic Analysis of Limit Design. *Quart. Appl. Math*, 10, 157-165.

Hao, H. & Hao, Y. 2011. Numerical Evaluation of the Influence of Aggregates on Concrete Compressive Strength at High Strain Rate. *International Journal of Protective Structures*, 2, 177-206.

Hao, Y. et al. 2013. Influence of end Friction Confinement on Impact Tests of Concrete Material at High Strain Rate. *International Journal of Impact Engineering*, 60, 82-106.

Guo, Y. B. et al. 2017. Response of high-strength concrete to dynamic compressive loading. *Intl. Journal of Impact Engineering* 108, 114-135

FIB (International Federation for Structural Concrete). (2010). CEB-FIP Model Code 2010

Magnusson, J. et al. (2010). Air-Blast-Loaded, High-Strength Concrete Beams. Part II: Numerical Non-linear Analysis. *Magazine of Concrete Research*, 62, 235-242.

Riedel, W. et al. (1999). Penetration of Reinforced Concrete by BETA-B-500, Numerical Analysis Using a New Macroscopic Concrete Model for Hydrocodes. *Proceedings of the 9 th international Symposium Interaction of the Effects of Munitions with Structures*. Berlin, Germany.

Westerling, L. 2005. User Subroutines in Autodyn for Simulation of Reinforced Concrete (in Swedish with abstract in English). *Swedish Defence Research Agency.*Tumba, Sweden.

CEB (Comite Euro-International Du Beton). (1993). CEB-FIP Model Code 1990, Thomas Telford, London

Johnson, G. R., & Cook, W. H. (1983). A constitutive Model and Data for Metals Subjected to Large Strains , High Strain Rates and High Temperature. *Proceedings of the 7th International Symposium on Ballistics*. The Hague, Netherlands

Lin, X. et al. (2014). Modelling the Response of Reinforced Concrete Panels Under Blast Loading. *Materials and Design*, 56, 620-628.

Livermore Software Technology Corporation (LSTC). (2014). LS-DYNA Keyword User's Manual Volume II: Material Models.

Li, J. & Hao, H. (2014). Numerical Study of Concrete Spall Damage to Blast Loads. *International Journal of Impact Engineering*, 68, 41-55.

Jawed, I., Childs, G., Ritter, A., Winzer, S., Johnson, T., Barker, D. 1987. High-Strain Rate Behavior of Hydrated Cement Pastes. *Cement and Concrete Research*, 17, 433-440.

Gran, J. K., Florence, A. L., Colton, J. D. 1989. Dynamic Triaxial Tests of High-Strength Concrete. *ASCE Journal of Engineering Mechanics*, 115, 891-904.

Wang, S. et al. 2011. Effect of high strain rate loading on compressive behavior of fibre-reinforced high-strength concrete. *Magazine of concrete Research*, 63, 813-817.

Su, H. et al. 2014. Mechanical properties of ceramic fiber-reinforced concrete under quasi-static and dynamic compression. *Materials and Design*, 57, 426-434

Xiao, J. et al. 2015. Compressive behavior of recycled aggregate concrete under impact loading. 71, 46-55

Deng, Z. et al. 2016. Compressive behavior of the cellular concrete utilizing millimeter-size spherical saturated SAP under high strain-rate loading. *Construction and Building Materials,* 119, 96-106.

Holmquist, T. J., Johnson, G. R. & Cook, W. H. (1993). A Computational Constitutive Model for Concrete Subjected to Large Strains, High Strain Rates and High Pressures. *14th International Symposium on Ballistics*. Quebec City, Canada.

Erdoğan, T. Y. (2013). Beton. Ankara: ODTU Yayıncılık.

Chen, W.W. & Song, B. (2011). Split Hopkinson (Kolsky) Bar Design, Testing and Applications. New York: Springer Science & Business Media

Subhash, G. & Ravichandran, G. (2000). Split-Hopkinson Pressure Bar Testing of Ceramics. *ASM Handbook Mechanical Testing and Evaluation*, 8, 497-504.

Ehrgott, J. Q. (1989). Mechanical Property Test Results on a High Strength Concrete. Structures Laboratory, Waterways Experiment Station, Vicksburg, MS

Hanchak, S. J. et al. (1992). Perforation of Concrete Slabs with 48 MPa and 140 MPa unconfined compressive strengths. *International Journal of Impact Engineering*, 12, 1-7

Marsh, S. P. (1980). LASL Shock Hugoniot Data. *University of California Press*.

Ozbolt, J. & Sharma, A. (2012). Numerical Simulation of Dynamic Fracture of Concrete Through Uniaxial Tension and L-Specimen. *Engineering Fracture Mechanics*, 85, 88-102

LS-DYNA v971. Nonlinear Finite Element Software. Livermore Software Technology Corporation.

Vita

Mehmet Alper ÇANKAYA was born in İzmir/TURKEY in October 10, 1985. After graduation from Civil Engineering department of Suleyman Demirel University, he continued his M.Sc. and Ph.D. studies as research assistant in İzmir Institute of Technology.

Education:

- Ph.D. 2011, Civil Engineering, İzmir İnstitute of Technology
- M.Sc. 2008, Structural Mechanics (Civil Engineering), İzmir Institute of Technology
- B.Sc. 2004, Civil Engineering, Suleyman Demirel University.

Journal Papers:

- Basturk, S. B., Tanoglu, M., Cankaya, M. A., et al. (2016). Dynamic behavior predictions of fiber-metal laminate/aluminum foam sandwiches under various explosive weights. *Journal of Sandwich Structures & Materials*,18(3), 321-342.
- Donmez, C. and Cankaya, M. A., (2013). Effect of infill walls on the drift behavior of reinforced concrete frames subjected to lateral-load reversals. *Journal of Earthquake Engineering,* 17(5), 611-636.

Conference Papers:

- Cankaya, M. A. and Donmez, C. (2011, 11-14 Ekim). Tersinir Yükler Altında Dolgu Duvarların Betonarme Çerçevelerin Rijitlik, Dayanım, Ötelenme Profili ve Doğal Frekanslarına Etkisi. *1'inci Türkiye Deprem Mühendisliği ve Sismoloji Konferansı*, Ortadoğu Teknik Üniversitesi, Ankara, TÜRKİYE.
- Tasdemirci, A., Cankaya M. A., et al. (October 19-21, 2016). The effect of pulse shaping on the dynamic mechanical behavior of concrete. *22nd DYMAT Technical Meeting: Experimental Testing and Modeling of brittle materials at high strain rates*, Grenoble, FRANCE.